MAGNETIC ORDERING OF ERBIUM AND UNi_2Si_2 BY NEUTRON SCATTERING

BY

HONG LIN, M.S.

A Thesis

Submitted to the School of Graduate Studies

in Partial Fulfilment of the Requirements

for the Degree

Doctor of Philosophy

McMaster University

November, 1991

MAGNETIC ORDERING OF ERBIUM AND UNi_2Si_2 BY NEUTRON SCATTERING

DOCTOR OF PHILOSOPHY (1992) **McMASTER UNIVERSITY**

(Physics) Hamilton, Ontario

TITLE: Magnetic Ordering of Erbium and UNi_2Si_2 by Neutron Scattering

AUTHOR: Hong Lin, B.Sc. and M.Sc. (Beijing University)

SUPERVISOR: Professor M. F. Collins

NUMBER OF PAGES: xii, 119

ABSTRACT

The magnetic ordering has been studied in UNi_2Si_2 and erbium single crystals by elastic neutron scattering. Abundant results are given regarding the magnetic structure, magnetic phase transitions, and the effect of a magnetic field on these properties.

Three ordered phases are observed in UNi_2Si_2. They have been determined to be an incommensurate longitudinal spin density wave with a magnetic wave vector around $q=0.74c^*$ in the high temperature phase, a simple body-centred antiferromagnet in the intermediate temperature phase, and a square wave in the low temperature phase. This square wave can be viewed equivalently as a longitudinal spin density wave with $q=2/3c^*$ superimposed on a ferromagnetic component . Hysteresis and sample dependence are observed in the low-temperature phase transition. The two lower temperature phase transitions are both first order. The transition to paramagnetism is second order with a critical exponent $\beta=0.35\pm0.03$. When a magnetic field is applied along the c axis, the intermediate temperature phase is destabilised and disappears above a field of 3.5T. Although there is no new phase induced by the field, there exists a reentrant point where the three ordered phases

can coexist.

Erbium has three distinct ordered phases: the cone phase at low temperatures, the c-axis modulated (CAM) phase at higher temperatures, and the intermediate phase with moments modulated both along c and perpendicular to c. Within these phases the modulation of the moments may lock in to the lattice. The observed weak harmonics of the wave vector **q** in the basal plane for the cone phase and the $\mathbf{q}=1/4\mathbf{c}^*$ structure in the intermediate phase can be explained by a basal-plane spin slip model. The effect of magnetic field along the c axis on the magnetic structure is to stabilise the cone phase and to destabilise the intermediate phase. A new lock-in structure with $\mathbf{q}=1/4\mathbf{c}^*$ in the cone phase is induced by fields above 1.8T. The presence of the field also stabilises the lock-in structure with $\mathbf{q}=2/7\mathbf{c}^*$ in both the intermediate and the CAM phases.

ACKNOWLEDGEMENTS

The work described in this thesis has stretched out over almost four years, and quite a number of people have contributed at one time or another both at McMaster University and at the Chalk River Laboratories of AECL Research where the experiments were performed. I would like to thank them all for their help.

It gives me great pleasure to thank my thesis advisor, Professor M. F. Collins, for suggesting the subject and providing a most stimulating environment. His professional guidance and kindness are deeply appreciated. It is he who introduces me to a lot of knowledge of physics and to the mysteries of western culture, and helps me with English for this thesis.

Almost everyone associated with the Neutron and Solid State Branch at Chalk River has contributed in some form. Especially, I would like to mention Dr. W. J. L. Buyers for his interest in this work. I have benefited greatly from his profound knowledge of solid state physics in general and neutron scattering in particular. He introduced me to the experimental techniques with caring supervision and remarkable patience, and suggested me involving in many experiments . I

am also grateful for the hospitality he extended to me at his home.

I would also like to extend my warmest thanks to Drs. E. C. Svenson, C. P. Martel, Z. Tun, B. M. Powell, T. M. Holden, W. Wei, J. H. Root, S. M. Kim, and Ms. A. M. VanDine and N. Waddell for their constant support, their hospitality, and the exiting atmosphere at the NSSP Branch.

Many thanks go to J. Garrett, P. A. Moss, H. F. Nieman, T. Eve, M. M. Potter, D. C. Tennant, R. L. Donaberger, G. A. Tapp, L. E. McEwan, and A. Hewitt for their expert technical assistance.

I would like to thank Drs. T. E. Mason, C. Broholm, R. Steeman and L. Rebelsky. Those four are young neutron scatterers who have contributed to my understanding of magnetic neutron scattering and to many discussions during our collaborative work on various projects.

It was equally enjoyable at McMaster. I would like to thank M. Wilby, D. Burrows, R. McNeice, and W. Mararek for their administrative and secretarial assistance. Four fellow students also deserve special mention, R. Rogge, J. G. Lussier, Y. Ning and C. Jiang helped me in various ways.

Special thanks go to Drs K. M. Hughes, B. D. Gaulin, N. C. Schmeing and H. Schmeing who over the course of this work provided so much support and warmness beyond words.

I would like to thank Dr. M. Hagen for his suggestions

to improve this thesis.

Finally, the financial assistance of McMaster University and the Canadian Investment Development Association is gratefully acknowledged. AECL Research has provided excellent facilities for performing the experiments.

TABLE OF CONTENTS

LIST OF FIGURES

LIST OF TABLES

CHAPTER 1: INTRODUCTION

1.1 General Outline

The nature of the magnetic ordering is a fundamental property of magnetic materials. This thesis involves the study of such ordering by the use of neutron scattering techniques for two materials, UNi_2Si_2 and erbium.

This chapter describes the microscopic origin of the magnetic ordering of f electron systems, the general features of magnetic structures and magnetic phase transitions. The magnetic ordering of two particular f electron systems, heavy rare earth metals and uranium transition metal silicides, will be summarized. In Chapter 2 the neutron scattering theory and techniques required for the study of magnetic ordering will be described. The particular experimental equipment and methods used are also included in Chapter 2. The experimental determination of the magnetic ordering for UNi_2Si_2 and Er will be presented in Chapter 3 and Chapter 4 respectively.

Several papers related to this thesis have been published in the refereed scientific literature[1-4]. Other work not covered in this thesis that has been performed during my study for the Ph.D degree are the neutron scattering study of the heavy fermion superconductor URu_2Si_2[5,6], and the Kondo lattice compound $CePd_2Si_2$[7].

1.2 General Physics of f Electron Systems

Both rare-earth and actinide systems show fascinating magnetic properties. They are characterized by the filling up of the 4f and 5f shells respectively, by a d shell filled by one or more electrons, and by a broad conduction band of s and p electrons. The magnetism arises from the f electrons in the partically filled shells. The interaction of these moments with d and sp electrons gives rise to the ordered magnetic states.

In the rare earths 4f electrons are well localized on the ion sites. However, the energy level of 4f electrons can be very different relative to the Fermi level of the sp and d band[8]. If the energy difference between them is large, the ionic model is a good approximation. The 4f electrons interact with each other only indirectly through the conduction electrons by the Ruderman-Kittel-Kasuya-Yosida (RKKY) mechanism. The heavy rare earths (Gd, Tb, Dy, Ho, Er, Tm) belong to this group. In addition, the orbital angular momentum of f elections interacts with the crystal electric fields at the ion sites. The spin-orbit coupling in the f shell is strong and the total angular momentum J is a good quantum number which can be determined by Hund's rules. The ionic magnetic moment in the ground state is given by $\mathbf{m}=-g_J\mu_B\mathbf{J}$ where g_J is the Lande factor and μ_B the Bohr magneton. If the 4f level is close to the Fermi level, as is the case for the

light rare earths Ce, Eu, and Sm, and for Y, the interaction between 4f and conduction electrons may be considered through a resonant scattering mechanism. The interaction between electrons may be dominated by the lattice Kondo effect which describes the conduction electron - spin exchange[9].

In contrast, the 5f electrons are relatively much less localized in light actinide. The magnetism only occurs in U, Np and Pu where there is a strong hybridization between the 5f and 6d electrons. Two kinds of interaction compete in actinides metals and compounds: the RKKY interaction which favours long-range magnetic ordering of the local f moments, and the Kondo effect which tends to reduce the local f moments[10].

Using the above physical picture as a starting point, a large amount of experimental and theoretical work has been concentrated on the magnetic ordering of f electron systems.

1.3 Magnetic Ordering

1.3.1 Magnetic ordering

At low temperatures the magnetic moments of materials form an ordered arrangement, a phenomenon known as magnetic ordering. The ordered arrangements are usually characterized by a Fourier expansion in reciprocal space. The lattice is described by atomic sites with a magnetic moment m at the site. Fourier transformation gives

$$\boldsymbol{m}_q = N^{-1}\sum_l \boldsymbol{m}_l \exp(i\boldsymbol{q}\boldsymbol{R}_l) \qquad (1.1)$$

where $\mathbf{R}_l$ is the position of the lth atom and there are N nuclear unit cells in the crystal, and $\mathbf{q}$ is a vector in the first Brillouin zone of the lattice.

For simple structures there is just one value of $\mathbf{q}$ where $\mathbf{m}_q$ is non zero, and complex structures show only a small number of values of $\mathbf{q}$ where $\mathbf{m}_q$ is non zero. These $\mathbf{q}$ are reciprocal lattice vectors in the magnetic unit cell, which in general is larger than the nuclear cell in real space. The magnetic cell need not be commensurate with the nuclear cell. In this thesis investigations will be described of some complicated magnetic structures, so we will describe initially the types of structure that we will be coming across.

1. **Ferromagnetism.** All the magnetic moments are parallel to each other and $\mathbf{m}_q$ is zero unless $\mathbf{q}=0$.

2. **Simple antiferromagnetism.** Successive moments point in opposite directions, which for simple structures give rise to $\mathbf{q}=\boldsymbol{\tau}/2$ where $\boldsymbol{\tau}$ is a nuclear reciprocal lattice vector.

3. **Incommensurate sinusoidal structures.** The magnetic lattice is incommensurate with the nuclear lattice, so that $\mathbf{q}$ is not a rational fraction of any of the vectors $\boldsymbol{\tau}$. For these structures

$$\boldsymbol{m}_l = A\cos(\boldsymbol{q}\boldsymbol{R}_l+\varphi)\,\hat{\boldsymbol{u}} \qquad (1.2)$$

with

$$\boldsymbol{m}_q = A\exp(i\varphi)\,\hat{\boldsymbol{u}}/2 \qquad (1.3)$$

These equations describe a spin density wave; that is a sinusoidally - modulated moment propagating along the **q** direction with amplitude A and phase φ. If **q** is parallel to $\hat{\mathbf{u}}$ it is a longitudinal wave and if **q** is perpendicular to $\hat{\mathbf{u}}$ it is a transverse wave. If q is a rational fraction of τ, the magnetic structure is commensurate with the nuclear one.

4. **Square-wave structures.** The magnetic lattice consists of blocks of moments along $\hat{\mathbf{u}}$ where within each block the moments are all either +**m** or -**m**. This is similar to the sinusoidal structures except that higher harmonics are usually needed to produce the squared-up structure, so that $\mathbf{m}_q$ is non zero at a value of n**q**, folded back into the first Brillouin zone if necessary.

5. **Helical structures.** Here

$$\boldsymbol{m}_l = A[\cos(\boldsymbol{q}\boldsymbol{R}_l+\varphi)\,\hat{\boldsymbol{u}} + \sin(\boldsymbol{q}\boldsymbol{R}_l+\varphi)\,\hat{\boldsymbol{v}}] \qquad (1.4)$$

where $\hat{\mathbf{u}}$ and $\hat{\mathbf{v}}$ are two orthogonal unit vectors and

$$\boldsymbol{m}_q = A\exp(i\varphi)\,(\hat{\boldsymbol{u}}+i\hat{\boldsymbol{v}})/2 \qquad (1.5)$$

More complicated magnetic structures can be combinations of the above. For instance, a cone structure consists of a helix and a ferromagnetic moment along an unit vector $\hat{\mathbf{z}}$ which is orthogonal to $\hat{\mathbf{u}}$ and $\hat{\mathbf{v}}$.

The magnetic structure arises from the minimization of the free energy of a system. The Hamiltonian term in the free energy has different forms for different systems, as will be discussed later. In the following two sections we will describe the magnetic structures of two specific systems of f electrons: the heavy rare earth metals and UT_2Si_2 where T is a transition metal.

1.3.2 Magnetic ordering in heavy rare earth metals

The heavy rare earth metals from gadolinium to thulium crystallize in the hexagonal close-packed (hcp) structure with a c/a ratio from 1.591 to 1.571, slightly smaller than "ideal" value 1.633. There are two atoms per unit cell at $\mathbf{R}=(0,0,0)$ and $\mathbf{R}=(1/3,2/3,1/2)$. The electronic configuration in an isolated atom is $4f^n6s^2$ for n=9-13 (terbium to thulium) and $4f^75d^16s^2$ for gadolinium. The magnetic ordering has already been reviewed by many authors[11-15], and this section will update these results.

Table 1.1 summarizes the magnetic ordering of the heavy rare earths. Tc, the ferromagnetic Curie temperature, is the critical temperature to a ferromagnetic alignment. T_N is the Neel temperature or the temperature of transition to a

non-ferromagnetic ordered state. T_{N1} refers to the ordering along the c axis, and T_{N2} refers to the ordering in the ab plane except for thulium where it is the temperature that the structure locks into the commensurate phase. m_f is the measured low-temperature saturation magnetic moment which is slightly larger than the value predicted from the Hund's rules' ground state $g_J J(\mu_B)$.

The common feature is that magnetic moments are parallel to each other in the hexagonal basal planes forming ferromagnetic sheets, and the ordering of these sheets is characterized by a wave vector **q** along the c axis. Incommensurate structures are formed at higher temperatures below T_N, and are transformed into ferromagnetic structures or commensurate structures with ferromagnetic components at lower temperatures. In holmium[16,17], erbium[18] and thulium[19], these incommensurate structures are locked into commensurate structures of the same type within certain temperature ranges. The c-axis modulated (CAM) structure can vary from a sine-wave to a square-wave along the c axis. This variation is marked by the harmonics of the modulation.

Recently, the spin-slips concept has been developed to model the commensurate structure with harmonics[16-21]. A c-axis spin-slip structure is such that spins with the blocks of four are parallel and antiparallel successively to the c axis, and spin-slips occur with blocks of three spins. A basal-plane

TABLE 1.1. Magnetic ordering of heavy rare earth metals. $\hat{m}$ is the direction of the moment. q is the value of wavevector (q//c). F stands for ferromagnet, c for cone, H for helix, CAM for c-axis modulated sturcture.

metal	T < Tc		Tc	Tc < T < T_{N2}		T_{N2}	T_{N2} < T < T_{N1}		T_{N1}	m_f	$g_J J$
	type	$\hat{m}$ q	(K)	type	$\hat{m}$ q	(K)	type	$\hat{m}$ q	(K)	(μ_B)	(μ_B)
Gd	F	m∥c(T) 0	293							7.55	7.0
Tb	F	m⊥c 0	220	H	m⊥c 0.097 -0.118	230				9.34	9.0
Dy	F	m⊥c 0	88	H lock-in	m⊥c 0.147 -0.235 1/7	176				10.33	10.0
Ho	C (F +H) lock-in	m_z//c m_{xy}⊥c 1/6	19	H lock-in	m⊥c 0.181 -0.282 2/9, 2/11	130				10.34	10.0
Er	C (F +H) lock-in	m_z//c m_{xy}⊥c 5/21	18	CAM ±m_z//c 0.250 + H m_{xy}⊥c -0.292 lock-in n(4n-1)$^{-1}$ n=∞,6,5,4,3,2		52	CAM ±m//c 0.292 -0.282		85	9.0	9.0
Tm				CAM ±m//c lock-in	2/7	32	CAM ±m//c 0.286 -0.272		57	7.14	7.0

spin-slip structure involves spins (or pairs of spins) that are distributed at 60° intervals in the basal plane around the hexagonal easy axis. Spin-slips involve a pattern where a spin is missing and the single spin lies on the easy axis. Some spin-slip structures have small net ferromagnetic moments, because there are an odd number of spins in the unit cell. This is the case, for example, for the repeating unit found in thulium for $q=2/7c^*$ and in erbium for $q=2/7c^*$, $4/15c^*$ and $6/23c^*$. For instance, the $q=2/7c^*$ structure consists of a block of four spins in one direction followed by a block of three spins in the opposite direction, giving a net moment of one

atomic moment for every seven atoms along the c axis.

From gadolinium to thulium, the magnetic structure can be ferromagnetic (Gd, Tb, Dy) with the direction of the moments either being at an angle with the c axis as a function of temperature (Gd) or in the ab plane (Tb, Dy); helical in the ab plane (Tb, Dy, Ho); conical, consisting of a helix in the ab plane and a ferromagnetic moment along c (Ho, Er); and CAM along c (Er, Tm). Spin-slip structures exist in those metals whose orbital angular momentum is large (Dy, Ho, Er, Tm). These complicated magnetic structures result from the competition between the exchange, crystal field anisotropy, and magnetostriction energies as will be discussed in chapter 1.3.4.

1.3.3 Magnetic ordering in UT_2Si_2 compounds

The intermetallic compounds UT_2Si_2 with T a 3d, 4d or 5d transition metal crystallize into the $ThCr_2Si_2$ tetragonal structure with space group I4/mmm, except for T = Ir, Pt and Au when the $CaBe_2Ge_2$ structure occur with space group P4/nmm. The arrangement of the atoms in a unit cell of the $ThCr_2Si_2$ structure is shown in figure 1.1. The uranium atoms occupy the 2a positions to form a simple body-centred tetragonal (bct) sublattice. The transition metal atoms are in the 4d positions and the silicon atoms in the 4e positions. The nearest neighbour U-U separation in these compounds always exceeds the

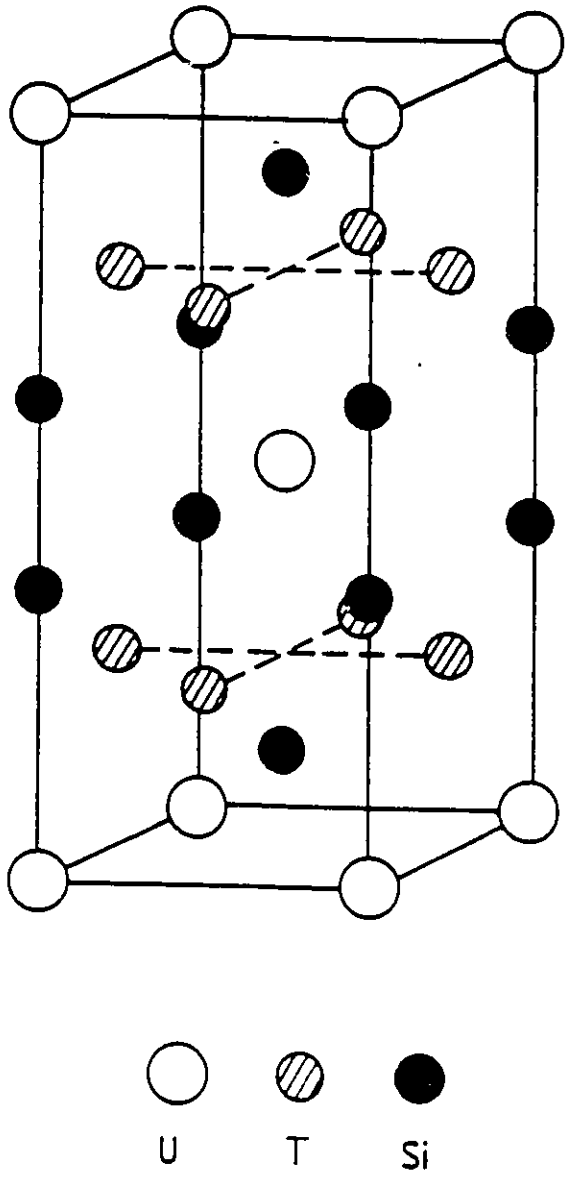

Figure 1.1 Tetragonal crystal structure of UT_2Si_2 compounds, where T can be most 3d, 4d, and 5d metals.

*Table 1.2. Magnetic ordering of UT_2Si_2 where T is a 3d, 4d and 5d transition metal. * lables $CaBe_2Ge_2$ crystal structure otherwise $ThCr_2Si_2$ structure.*

Mn	Fe	Co	Ni	Cu
375 F 0 4.72 1.14(U), 2.36(Mn)	- P	85 AF 1 4.85 1.42	103 96 53 AF F? LSW 1 2/3 2.90 2.89	107 103 AF F 1 0 3.58 1.61
T	Ru	Rh	Pd	Ag
T_N or $T_{C(K)}$ Ordering q m_{eff} (μ_B) m (μ_B)	17 AF 1 2.86 0.04	136 AF 1 3.06 1.96	150 97 40 LSW AF? AF 0.662 1 1 2.88 1.96	
Re	Os	Ir *	Pt *	Au *
- P	- P	5 AF 1 3.03	37 AF 1 3.22 1.67	78 48 18 LSW? ? AF? 3.11

Hill limit of 0.35nm[22]. The transition metal atoms appear to have no ordered moment except in the case of UMn_2Si_2. The ground state for U^{4+} with the electron configuration $[Rn]5f^2$ is $^3H_4$ according to Hund's rules.

Table 1.2 is a summary of the magnetic ordering of UT_2Si_2 with the data collected from the references 10 and 23-28. The magnetic structure marked AF is the simple body centred tetragonal antiferromagnet; this is the most commonly occuring magnetic structure. F stands for ferromagnet, LSW for longitudinal spin density wave, P for paramagnet. Cases with conflicting results in the literature are marked "?". The variety of magnetic structures shows the invalidity of the

Hill limit which predicts that large U-U separation leads to a magnetic ground state and that small separation leads to a non-magnetic ground state.

Like the heavy rare earths, the magnetic structures exhibit ferromagnetic sheets in the ab plane which are ordered with a wave vector **q** along c. However the moments are also along c instead of three dimensional. With an increasing number of d electrons, the compounds show a trend from Pauli-paramagnetism via simple antiferromagnetism to a modulated spin density wave.

The effective moment m_{eff} in table 1.2 is from the paramagnetic Curie-Weiss susceptibility. Except for the manganese and cobalt compounds, the uranium moments are around $3\mu_B$ which is smaller than expected from the free-ion magnetic moment of $3.58\mu_B$. The ordered moment m is different from m_{eff} in most compounds. For instance, the ordered moment in URu_2Si_2 is $0.04\mu_B$ below 17K. This difference may arise from the Kondo screening of the local moments.

1.3.4 The Hamiltonian

An understanding of this variety of magnetic structures is conventially sought in terms of the interactions described by the Hamiltonian[29]:

$$H = H_{ex} + H_{cf} + H_{me} + H_{af} \qquad (1.6)$$

where H_{ex} stands for the exchange contribution, H_{cf} for the crystal field contribution, H_{me} for the magnetoelastic or magnetostriction contribution, and H_{af} is the term due to the presence of an applied field.

1. The exchange contribution consists of the isotropic Heisenberg term and an anisotropic term in the heavy rare earths.

$$H_{ex} = -\sum_{i \neq j} J(\boldsymbol{R}_i - \boldsymbol{R}_j)\boldsymbol{J}_i\boldsymbol{J}_j - \sum_{i \neq j} K_{ij}(\boldsymbol{R}_i - \boldsymbol{R}_j)\boldsymbol{S}_i\boldsymbol{S}_j[[\boldsymbol{L}_i(\boldsymbol{R}_i - \boldsymbol{R}_j)]^2 + [\boldsymbol{L}_j(\boldsymbol{R}_i - \boldsymbol{R}_j)]^2] \quad (1.7)$$

where $\mathbf{J}_i = \mathbf{L}_i + \mathbf{S}_i$ is the total angular momentum operator for the ith ion, $J(\mathbf{R}_i - \mathbf{R}_j)$ is the RKKY interaction that is long range and oscillatory in character. $K_{ij}(\mathbf{R}_i - \mathbf{R}_j)$ is the anisotropic exchange. It takes into account the nonspherical part of f wave function which results in particular exchange mechanics, quadruple-quadruple, for example.

The exchange energy is the dominant term in the determination of the periodicity of magnetic structure because the magnetic structure is described by a wave vector $\mathbf{q}$ that maximizes $J(\mathbf{k})$ and $K(\mathbf{k})$ which are defined as the Fourier transforms of the interactions,

$$J(\boldsymbol{k}) = \sum_i J_{ij} \exp(i\boldsymbol{k}(\boldsymbol{R}_i - \boldsymbol{R}_j)) \quad (1.8)$$

and

$$K(\boldsymbol{k}) = \sum_{i} K_{ij} \exp(i\boldsymbol{k}(\boldsymbol{R}_i - \boldsymbol{R}_j)) \qquad (1.9)$$

The modulation of magnetic structure results from the oscillation of the exchange interaction.

The Fourier transform of the exchange interaction depends on the band structure and the susceptibility of the conduction electrons. Because of the interaction between the local f moments and the spins of the conduction electrons, the periodic magnetic ordering perturbs the conduction electron bands. The conduction electrons experience a potential with different period from the lattice and hence produce magnetic superzone gaps at the Fermi surface in the bands[30]. As the temperature varies, the Fermi surface changes, and the $J(\mathbf{k})$ is modified. Consequently the wave vector $\mathbf{q}$ determined from the maximum value of $J(\mathbf{k})$ changes. The coalescing of superzone gaps will lower the exchange energy and cause a discontinuous change in the Fermi surface. This is one of reasons that the magnetic structure becomes commensurate.

The Anderson Hamiltonian is applied for uranium compounds, which describes the case of strong d-f electron hybridization[10,31]. The RKKY interaction is also valid to give the modulation of the magnetic structures.

2. The crystal field contribution caused by each ion seeing the other charged ions has the general form:

$$H_{cf} = \sum_i \sum_{l,m} B_l^m O_l^m(J_i) \qquad (1.10)$$

where $O_l^m(J_i)$ are the Stevens operator equivalents of spherical harmonics and B_l^m the Steven factors[32]. The crystal field tends to align the charge clouds and hence the magnetic moments of the f electron relative to the crystal axis. It exhibits the local symmetry of the ionic lattice. The macroscopic form of eqn (1.10) for hexagonal symmetry is

$$E_{hex} = K_2^0 Y_2^0(\theta,\varphi) + K_4^0 Y_4^0(\theta,\varphi) + K_6^0 Y_6^0(\theta,\varphi) + K_6^6 \sin^6\theta \cos 6\varphi \qquad (1.11)$$

where θ and φ are the angles of magnetization relative to the c and a-axis. K_l^0 terms describe the dominant uniaxial anisotropy, while the K_6^6 term describes the basal plane anisotropy. Positive values of K_l^0 favour the alignment of the moments in the basal plane and negative values favour the c axis. The observed and calculated K_l^0 is positive for Tb, Dy and Ho and negative for Er and Tm. The magnetic ordering shows that the moments of the first three align in the basal plane and the last two along c. The crystal field anisotropy is one of the main factors in determining the direction of the moment.

In tetragonal uranium compounds, the crystal field anisotropy acts to align the moments perpendicular to the ab plane.

3. The magnetostriction describes the coupling between the magnetization and the crystal deformation. The magnetoelastic contribution can be written down in terms of the equilibrium strains and the magnetostriction coefficients.

$$H_{me} = \sum_{\Gamma,i} B^{\Gamma,i} S^{\Gamma,i} \varepsilon^{\Gamma,i} \qquad (1.12)$$

where $\varepsilon^{\Gamma,i}$ is the irreducible strains, $B^{\Gamma,i}$ the magnetoelastic coupling constants and $S^{\Gamma,i}$ the linear combination of Stevens operators.

Since the anisotropy and magnetic moments are large in rare earths, large magnetostriction effects are expected. They play the key role as the basic driving force behind the ferromagnetic transition in Tb and Dy and the incommensurate-commensurate transitions in Ho, Er and Tm.

The magnetoelastic contribution may be less important in the UT_2Si_2 system because the moments are not large and the lattice deformation on ordering is small.

4. The applied field contribution can be simply expressed by the Zeeman energy:

$$H_{ap} = -g_J \mu_B \sum_i \boldsymbol{H} \boldsymbol{J}_i \qquad (1.13)$$

For sufficiently large fields a ferromagnetic arrangement will be reached. However, various intermediate types of magnetic ordering can be induced by the field. For example, the fan or helifan structures are observed in Ho when the field is applied in the ab plane[15].

The Hamiltonian is very complicated. The entire theory for heavy rare earths has been extensively studied by Callen and Callen[33], Coqblin[11], Cooper[34], Elliott[35], Nagamiya[36], Yosida and Miwa[37], and Jensen and Mackintosh[15]. The theory for uranium compounds has been studied by Cooper[31], Coqblin[8] and others.

Considering the large anisotropy in these systems and that the moments form ferromagnetic sheets, a simplified phenomenological Hamiltonian was suggested by Elliott[38].

$$H = -\sum_{ij} [J_{ij} J_i^z J_j^z + J'_{ij} (J_i^x J_j^x + J_i^y J_j^y)] \qquad (1.14)$$

where $J'_{ij}=0$ for moments align along c and $J_{ij}=0$ for moments align in the basal plane. Many subsequent studies have concentrated on the Ising-like system ($J'_{ij}=0$)[34]. The Fourier transform of J_{ij} has a simple form if the interactions between layers are taken with only nearest-neighbour J_1 and next-nearest-neighbour J_2 considered.

$$J(k) = J_0 + 2J_1 \cos(2\pi kd) + 2J_2 \cos(4\pi kd) \qquad (1.15)$$

where J_0 is the interplane interaction and d is the distance between planes. If the intraplane interactions are larger than the interplane ones and the exchange is Ising in character, the model is called the axial-next-nearest-neighbour Ising (ANNNI) model. Although no real system exactly corresponds to this model,it has the virtue of being soluble by approximate methods. It predicts a rich array of magnetic structures, with incommensurate-commensurate phase transitions.

1.4 Phase Transitions

1.4.1 Phase transitions

When a system changes phases we say that there has been a phase transition. This may be from a disordered to an ordered state, or from one ordered state to another. The transitions are accompanied by large changes or anomalies at the phase transition temperatures in experimental observables such as the specific heat, susceptibility, resistivity, and magnetization.

There are two types of phase transitions: first order and critical (second order) phase transitions.

For the first order phase transition, the first derivative of the Gibbs free energy is discontinuous at the transition, so there is a latent heat. The existence of a hysteresis effect is a sufficient condition of the phase transition to be of first order. If the phase transition can

be described in terms of an order parameter η, as defined in Ginzberg-Landau theory, then this parameter drops to zero discontinuously with the temperature on going from the ordered to the disordered state.

For the critical phase transition, the Gibbs free energy is nonanalytic at the transition point and no hysteresis exists. The order parameter is a continuous function of temperature. This transition involves the ordering such that fluctuating micro-regions of both phases are involved. As the critical point is approached, the correlation length, defined as the linear extent of these regions, tends to infinity, and the response time of the system also tends to infinity.

In magnetic systems, the experimental observables, magnetization M, susceptibility χ, specific heat c_H and correlation length ξ obey power laws as a function of reduced temperature, $t = (T-Tc)/Tc$, when the critical point is approached.

$$M \propto \begin{cases} (-t)^{\beta} & t<0 \\ 0 & t>0 \end{cases} \qquad (1.16)$$

$$\chi_{q=0} \propto \begin{cases} t^{-\gamma} & t>0 \\ (-t)^{-\gamma'} & t<0 \end{cases} \qquad (1.17)$$

$$C_H \propto \begin{cases} t^{-\alpha} & t>0 \\ (-t)^{-\alpha'} & t<0 \end{cases} \qquad (1.18)$$

$$\xi \propto \begin{cases} t^{-\nu} & t>0 \\ (-t)^{-\nu'} & t<0 \end{cases} \qquad (1.19)$$

The critical exponents, the indices of the power laws, obey certain relations called scaling laws; and depend only on the following three properties (hypothesis of universality):

1. The dimensionality of the system, d.

2. The dimensionality of the order parameter, D.

3. The character of the coupling of the local variables. Examples of such character would be short range interactions, long range interactions and interactions with a random component.

Any particular value of the above properties determines a universality class. In a real system, a crossover may occur from the critical behaviour of the original universality class to that of a new universality class[40]. The critical phase transitions have been studied in detail by Stanley[41] and Collins[42].

1.4.2 Phase transitions in heavy rare earth metals and UT_2Si_2 compounds

As discussed in Chapter 1.3.2, most heavy rare earths

Table 1.3. Critical exponents of heavy rare earth metals.

Metal	β	γ	ν	α
Gd				
Tb	0.25; 0.33			
Dy	0.39 (+0.04, -0.02)	1.05 (±0.07)	0.57 (±0.05)	
Ho	0.39 (+0.04, -0.03)	1.14 (±0.10)	0.57 (±0.04)	
theory	0.39	1.39	0.70	-0.17
Er	0.39			
Tm	0.25-0.30 (± 0.05)	1.33 (± 0.02)	0.66 (± 0.02)	
theory	0.35			

have at least two magnetic phase transitions. The transition from the paramagnetic state to an ordered magnetic state is usually a critical phase transition. Transitions from the antiferromagnetic state to a ferromagnetic state are first order. The measured critical exponents for the transition to paramagnetism are given in table 1.3. The data are collected from references 19, 42, 43 and 43a.

Usually theories predict the heavy rare earth metals in the universality class with d=3, D=2 or 4, and long range forces[44]. D is defined as a product of dimensionality of spins and of the wave vector, $\mathbf{q}=\pm(0,0,q_z)\mathbf{c}^*$, the latter being two. Just below the phase transition from the paramagnetic to the

ordered state, D=4 for Tb, Dy and Ho since the spins are in the basal plane, and D=2 for Er and Tm since spins are only along the c axis. The Landau-Ginzburg-Wilson model with d=3 and D=4[45,46] predicts the critical exponents ν=0.70, β=0.39, γ=1.39 and α=-0.17. Theoretical values are β=0.33 for D=2 model. Comparing with table 1.3, Dy and Ho agree satisfactorily but the other cases do not show agreement for β.

Much less work has been reported on the UT_2Si_2 system. Mean field behaviour with β=1/2 was observed in URu_2Si_2 indicating long range forces[47].

CHAPTER 2: NEUTRON ELASTIC SCATTERING

Neutron scattering is an invaluable probe of the magnetic structure and phase transitions. The neutron has a magnetic moment and is a neutral particle so that it can penetrate into the bulk of a specimen. Thermal neutrons have both wavelengths (1-3Å) and energies (10-80 meV) comparable with interatomic distances and thermal excitations in crystals. Because of these properties thermal neutrons interact with matter in two ways, namely, (1) the interaction with the nucleus via short-ranged nuclear forces, and (2) the interaction between the magnetic moments of the neutron and of the matter via long-ranged magnetic forces. Scattering by these mechanisms is called nuclear scattering and magnetic scattering respectively. This chapter will introduce the results of neutron scattering theory and describe the experimental techniques used in the present work, the references are 42, 48-52.

2.1 Nuclear and Magnetic Bragg Scattering

2.1.1 Bragg scattering formalism

Neutron elastic scattering is scattering where the energy of the incident and the scattered neutron are identical; in another words the energy transfer is zero.

The quantity measured in the elastic scattering is the differential cross section, the probability of scattering into a solid angle $d\Omega$. The differential cross section $d\sigma/d\Omega$ can be calculated by quantum scattering theory. If $|\mathbf{k}\sigma\lambda\rangle$ ($|\mathbf{k}'\sigma'\lambda'\rangle$) is the initial (final) state of the system, where $\mathbf{k}$ is the neutron wavevector, σ labels the spin state, and λ is the quantum state of the target, then

$$\frac{d\sigma}{d\Omega} = \left(\frac{2\pi m}{h^2}\right)^2 |\langle k'\sigma'\lambda' | V | k\sigma\lambda\rangle|^2 \qquad (2.1)$$

where V is the interaction potential between the neutron and the target.

If the neutron is scattered from a lattice having N unit cells, the neutron sees the structure of the lattice through a mean periodic potential for each cell. Then the differential cross section will reflect the symmetry of the lattice and will be determined by the mean periodic potential.

$$\frac{d\sigma}{d\Omega}(Q) = N\frac{(2\pi)^3}{v_0}\sum_{\tau}\delta(Q-\tau)|V(Q)|^2 \qquad (2.2)$$

where $\mathbf{Q}=\mathbf{k}-\mathbf{k}'$ is the scattering vector, the momentum transfer of the neutron to the lattice. For elastic scattering, $|\mathbf{k}| = |\mathbf{k}'| = k$. v_0 is the volume of the unit cell. τ is the reciprocal lattice vector of the unit cell, and $|V(Q)|^2$ is determined by the mean periodic potential. All quantities of the lattice are referred to the crystallographic unit cell for the nuclear

scattering and to the magnetic unit cell for the magnetic scattering.

The scattering will be zero unless $\mathbf{Q}=\boldsymbol{\tau}$, as required by the δ function in eqn (2.2). This is the Bragg relation. If the angle between the wave vectors of the incident and scattered beams is 2θ, then the Bragg relation can be written as

$$\lambda = 2d\sin\theta \tag{2.3}$$

where $\lambda=2\pi/k$ is the neutron wavelength, d is the spacing of planes in the lattice, with

$$|Q| = |\tau| = \frac{2\pi}{d} \tag{2.4}$$

A reciprocal lattice vector of the nuclear unit cell is given by

$$\tau_N = h\mathbf{a}^* + k\mathbf{b}^* + \ell\mathbf{c}^* \tag{2.5}$$

or

$$\tau_N = (h,k,\ell)$$

and a reciprocal lattice vector in the magnetic unit cell can be expressed by

$$\tau_M = \tau_N + \mathbf{q} \tag{2.6}$$

where $\mathbf{q}$ is a reduced magnetic wave vector, defined in Chapter 1.

For nuclear scattering, eqn (2.2) gives the coherent scattering which arises from the mean scattering length for each atom in the crystal lattice. The incoherent scattering arises from the random isotope distribution and the random nuclear spin orientation. It is isotropic and contributes a

uniform background scattering. The V(Q) of eqn (2.2) for the nuclear Bragg scattering is called the nuclear structure factor. It is given by

$$V(Q) = F_N(Q) = \sum_\ell \bar{b}_\ell \exp(iQR_\ell) \exp(-W_\ell) \qquad (2.7)$$

where the sum over ℓ is to be taken over all the atoms (at position R_ℓ) in the nuclear unit cell. $\bar{b}_\ell$ is the mean scattering length. The term $\exp(-W_\ell)$ is the Debye-Waller factor which is due to thermal vibration effects.

The magnetic scattering comes from the interaction of the neutron magnetic moment with the local magnetic field. The general form of $|V(Q)|^2$ in eqn (2.2) is given by

$$|V(Q)|^2 = \sum_{\alpha\beta} (\delta_{\alpha\beta} - \hat{Q}_\alpha \hat{Q}_\beta) F_\alpha^*(Q) F_\beta(Q) \qquad (2.8)$$

where $\hat{Q}_\alpha = Q_\alpha/|Q|$ is the direction cosine of Q along the α axis, and $F_\alpha(Q)$ is known as the magnetic structure factor, given by

$$F_\alpha(Q) = \left(\frac{\gamma r_0}{2}\right) \sum_\ell m_\ell^\alpha f_\ell(Q) \exp(iQR_\ell) \exp(-W_\ell) \qquad (2.9)$$

The sum over ℓ is over all the magnetic atoms (at position $\mathbf{R}_\ell$) in the magnetic unit cell. $f_\ell(\mathbf{Q})$ is the magnetic form factor of the ℓth magnetic ion, the Fourier transform of the atomic magnetization density. It is a function of Q and $f_\ell(Q=0)=1$. The constant $\gamma r_0/2=0.27\times10^{-12}$cm represents the scattering amplitude at Q=0 for a single magnetic moment of 1 μ_B. It is of about the same magnitude as the nuclear scattering length, so the magnetic scattering can be easily measured. The polarization factor in eqn (2.8), $\delta_{\alpha\beta}-\hat{Q}_\alpha\hat{Q}_\beta$, reflects the fact that the neutron only sees the moment perpendicular to the scattering vector. This gives the possibility of determining the orientation of the magnetic moments in the magnetic lattice. m_ℓ^α is the thermal average value of the component of the magnetic moment of the ℓ'th atom, $m_\ell^\alpha \equiv <\mu_\ell^\alpha>$.

2.1.2 Bragg scattering from f electron systems

Since the f electron systems described in this work always have magnetic layer structures with **q** parallel to **c** it is convenient to describe the differential cross section into two parts: a part arising from the component of the moment along the c axis and the part from the component perpendicular to the c axis. The eqn (2.2) can be written as

$$\frac{d\sigma}{d\Omega}(\mathbf{Q}) = N\frac{(2\pi)^3}{v_0}\sum_{\tau}\delta(\mathbf{Q}-\tau)\,(|V_z(\mathbf{Q})|^2+|V_{xy}(\mathbf{Q})|^2) \qquad (2.10)$$

If there is only one kind of magnetic ion, eqns (2.8) and (2.9) become

$$|V_z(Q)|^2 = (\frac{\gamma r_0}{2})^2 f^2(Q) \exp(-2W)(1-\hat{Q}_z^2)|F^z(Q)|^2 \qquad (2.11)$$

and

$$|V_{xy}(Q)|^2 = (\frac{\gamma r_0}{2})^2 f^2(Q) \exp(-2W)\,[(1-\hat{Q}_x^2)|F^x(Q)|^2 + (1-\hat{Q}_y^2)|F^y(Q)|^2] \qquad (2.12)$$

with

$$F^j(Q) = \sum_l m_l^j \exp(iQR_l) \qquad j=x,y,z \qquad (2.13)$$

These equations allow for the calculation of the elastic scattering for any given arrangement of the moments. To determine the structure from the observed scattering is a more difficult problem. The solution involves two steps, separation of the scattering into z and xy components and then solving for each component. The former problem is soluble in principle for structures with ferromagnetic layers; the latter problem is difficult because only the magnitude of the magnetic structure factor can be determined , not its phase. The magnetic wave vector **q** will be identified from the experiment.

2.2 Measurements of Bragg Scattering in Single Crystals

2.2.1 The scattering methods

There are two ways to measure Bragg scattering from

single crystal samples.

Laue method

A single crystal with fixed orientation accepts neutrons with different wavelengths and scatters those with one particular wavelength in one particular direction which satisfies the geometry of Bragg scattering. This technique is called the Laue method. Such single crystal scattering is used for two important parts of a neutron instrument: the monochromator, to select neutrons of a particular wavelength from a reactor or a pulsed neutron source; the analyzer, to analyze the wavelength of scattered beam from the sample. The latter can be used to provide a series of wavevectors at different time in the inelastic scattering so the energy spectrum of the scattered beam can be measured. For elastic scattering, the use of an analyzer set to the elastic scattering energy may improve the accuracy of measurement, by eliminating the inelastic component of the scattering.

Crystal rotation method

This technique is normally used to determine the arrangement of the atoms within a crystal. The single crystal is rotated in an incident monochromatic neutron beam and scattered neutrons are detected by a counter at a fixed angle which satisfies the geometry of the Bragg scattering.

2.2.2 The scattering intensity

Before giving the formula for the scattering

intensity, the concepts of collimation, mosaic spreads, instrument resolution and the Lorentz factor are described.

Collimation

The process of limiting the angular spread of a beam of particles is called collimation. The actual angular spread of the beam is called the collimation angle. A common method of limiting this angle to a value of less than the solid angle submitted by the source at the sample is to use a Soller slit. This is composed of many parallel absorbing slits, located in the neutron flight path. The collimation of a Soller collimator is determined by the ratio of the slit separation to their length.

Mosaic spreads

A real single crystal cannot be a perfect lattice of infinite extent. There are almost always small mosaic blocks distributed in the crystal. Those mosaic blocks are perfect by themselves but are slightly misoriented from one to another, which give the orientation of the lattice a small angular spread known as the mosaic spread. Usually crystals have mosaic spreads in the range of one minute to a few degrees.

Resolution

Because of the collimation and mosaic spreads the momentum transfer Q and energy transfer ω can not be perfectly defined. The uncertainty in Q and ω can be described by the spectrometer resolution function. If the angular spreads form

Gaussian distribution functions, the resolution is also Gaussian with the surfaces of the constant intensity forming ellipsoids in the four dimensional (Q,ω) space. For elastic scattering, the surface only exists in Q space.

Lorentz factor

In an experiment the integrated intensity of a Bragg peak is measured by tracking through that Bragg peak at a constant rate along some path in reciprocal space. For instance the path may be an arc of a circle as produced by rotating the crystal at a fixed scattering angle, or may be along a linear path in reciprocal space. The Lorentz factor is the expression which relates the intensity of peak to the path taken in reciprocal space. If a scan is performed along a line at angle α to the wave vector transfer in constant wave vector steps, the Lorentz factor $\mathcal{L}(\theta)$ by using a diffractometer is given by

$$\mathcal{L}(\theta) = (\sin(\theta+\alpha))^{-1} \qquad (2.14)$$

where θ is the Bragg angle. The case of $\alpha=0$, $\pi/2$ and θ corresponds to the scan taken along Q, perpendicular to Q and rocking 2θ respectively.

For a triple-axis spectrometer, the Lorentz factor for the integrated intensity also depends on the resolution. The expression for $\mathcal{L}(\theta)$ is more complicated (see Appendix[17,53]).

Bragg scattering intensity

Due to the instrumental resolution, what the experiment sees in Bragg scattering is not a δ function but a peak with finite width. Experimentally we change some experimental parameters in order to let the scattering pass through the Bragg condition. The intensity of the Bragg peak at the scattering vector Q is given by

$$I(\mathbf{Q}) = c\mathcal{L}(\theta)|V(\mathbf{Q})|^2 \qquad (2.15)$$

where c is a normalization factor which takes into account all of the factors that remain constant during the experiment. The normalization factor c is proportional to the incident neutron flux, and the volume of the crystal, and increases as the wavelength increases. $|V(\mathbf{Q})|^2$ is defined by eqn (2.2) and depends only on the measured crystal or magnetic structure of the sample. $\mathcal{L}(\theta)$ is the Lorentz factor. By comparing the measured intensity of the nuclear peak with the square of the nuclear structure factor, the normalization factor can be determined. In order to determine the magnetic structure of the sample, the magnetic intensity is normalized to the intensity of the nearest nuclear peak. Equation (2.15) is valid for both the peak intensity and the integrated intensity of the Bragg peak, but c and $\mathcal{L}(\theta)$ may be different in the two cases.

The scattering intensity from a single crystal sample

is also effected by extinction and absorption.

The main effect of extinction is that stronger reflections are weakened so that the intensity of scattering is no longer proportional to the structure factor and the volume of the sample. The attenuation of the neutron beam in primary extinction results from the process of reflection by successive planes of a perfect crystal, while in secondary extinction it results from the neutron beam encounting blocks with similar orientations in different mosaic blocks. Since Bragg scattering intensity increases as the wavelength increases, single crystal measurements should be performed with a neutron wavelength as small as possible.

Some elements have large absorption cross sections, whose value is proportional to the wavelength. The observed intensity will be reduced by a factor $A(\theta)$ with

$$A(\theta) = \int \frac{1}{V} e^{-\mu x} dV \qquad (2.16)$$

where the integral is over the sample, V is the volume, x is the path length of the neutron through the sample for a given Bragg angle θ, and μ is the linear absorption coefficent. It is given by

$$\mu = \frac{1}{v_0} \sum_{i=1}^{n} \sigma_i^a \qquad (2.17)$$

if one unit cell contains n atoms with the absorption cross section σ_i^a for the ith atom. The absorption effect can be reduced through working with short wavelengths and a small crystal. Use of a spherical or cylindrical crystal enables the absorption correction to be calculated with some assurance.

2.3 Triple-Axis Spectrometer (TAS)

The triple-axis spectrometer is an instrument which can be used for both neutron elastic and inelastic scattering. It consists of a monochromater, a rotating sample table, an analyzer, detectors and collimators. The three axes are those of the monochromator drum, sample table, and analyzer crystal at each of which the neutron is scattered. Figure 2.1 shows the basic configuration of the N5 triple-axis spectrometer at NRU reactor in the Chalk River Laboratories.

Four collimators, namely C_0, C_1, C_2 and C_3, are located in the neutron flight path from the reactor to the monochromator, the monochromator to the sample, the sample to the analyzer, and the analyzer to the detector respectively. The horizontal collimation of these Soller slits is typically in the range of 0.2°-2.0°, and the vertical collimation is about 10°. Therefore the out of plane components of the neutron wavevectors are much less well defined than those in the plane. The experiments are normally performed in the horizontal plane.

D_1, D_2 and D_3 are neutron detectors. D_1 and D_2 are low-sensitivity monitors for the main beam from the reactor and for the diffracted beam just after monochromator. The monitor contains of a thin layer of natural uranium. Neutrons are detected by the ^{235}U fission reaction with an efficiency of about 10^{-5}. D_3 is a ^3He gas detector used for detecting the scattered neutrons. A ^3He nucleus captures a neutron and becomes a proton and a triton. The proton produces ionization in the ^3He-^4He mixture. The ionization cloud is detected by means of the electrical pulse which is counted with the high efficiency of between 60 and 90%.

Thermal neutrons from a reactor have a Maxwellian spectrum of energies. This "white" beam falls on to the monochromator (M), and the neutrons with the particular wave vector $\mathbf{k}$ selected by Bragg scattering off the monochromator with the scattering angle $2\theta_M$ fall on to the sample (S). The orientation of the sample in the scattering plane is given by the angle ψ. Neutrons scattered from the sample with the wave vector $\mathbf{k}'$ and the scattering angle φ fall on to the analyzer (A), and those with the wave vector corresponding to the angle $2\theta_A$ may be Bragg-reflected by the analyzer into the detector. $2\theta_M$ is the angle between the two collimators C_0 and C_1, and $2\theta_A$ the angle between C_2 and C_3. As the collimator C_1 rotates through $2\theta_M$ the monochromator must rotate by θ_M in order to maintain the correct reflecting condition; a similar condition

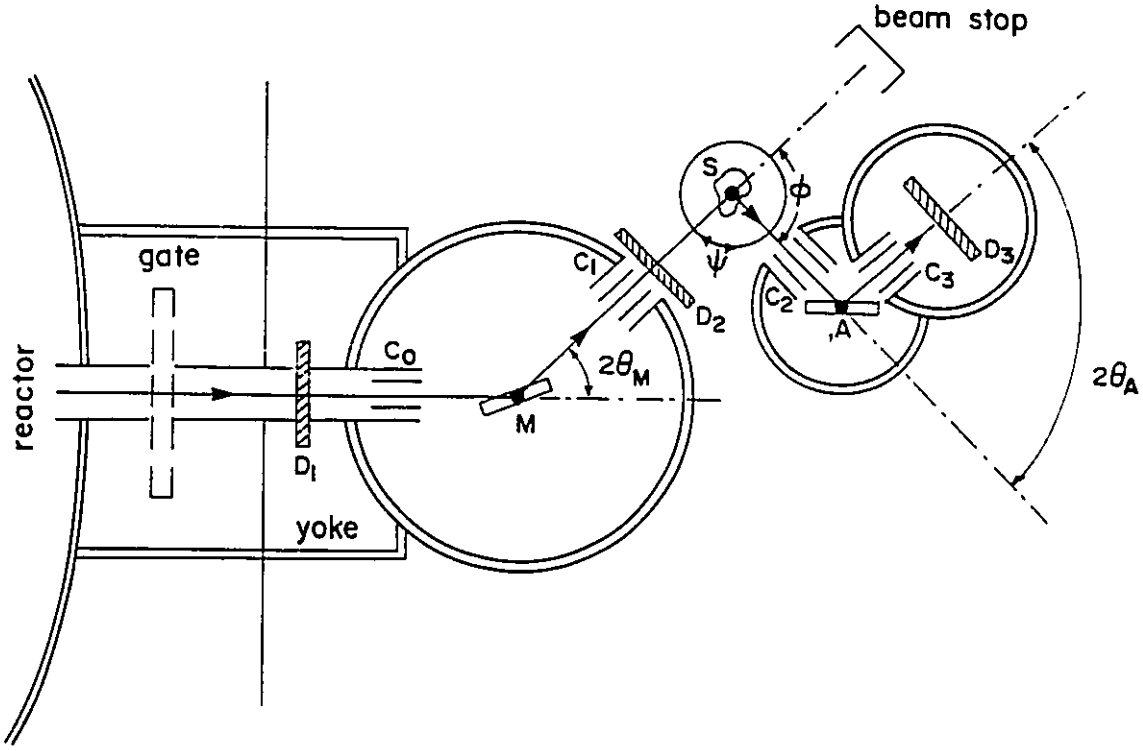

Figure 2.1 The neutron triple-axis spectrometer. Thermal neutrons from the reactor fall on to the monochromator (M) and are Bragg scattered with the angle $2\theta_M$ on to the sample (S). Neutrons scattered from the sample with the scattering angle φ fall on to the analyzer (A), and are Bragg scattered with the angle $2\theta_A$ on to the detector.

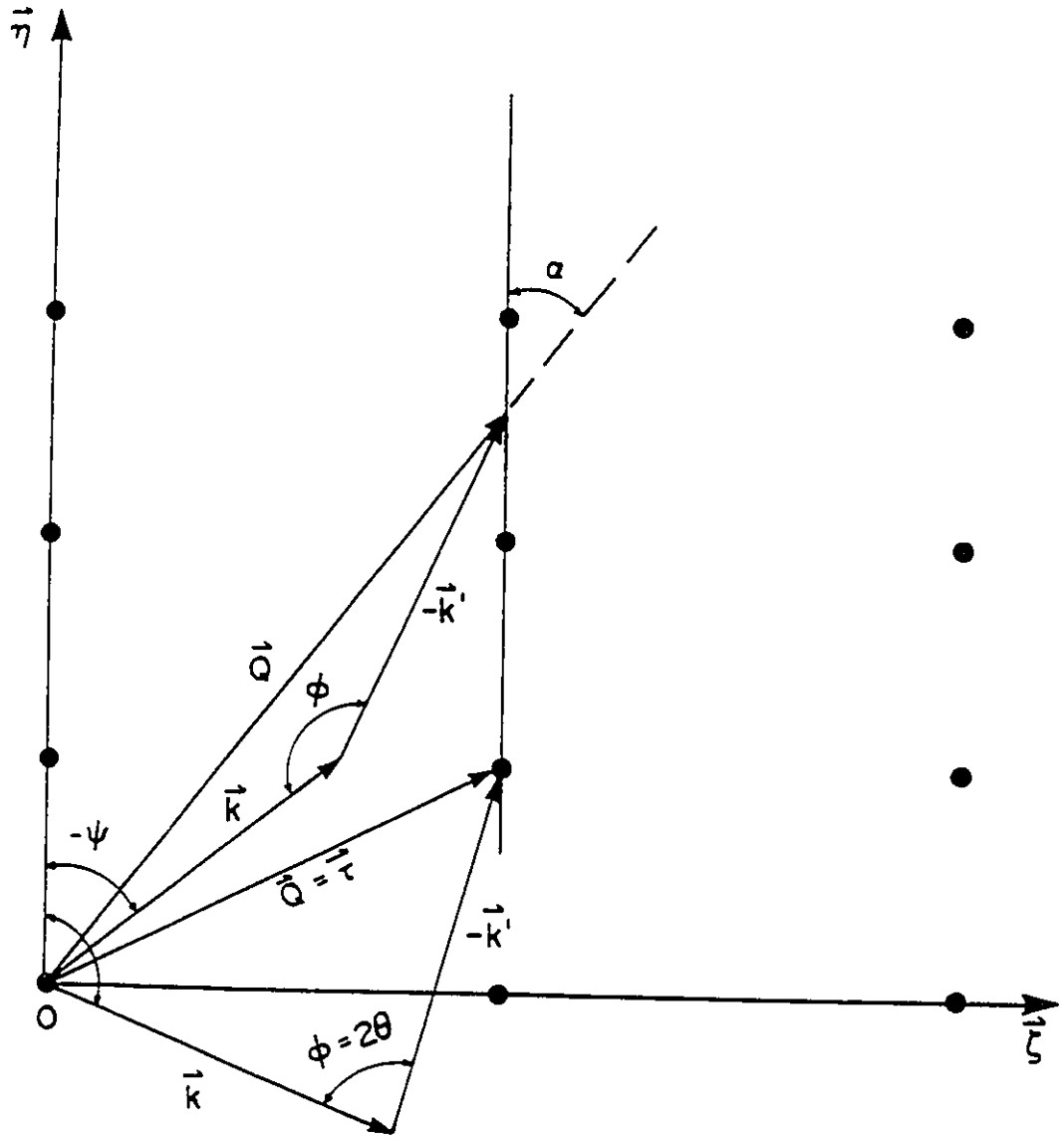

Figure 2.2 Scattering geometry of triple-axis spectrometer in reciprocal space. The monochromator scatters neutrons from the reactor with the wave vector **k**. The analyzer scatters neutrons from the sample with the wave vector **k′**. Bragg scattering occurs when the scattering angle $\varphi=2\theta$ and $|\mathbf{k}|=|\mathbf{k}'|$. α is an angle between the scattering vector **Q** and the η axis.

applies to reflection from the analyzer. For Bragg scattering by the sample, $\varphi=2\theta$ with θ the Bragg angle. Figure 2.2 shows the geometry in reciprocal space.

An advantage of the triple-axis spectrometer is that it can be configured in different ways to perform different measurements. In addition to "constant Q" and "constant E" modes for inelastic scattering, diffraction is performed by scanning the φ angle with the analyzer arm in the straight-through position (C_3 parallel to C_2) and with the analyzer removed. Elastic scattering is performed by scanning the φ angle with the magnitude of the analyzer wave vector $\mathbf{k}'$ fixed equal to the value of the incident wave vector $\mathbf{k}$, i.e. $\omega=0$.

A disadvantage of TAS is that the monochromator and the analyzer do not reflect a truly monochromatic beam. This is because for the same Bragg angle of the M (or A), not only neutrons with wavelength λ are reflected from the (hkℓ) plane, but also those with wavelengths λ/n, with n any integer, are reflected from the (nh nk nℓ) plane. Therefore the beam designed for wavelength λ will have contamination at wavelengths λ/n for $n=2,3,4,\ldots$. In addition, the monochromator and the analyzer will scatter some neutrons of all wavelengths through all angles because of incoherent and inelastic scattering processes. These difficulties can be overcome in several ways. For Laue scattering, the intensity is proportional to $(\lambda/n)^4$. The peak of the Maxwellian, for

example, for a temperature of 320K occurs at a wavelength of 1.40Å. Therefore if λ is much less than the value at the peak of Maxwellian, there will be no intensity at wavelength λ/n.

Monochromators and analyzers are often made from large single crystals of materials such as silicon, germanium, copper, pyrolytic graphite and beryllium which have very small absorption and incoherent cross sections. $\lambda/2$ contamination can be eliminated by choosing the (111) and (113) reflections from Si or Ge. These have a diamond structure whose second order (n=2) reflections (222) and (226) have zero structure factor.

Another technique is to put a filter in the incident or scattered beam. Be filters are only transparent to neutrons with a wavelength larger than a cut-off wavelength of 3.92Å, and pyrolytic graphite filters only have windows of transmittance with wavelengths around 2.37Å, 1.55Å and 1.39Å. The $\lambda/2$ or $\lambda/3$ contamination does not fall in the set windows and so is not transmitted through the filter.

2.4 The Experimental Technique

The neutron diffraction measurements in this thesis were carried out on a triple-axis spectrometer, in elastic scattering mode, at the NRU reactor of the Chalk River Laboratories. Table 2.1 lists the experimental configurations employed. An incident neutron wavelength of 2.37Å was used in

conjunction with a pyrolytic graphite filter in the scattered beam.

The samples were aligned with the certain reciprocal plane horizontal and mounted in a displex refrigerator. Calibrated carbon temperature sensors were located on the aluminum sample holder in the cryostat, and the temperature was usually controlled to about 0.1 K.

Measurements in a magnetic field were performed with the sample in a horizontal field magnet cryostat of a Chalk River-Oxford Instruments design[54], which permits orientation of the field along any crystallographic direction. The maximum field is 2.95 T. The accuracy of the alignment of the direction between the field and the crystallographic axis was about 3°.

TABLE 2.1 Spectrometer configurations used in the experiments in this thesis. The third column is the horizontal collimation between reactor and monochromater, monochromater and sample, sample and analyzer, and analyzer and detector, respectively.

sample	instrument	collimation	monochromater	analyzer	cryostat
UNi_2Si_2 #1	N5	33′-42′-48′-56′	Si(111)	PG(002)	displex
#2	N5	33′-33′-36′-56′	Si(111)	Si(111)	
#1	L3	33′-33′-36′-56′	Si(111)	Si(111)	horizontal
Er	N5	33′-19′-24′-56′	Si(111)	Si(111)	field magnet

CHAPTER 3: THE EXPERIMENTAL RESULTS AND DATA ANALYSIS FOR UNi_2Si_2

3.1 Introduction

The first neutron diffraction study of the magnetic ordering of UNi_2Si_2 on a polycrystalline sample was performed by Chelmicki et al[26]. The experiment revealed a magnetic phase transition from a longitudinal spin-density wave type structure to a collinear simple antiferromagnetic type at around 53K and a Neel temperature at 103K. Contrary to this result, magnetization measurements by Buschow and DeMooij[23] show ferromagnetic ordering below 98K and no phase transition at 53K.

A series of measurements on a single crystal sample grown in the same laboratory as our crystals has been done recently by Ning et al[55,56] to study magnetic and transport properties of UNi_2Si_2 using different techniques, such as thermoelectric power,low temperature specific heat, electric resistivity, Hall effect and DC magnetic susceptibility. The data show that γ=22 mJ $mol^{-1}K^{-1}$ from the specific heat measurement. This indicates a small mass enhancement in the system. Anomalies occur at 53, 103 and 123K along the c axis of the crystal in all measurements, but perpendicular to the c axis only an anomaly around 94K in the thermoelectric power

measurement and a weak feature at 103K in the resistivity measurement is seen. The ferromagnetic moment is $0.62\mu_B$ at 4.2K. However, the ac susceptibility measurement on powder samples by Torikachvili et al[57] shows anomalies at 53K and 97K.

In this thesis the results on single crystal samples by neutron diffraction will be presented. The measurements were performed on two single crystals grown by a modified triple-arc Czochralski method. Sample #1 is 15 mm long with a diameter of 7 mm; sample #2 is 40 mm long with a diameter of 6 mm. Both samples showed sharp single crystal peaks with some minor asymmetric structure in the wings of the Bragg peaks. Sample #1 was in fact found to consist of two large single crystals widely separated in orientation. The measurements were made on sample #2 and one of the two crystals in sample #1. Both samples were aligned with the (h0ℓ) plane horizontal. The Bragg reflections of the nuclear unit cell are of the form h+k+ℓ=2n where h, k, ℓ and n are integers. The measurements confirm that the nuclear structure is a $ThCr_2Si_2$ structure and does not change from 11K to room temperature. The lattice parameters are a=3.958Å and c=9.514Å, and a=3.952Å and c=9.514Å at 11K for samples #1 and #2, respectively.

3.2 Magnetic Structure

A series of scans were taken along different directions in reciprocal space at fixed temperatures. The

diffraction pattern for four such scans from sample #1 along the [10ℓ] direction is shown in figure 3.1. Just the weak nuclear peak (1,0,1) is seen at 148K in the paramagnetic phase, but there are extra peaks in the pattern at 110, 79 and 11K. These are the magnetic Bragg peaks, and their different nature at the three temperatures indicates the presence of three distinct magnetic phases. As will be shown later, these phases are stable between 124 and 103K, 103 and 53K, and below 53K. They will be called the high-, intermediate-, and low-temperature phases.

It is apparent from close inspection of figure 3.1 that the Bragg peaks of sample #1 is asymmetric; each Bragg peak has some minor structure on its left hand side. The shape and width of all the magnetic Bragg peaks is the same as that of the nuclear peaks, indicating that in every case the magnetic peaks are sharp to within the experimental resolution and that the asymmetry is due to asymmetric crystal mosaic structure.

3.2.1 High-temperature phase

A survey of the (h0ℓ) plane indicates that this phase contains magnetic Bragg peaks of type (h,0,$\ell \pm q_z$) with h+ℓ=2n and h$\neq$0. We have observed all of the ten Bragg peaks of this type nearest to the origin, and these account for all the differences between the diffraction pattern at 110K and that at 148K. Least-squares fitting to the position of these

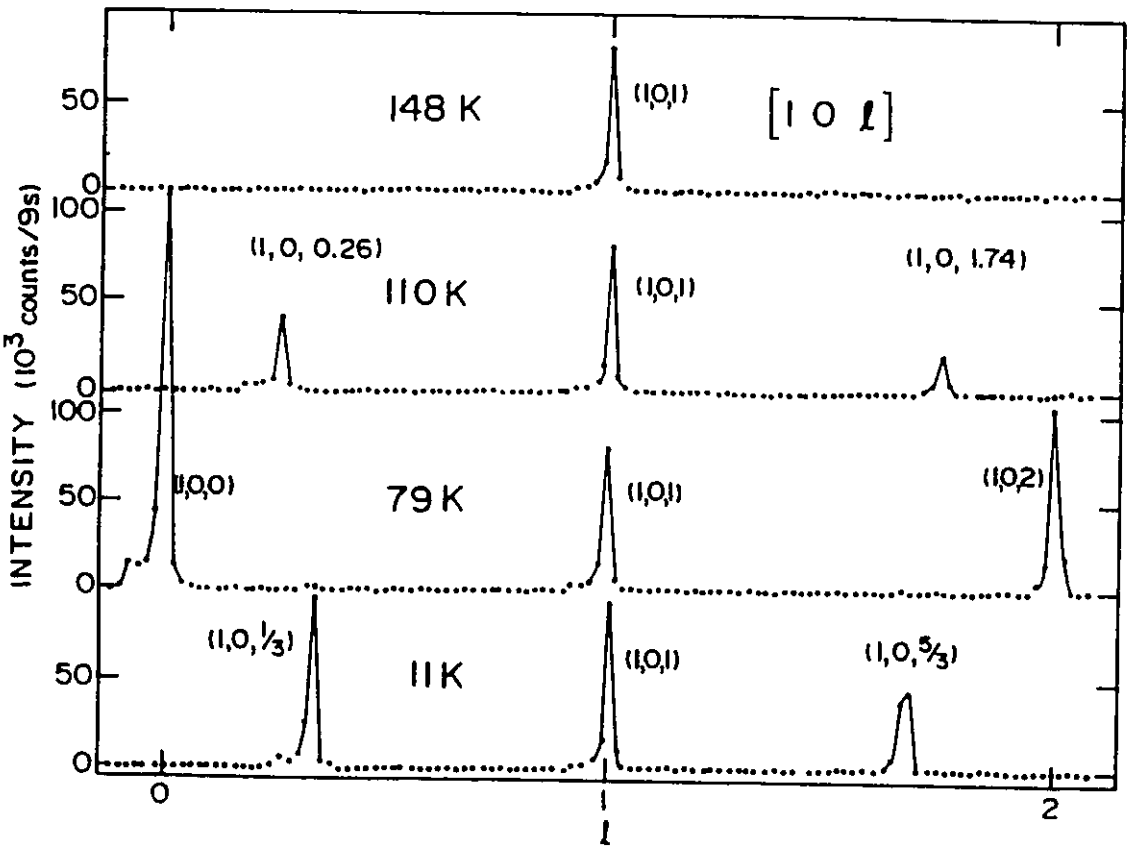

Figure 3.1 Diffraction pattern from UNi_2Si_2 along the [10ℓ] direction at 148, 110, 79, and 11K.

peaks gives q_z=0.745±0.002 at 110K.

A diffraction pattern of this type corresponds to a spin-density wave with wave vector $\mathbf{q}=(0,0,q_z)$. The restriction $h\neq 0$ indicates that the moments are aligned along the c axis so that the spin-density wave is longitudinal. As the other experiments on UT_2Si_2 compounds have already suggested, we will make the assumption that only the uranium atoms carry magnetic moment in our description of the spin-density wave. The diffraction patterns correspond to the spatial symmetry of the uranium sites. There is nothing in our data that requires the presence of a nickel moment for its interpretation. However, the measurements are rather insensitive to the presence of small moments (of order $0.1\mu_B$) and we cannot exclude the existence of such an amount of moment on the nickel sites.

A notable feature of the data is the absence of any reflections corresponding to harmonics of $\mathbf{q}$. This shows that the spin-density wave is quite sinusoidal, though for the commensurate wave with q=3/4 it is possible by adjusting the phase angle in eqn (1.2) to produce a squared-up structure with the succession of ferromagnetic layers coming in pairs of up and down sheets. The physical nature of the longitudinal spin-density wave is shown in figure 3.2.

Given this caveat, the magnetic moment has been calculated according to eqn (1.2) with $\hat{\mathbf{u}}=\hat{\mathbf{z}}$ and φ=0.

Table 3.1 lists the integrated intensities of the

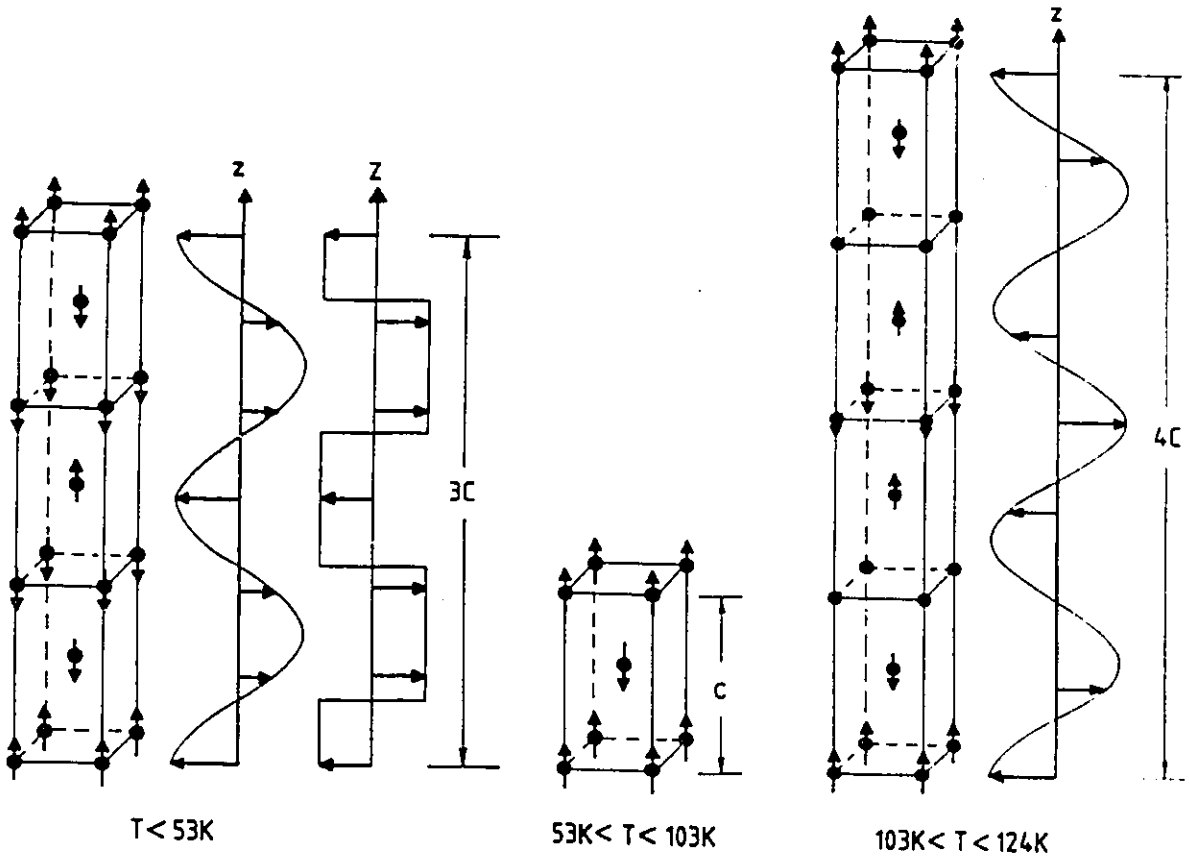

Figure 3.2 Magnetic structure in the three ordered phases. Two possible structures with $q=2/3c^*$ are shown for the low-temperature phase, on the left a longitudinal spin-density wave (LSDW), and on the right a square-wave. The intermediate-temperature phase is a simple body-centred tetragonal antiferromagnet and the high-temperature phase is a incommensurate LSDW with maximum $q\approx 3/4c^*$.

magnetic Bragg peaks observed and calculated for this phase. Least-squares fitting of these intensities to moments with form factors taken from Freeman et al [58], gives the maximum moment A in eqn (1.2) to be $A=(1.6\pm0.3)\mu_B$ with an R value of 3.4 %.

The experimental data indicate that the spin-density wave is incommensurate, with q_z slightly less than 3/4. In fact there is a temperature dependence to q_z which is shown in figure 3.3. The wave vector q_z has a maximum close to the commensurate value of three quarters at a temperature of 107K. This is about the temperature where the intensity of the Bragg peaks in this phase is a maximum. At higher and lower temperatures, q_z moves to values far from commensurability. Moreover, this temperature variation is seemingly continuous with no evidence of step-like behaviour corresponding to lock-in at various commensurate values.

3.2.2 Intermediate-temperature phase

In this phase magnetic reflections are observed with indices such that $h+k+\ell=2n+1$.

There are no magnetic reflections with h=k=0. This pattern indicates a simple body-centred tetragonal antiferromagnet with the moments aligned along the c axis. The result of a least-squares fitting to the data at 79K is given in Table 3.1. The moment so obtained is $(1.8\pm0.3)\mu_B$.

At 98K, a series of scans were taken along different

TABLE 3.1. Comparison of observed and calculated magnetic intensities for UNi_2Si_2 at 11, 79 and 110K.

			11 K			79 K		110 K	
h	k	ℓ	obs.	cal. LSDW	cal. square	obs.	cal	obs.	cal.
1	0	0.000				3810	5088		
1	0	0.255						796	1085
1	0	0.333	1745	2463	2282				
1	0	1.667	1760	1571	1456				
1	0	0.745						694	658
1	0	2.000				2985	2682		
1	0	2.255						586	507
1	0	2.333	1488	1110	1028				
1	0	3.667	595	516	477				
1	0	3.745						291	214
1	0	4.000				915	855		
1	0	4.255						145	159
1	0	4.333	336	347	321				
2	0	0.667	2135	1488	1379				
2	0	0.745						807	644
2	0	1.000				3541	2891		
2	0	1.255						736	600
2	0	1.333	1833	1356	1256				
2	0	2.667	1087	959	889				
2	0	2.745						414	407
2	0	3.000				2403	1727		
2	0	3.255						345	340
2	0	3.333	690	756	700				
2	0	4.667	433	425	393				
2	0	4.745						163	178
R(%)				4.8	9.1		5.9		3.4
moment	(μ_B)								
	A		2.7 ± 0.3			1.8	±0.3	1.6	± 0.3
	m_z		1.0 ± 0.3						
	$\lvert m_z \rvert$				2.2±0.3				

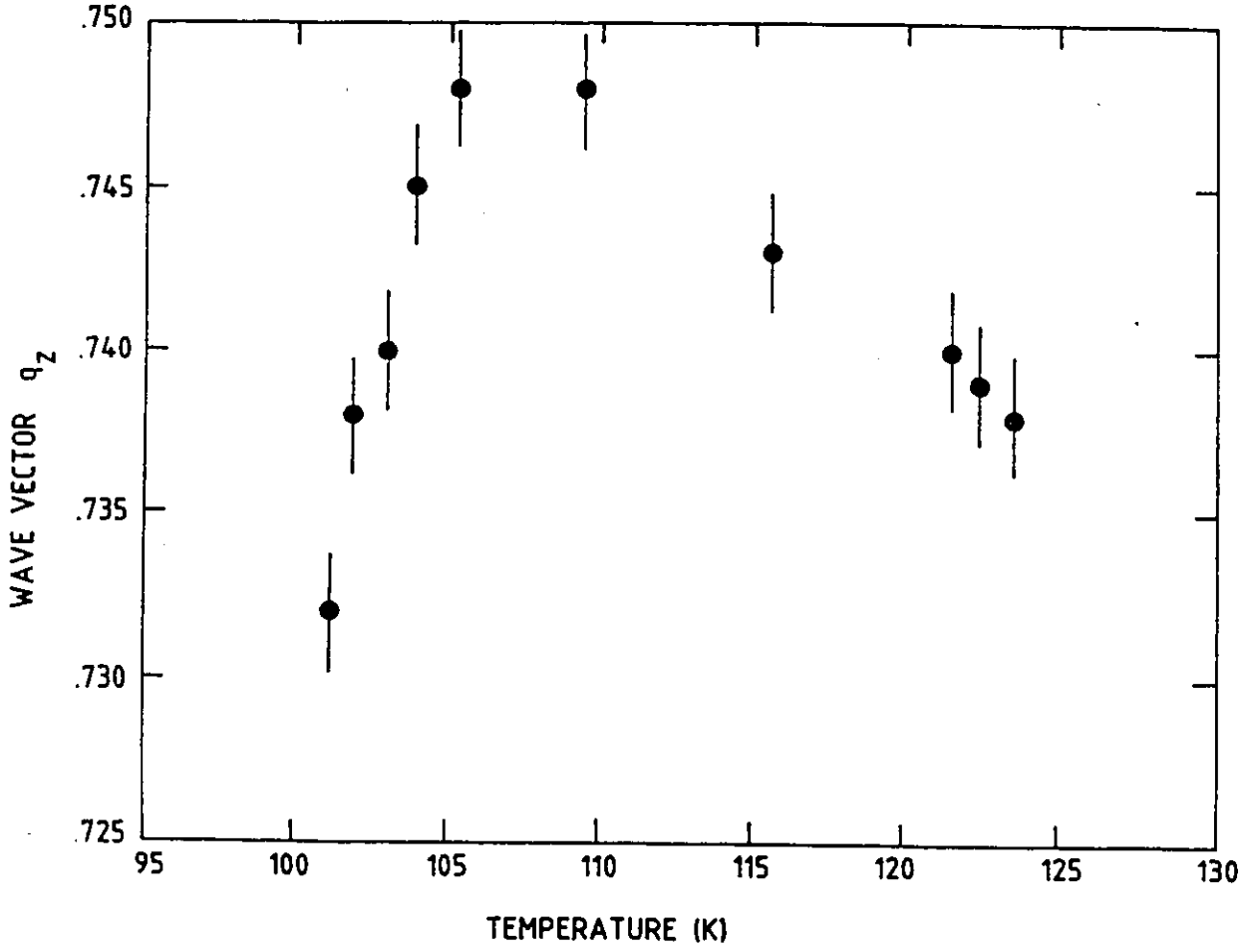

Figure 3.3 Variation of the incommensurate wave vector as a function of temperature in UNi_2Si_2.

directions in reciprocal space of the (h0ℓ) plane, where the thermoelectric power and magnetization measurements showed an anomaly. However, there was no new type of magnetic Bragg peaks in the scattering.

3.2.3 Low-temperature phase

The magnetic Bragg peaks in this phase are of the same type as those observed in the high-temperature phase but with q_z=0.667±0.002. The value of q_z was the same for the two samples and was temperature independent. Thus it is concluded that the low-temperature phase corresponds to a tripling of the unit cell along the c axis with q_z equal to two thirds. The absence of magnetic peaks of type (0,0,ℓ) again indicates that the moments are aligned along c. As was the case for the high-temperature phase, no peaks were observed corresponding to harmonics of q_z.

In addition, we searched for the ferromagnetic component of the moment suggested in Ref 23. Such components give rise to magnetic Bragg peaks at the same position as the nuclear Bragg peaks, that is at Bragg peaks with h+k+ℓ even. The Bragg peak with the smallest structure factor of any within our experiment range is (1,0,1); we observed it to be weaker than any other nuclear Bragg peaks by a factor of 5. Thus the sensitivity to a ferromagnetic component in UNi_2Si_2 is much higher at the (1,0,1) Bragg peak than at any other position. We observed that there was an increase of about 18%

in the intensity of the (1,0,1) Bragg peak relative to both higher-temperature phases (figure 3.4) for both samples. This building up of intensity at (1,0,1) indicates a ferromagnetic component in the magnetization that corresponds to a magnetic moment of $(1.0\pm0.3)\mu_B$. Such an amount of moment should be just observable on the $(0,0,\ell)$ nuclear peaks if the moment has an appreciable component in the xy plane. However, we did not observe any temperature change of the (0,0,2) Bragg peak within an error of $0.3\mu_B$ (figure 3.4). Therefore, we believe that the ferromagnetic moment is along **c**. In contrast to Ref 23, we observe no ferromagnetic moment in the temperature range $53<T<103$K, but only below 53K.

One possible interpretation of the data is that a commensurate longitudinal spin-density wave is combined with ferromagnetism. The model corresponds to a magnetic moment on the ℓth uranium atom given by

$$m_\ell = [A\cos(R_\ell q) + m_z]\hat{z} \qquad (3.1)$$

Least-squares fitting to this model gives $A=(2.7\pm0.3)\mu_B$ and $m_z=(1.0\pm0.3)\mu_B$ with an R value of 4.8%.

This represents the best fit to our data. However, it is possible to construct a squared-up structure with the magnitude of all the uranium moments the same if $A=4m_z$. This could be achieved by $A=2.96\mu_B$ and $m_z=0.74\mu_B$. The special values are within a standard error of our best fit values and give

R=9.1%. They are consistent with our experimental data and correspond to a magnetic cell with four moments of $2.22\mu_B$ along the +z direction and two moments of $2.22\mu_B$ along the -z direction. In this case, the net ferromagnetic component is naturally the consequence of the structure. The measured moment of $0.62\mu_B$ by magnetization measurements[56] supports this squared-up model.

The observed and calculated intensities at 11K are shown in Table 3.1. The possible structures in this phase are shown in figure 3.2.

3.3 Magnetic Phase Transitions

The temperature dependence of the characteristic Bragg reflections from sample #1 are shown in figure 3.4. We can see that the low-temperature phase represented by the (1,0,5/3) and (1,0,1) peaks is found below 53K, the intermediate-temperature phase represented by the (1,0,2) peak is found between 53 and 103K, and the high-temperature phase labelled by (1,0,1.74) exists between 103 and 124K. The phase transitions occur at 53±1, 103±1, and 124±1K.

The study of these phase transitions has been carried out with both samples.

Critical scattering is observed for Q=(1,0,ℓ) around ℓ=0.256 and (h,0,0.256) around h=1 with sample #2 above 124K, as the system enters the paramagnetic phase from the incommen-

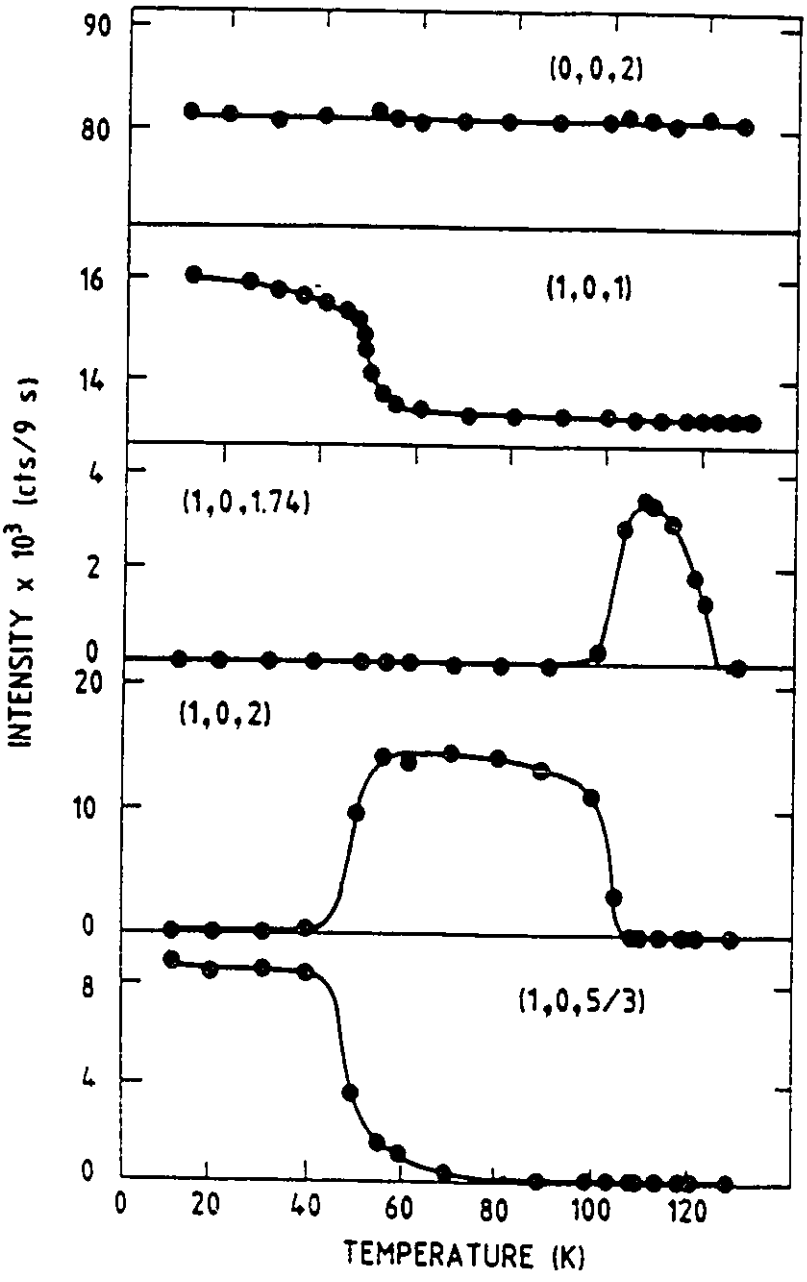

Figure 3.4 Temperature dependence of the intensity of the (1,0,5/3), (1,0,2), and (1,0,1.74) magnetic Bragg peaks and of the (0,0,2) and (1,0,1) nuclear Bragg peaks. There are phase transitions at 53, 103 and 124K.

-surate phase. Figure 3.5(a) and 3.5(b) shows the evolution of the critical scattering as a function of temperature. The resolution is 0.009±0.001 along $\mathbf{a}^*$ and 0.042±0.002 along $\mathbf{c}^*$, from which the variation of the intrinsic width of the critical scattering may be determined.

The width of peaks in scans along $\mathbf{c}^*$ is about twice as large along $\mathbf{a}^*$ in reduced reciprocal lattice units, as shown in figure 3.5. However, in real space, the correlation length ξ (which is represented by the reciprocal of the width of peak) is essentially the same, $\xi_c/\xi_a=0.94\pm0.10$, in the two directions because the lattice parameter c is about twice a. Thus the critical region is isotropic. The correlation length ξ is 10.08Å at 123.7K and 19.31Å at 124.7K along **c**. The critical scattering is centred at all temperatures about the position of the incommensurate magnetic Bragg peak at T_N, that is about Q=(1.000,0,0.265).

The critical temperature T_N is estimated by extrapolating the integrated intensity of the (1,0,0.256) magnetic peak as a function of temperature in the critical regime (figure 6(a)). Figure 6(b) shows a log-log plot of the integrated intensity against reduced temperature. The straight-line nature of the plot indicates that the intensity varies as a power law in reduced temperature, that is as $(T_N-T)^{2\beta}$. The value of β is fitted to be 0.35±0.03, which indicated that UNi_2Si_2 is not a mean field system, but instead is similar

in behaviour to a three dimensional Ising or xy system.

The phase transition at 103K, between the incommensurate and antiferromagnetic phases, behaves very differently from that at 124K. The temperature region of phase transition is about 4K wide, which is rather narrow. A rapid change of the order parameters, as represented by the intensity of (1,0,2) and (1,0,1.74) magnetic peaks, is observed (figure 3.4) at the phase transition. The width of those peaks remains resolution limited, and there is no temperature dependence of the observed width of the Bragg peaks to within an error of 0.002. The incommensurate wave vector q_z decreases continuously when the temperature decreases (figure 3.3), but suddenly jumps to q_z=1 when the antiferromagnetic phase is entered. No obvious hysteresis was observed. From the above evidence we conclude that the phase transition is first order.

For the lowest-temperature phase transition, hysteresis was observed on the (1,0,1/3),(1,0,0) and (1,0,1) reflections with sample #2. Figure 3.7 shows that hysteresis of the (1,0,0) reflection with a 4K spread between increasing and decreasing temperatures. The full phase transition region is about 20K wide. This is much broader than the transition at 103K. Although the integrated intensity changes relatively slowly, it does not obey a power law. The position and width

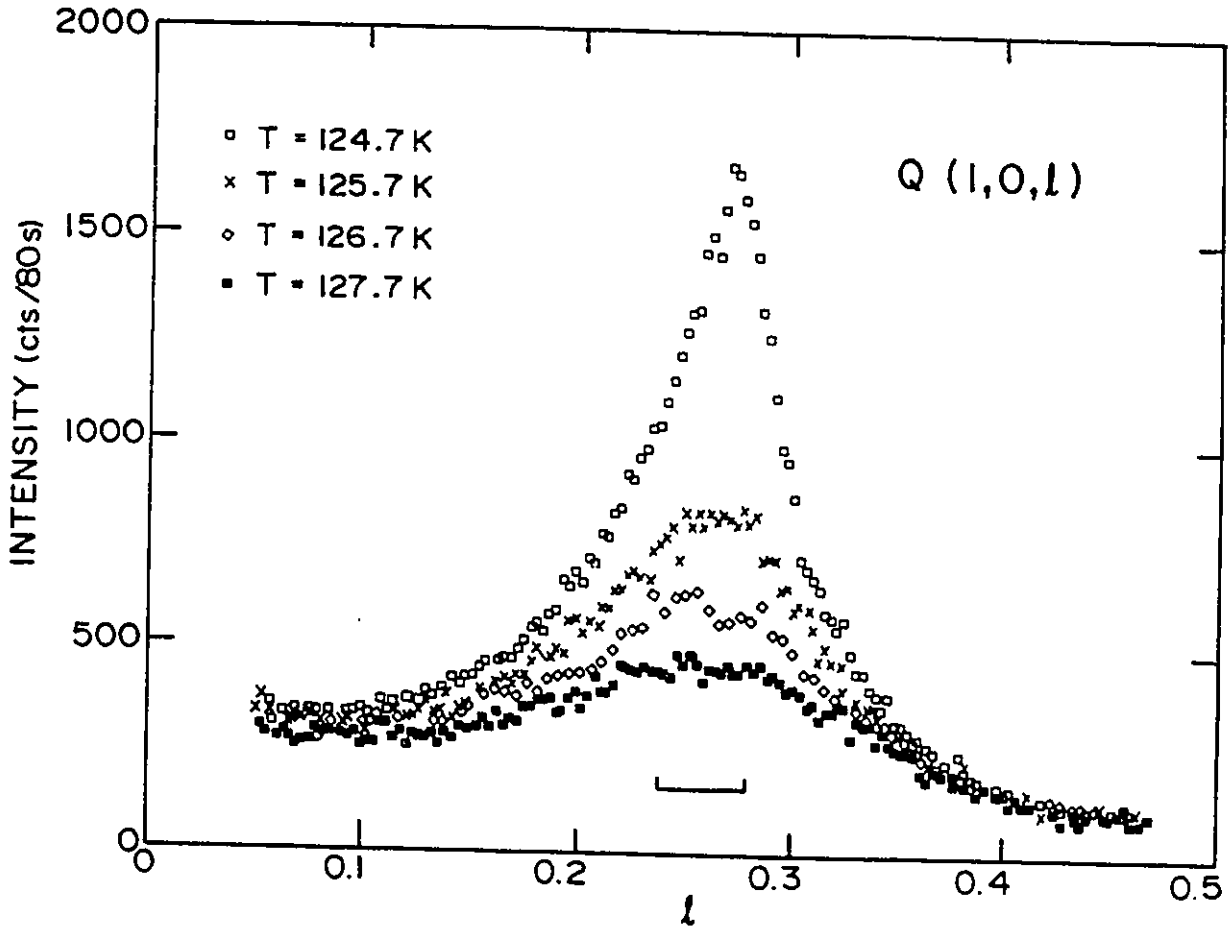

Figure 3.5(a) Critical scattering along the $(1,0,\ell)$ direction at a series of temperatures just above the critical temperature. The resolution width is shown by the horizontal bar.

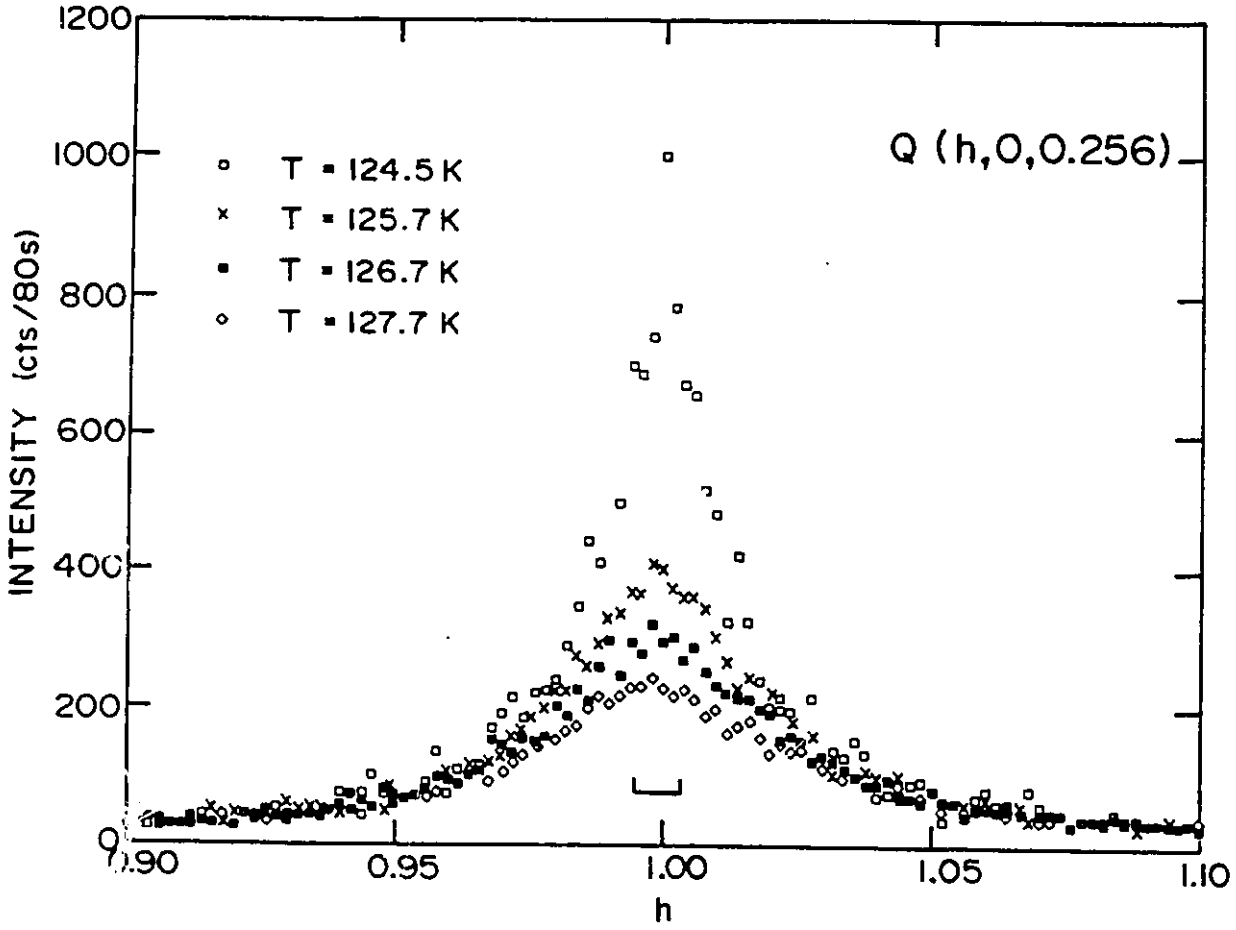

Figure 3.5(b) Critical scattering along the (h,0,0.256) direction at a series of temperatures just above the critical temperature. The resolution width is shown by the horizontal bar.

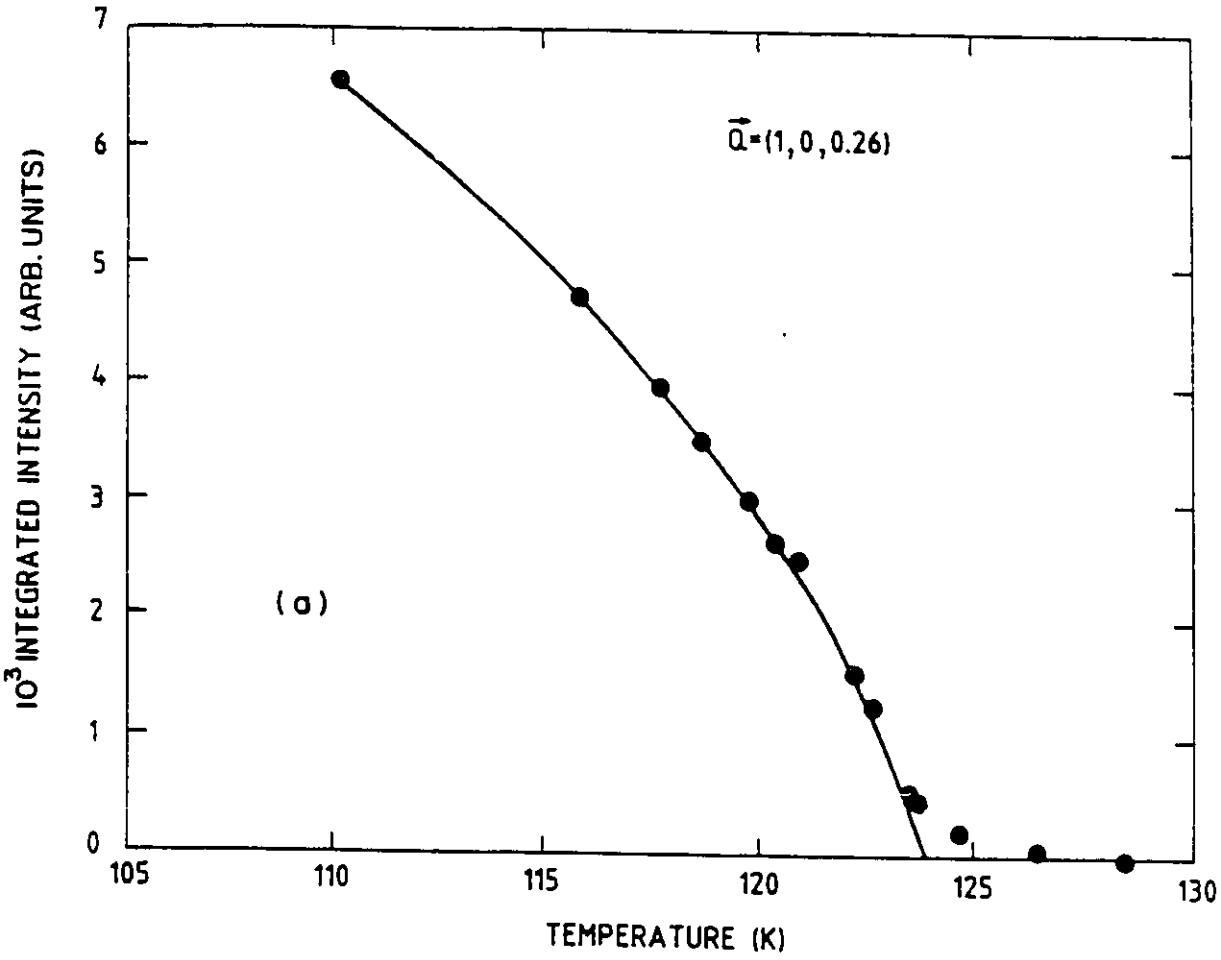

Figure 3.6(a) Temperature dependence of the integrated intensity of the (1,0,0.256) magnetic Bragg peak in the critical regime below 124K.

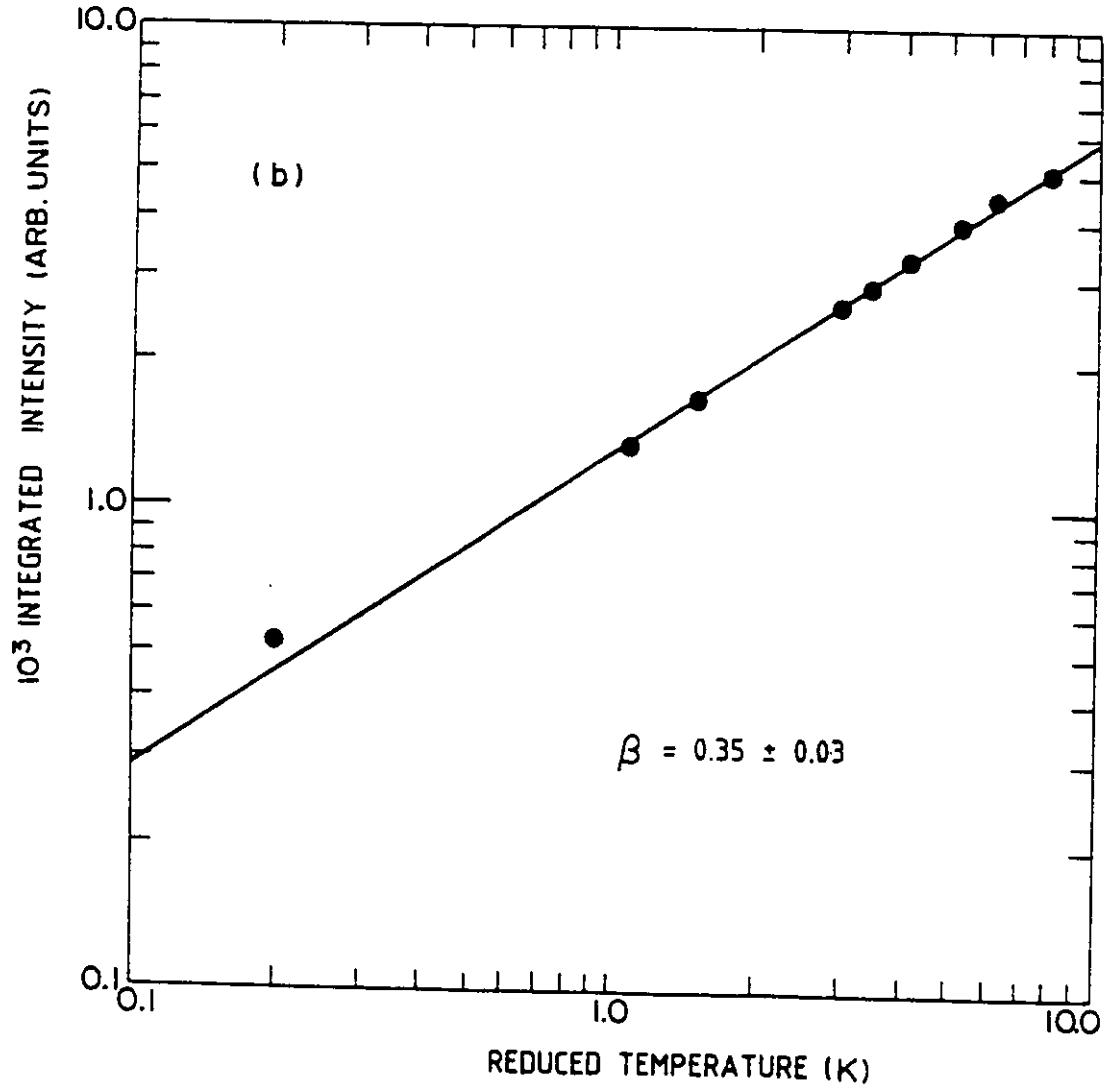

Figure 3.6(b) Log-log plot of integrated intensity vs reduced temperature. The slcp gives a critical exponent β of 0.35±0.03.

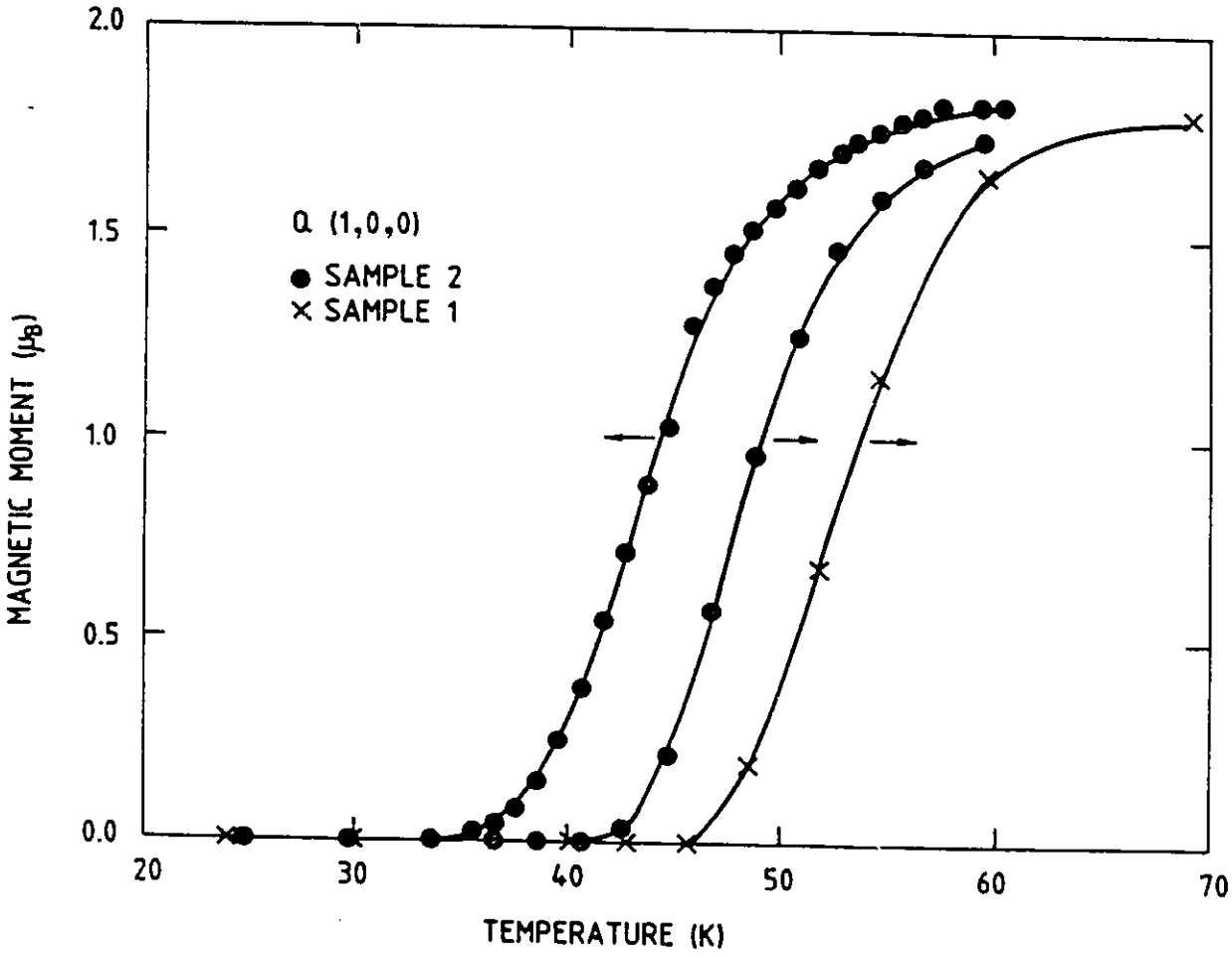

Figure 3.7 Hysteresis of the (1,0,0) magnetic Bragg peak with sample #2. The plot also shows that sample #1 and #2 give different phase transition temperatures. The arrows indicate the direction of the temperature variation.

of the Bragg peaks are temperature independent. It is concluded that this phase transition is first order.

Figure 3.7 also shows the behaviour of sample #1 at the lowest-temperature phase transition. It is notable that the two samples show transitions of similar width, but that the phase transition temperature is different by 4K. We have not been able to identify any differences between the two samples that can be connected to the difference of transition temperature. A third crystal from the same source gives the same higher transition temperature that was observed for sample #1. This sample dependence of phase transition temperature was not shown at the other two phase transitions, and in no other respect was the neutron scattering different between the two samples.

3.4 Phase Diagram in an Applied Field

The sample #1 was aligned with the (h0ℓ) plane horizontal with an applied field along the c axis for the experiments.

3.4.1 The magnetic scattering at H=2.95T

Figure 3.8 shows the temperature dependence of the intensity of the (1,0,0.26), (1,0,0) and (1,0,1/3) magnetic reflections in a field of 2.95 T. Comparison with figure 3.4 reveals several features.

The (1,0,1/3) reflection shows a sharp peak at about

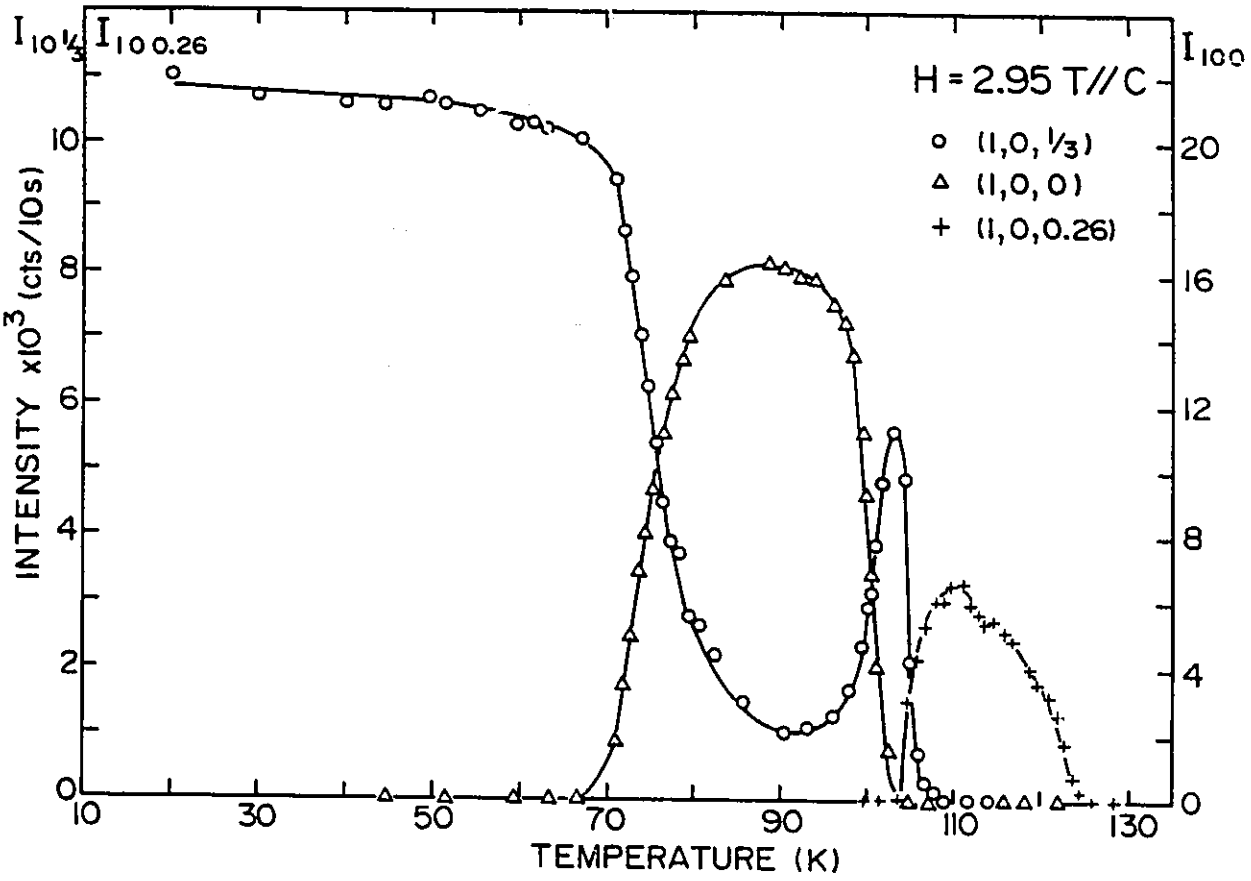

Figure 3.8 Temperature dependence of the intensity of the (1,0,1/3), (1,0,0), and (1,0,0.26) magnetic Bragg peaks in a field of 2.95T along the c axis.

103K. This indicates the presence of a new phase between the two phases represented by the (1,0,0) and (1,0,0.26) reflections. This phase is only 4.0±0.5K wide if we define the phase transition temperature as the temperature where the intensity is a half of its maximum value. The phase is centred at 102.3±0.5K, but the maximum intensity of the (1,0,1/3) reflection appears at 102.8±0.5K. As the temperature or field is varied, the peak of the (1,0,1/3) reflection remains at the same fixed location in reciprocal space, (1,0,0.333±0.001), indicating that the reflection is commensurate.

A survey of the (h0ℓ) plane at 102.8K was taken. We did not see any new type of diffraction pattern but just the pattern of the commensurate antiferromagnetic peaks as was found at low temperature in zero field. In addition, no reflections corresponding to harmonics of **q** were observed. Hence we conclude the new phase created by the field is the same longitudinal spin-density wave (LSDW) as is found at low temperatures, except that the ferromagnetic component is not present. The maximum sinusoidal moment given by a least-squares fitting to the data is 1.9±0.3μ_B in this temperature region.

Another feature is the change of phase transition temperature with field. We define the first order phase transition temperature as the average temperature where the intensity of the Bragg reflections is a half of its maximum

value. The low temperature transition moves from 53±1K in zero field to 75.2±1K in 2.95T. The upper boundary of the simple antiferromagnetic phase moves from 103.5±1K in zero field to 100.4±1K in a field of 2.95T. This leads to a narrower temperature region for the simple antiferromagnetic phase and a broader one for the low-temperature phase. The phase boundaries of the incommensurate LSDW are almost independent of field. No hysteresis of temperature or field was observed in the boundaries of the new LSDW phase.

The maximum magnetic component (A in eqn (2.2)) determined from the intensity of the magnetic reflections shown in figure 3.8 are $3.0\pm0.3\mu_B$, $1.8\pm0.3\mu_B$, $2.0\pm0.3\mu_B$ and $1.6\pm0.3\mu_B$ at the low temperature LSDW, the simple antiferromagnetism, the high temperature LSDW and the incommensurate LSDW phases respectively. All the magnetic Bragg peaks measured in this work remain sharp and resolution limited at all points in the ordered phases.

3.4.2 The field dependence of the magnetic structures

A series of scans along the [10ℓ] direction with different magnetic fields was taken in the temperature range from 10K to 130K. No new phases beyond those already described were observed.

Figure 3.9 shows the evolution of the commensurate (1,0,1/3) reflection with field at temperatures between 93K and 110K. As the field decreases from 2.95T the intensity of

the scattering from the phase decreases and it disappears below a field of 1.5T. The centre position of the phase stays at 102.3±0.5K and the temperature dependence of the scattering keeps the same shape as the field is varied.

With the temperature fixed at 102.8K, the intensity of the (1,0,1/3) reflection was measured as a function of field. The result is shown in figure 3.10. At higher fields, the intensity varies linearly with field, and extrapolation of a least-squares fit to the data above 2.2T gives an onset field of 2.10±0.05T. The measurements indicate the existence of a triple point which connects the simple antiferromagnetic phase, the commensurate LSDW phase and the incommensurate LSDW phase at T=102.8±0.5K and H=2.10±0.05T.

In the incommensurate LSDW phase, the intensity of the scattering is similar at all fields, but the value of the incommensurate wave vector q_z is different in different fields and at different temperatures. Figure 3.11 shows the behaviour of the peak position of the incommensurate $(1,0,\ell)$ magnetic reflection as a function of applied field. The minimum, value of about 0.25 in zero field, disappears gradually as the field increases. At a field of 2.95T, ℓ decreases continuously as the temperature increases at lower temperatures but reaches a temperature independent value of 0.265 at higher temperatures. The experimental error in the determination of ℓ is 0.002. The effect of field on q_z is more pronounced in

the centre of the phase region than near the boundaries. Increasing the field always tends to move the value of q_z away from the commensurate value of 3/4.

3.4.3 The magnetic phase diagram

Figure 3.12 shows typical results for the low temperature phase transition at different fields through the temperature dependence of the intensity of the (1,0,0) reflection. The transition shows hysteresis effects, and we have taken all the data in figure 3.12 with rising temperature so that the measurements can all be placed on an equivalent footing. The phase transition temperature increases with field, but the width of the phase transition and the magnitude of the saturated intensity are field independent.

The phase transition at 103K in zero field did not show field dependence until 2 T. As the high temperature LSDW phase grows, the temperature at half intensity of the (1,0,0) reflection decreases, but that of the (1,0,0.26) reflection increases slightly. The 124K phase transition temperature showed the field independence.

We can summarize our data by drawing a magnetic phase diagram for UNi_2Si_2. This is shown in figure 3.13, with the applied field along the c axis. The data predicts that the simple antiferromagnet will disappear in higher fields. This has been proven by the magnetization measurements, where McElfresh shows that the antiferromagnetism does not exist

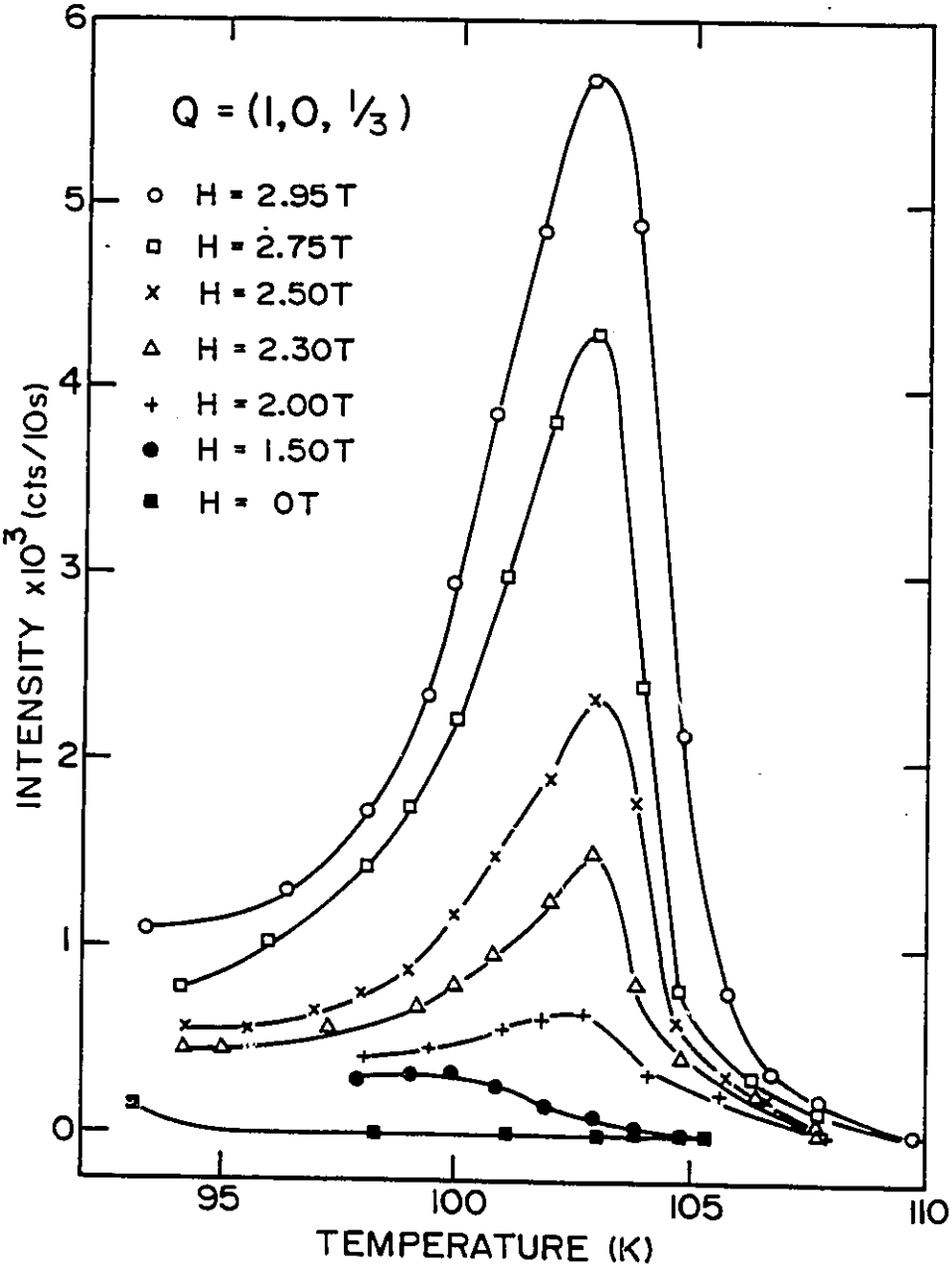

Figure 3.9 The intensity of the (1,0,1/3) magnetic Bragg peak as a function of temperature in different fields.

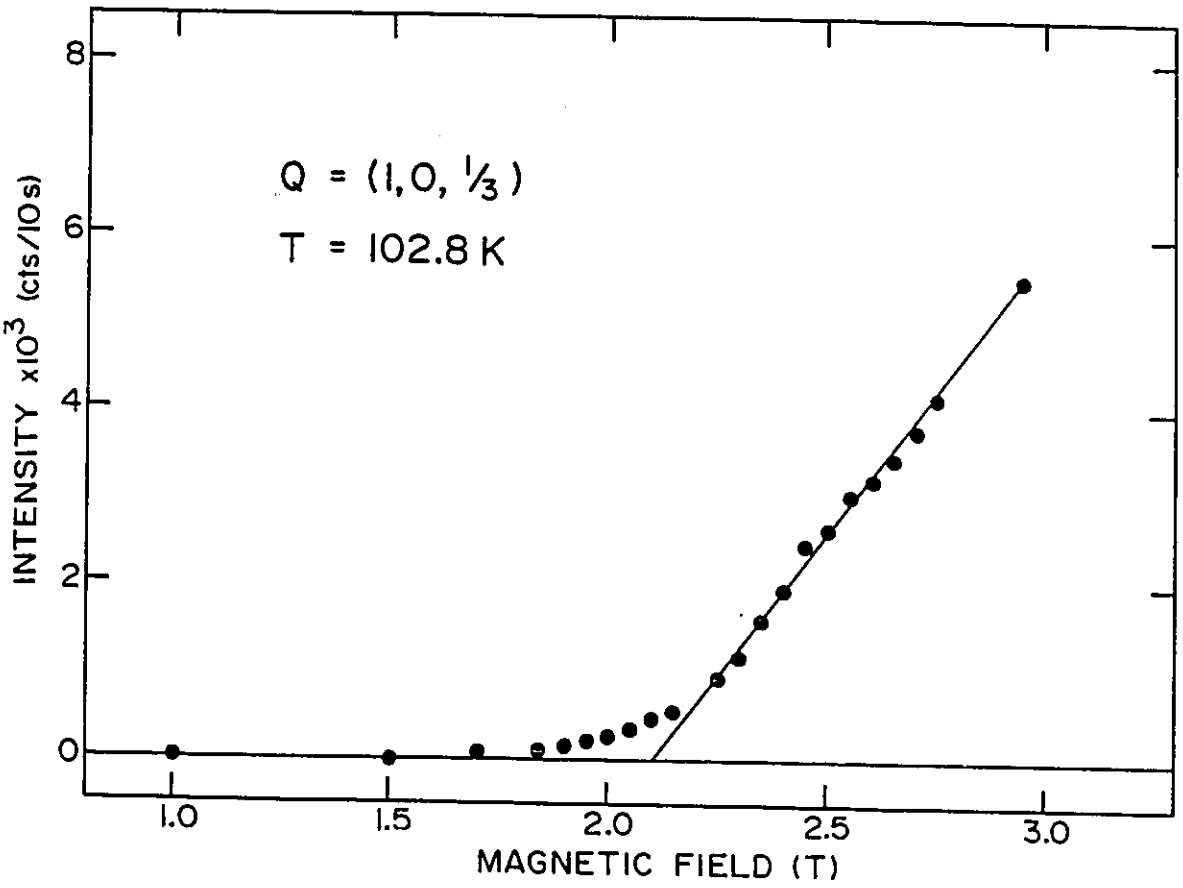

Figure 3.10 The intensity of the (1,0,1/3) magnetic Bragg peak as a function of applied field at a temperature of 102.8K.

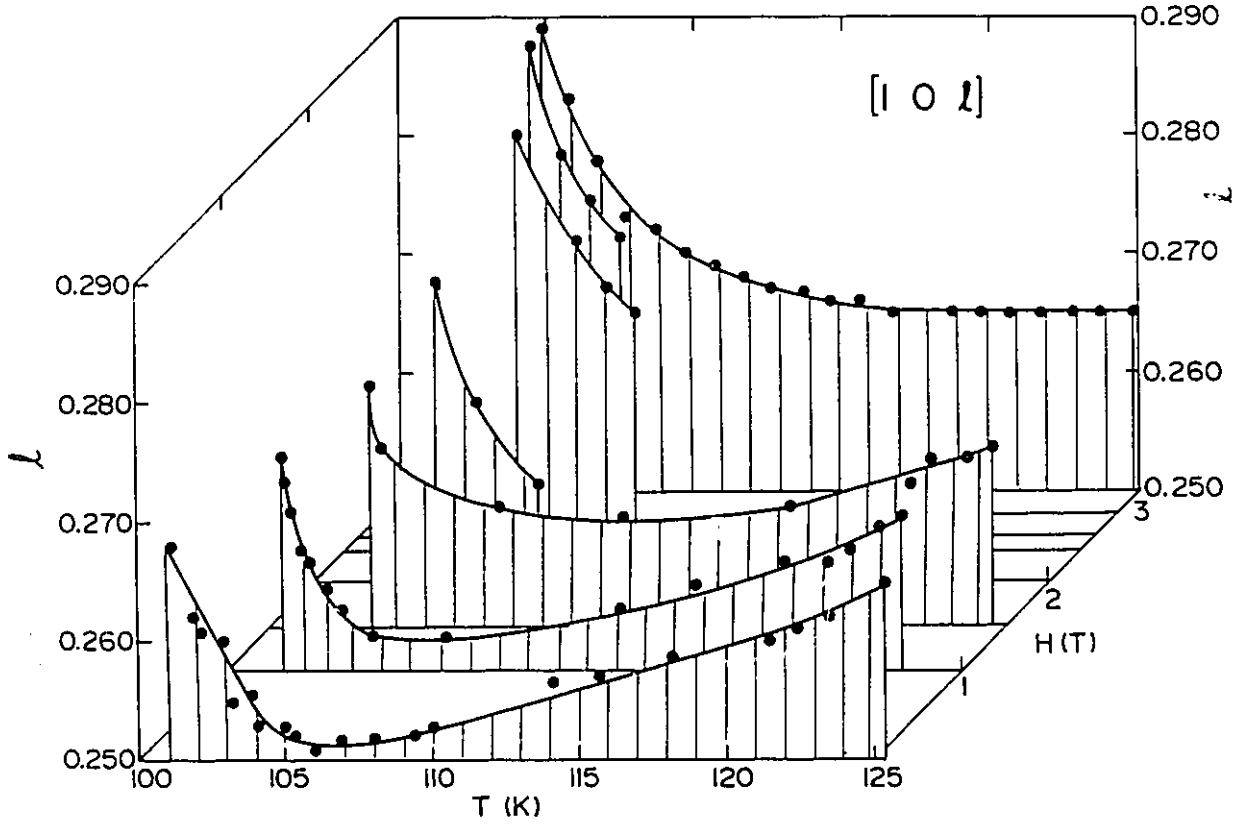

Figure 3.11 Temperature dependence of the position of the $(1,0,\ell)$ magnetic Bragg peak in different fields.

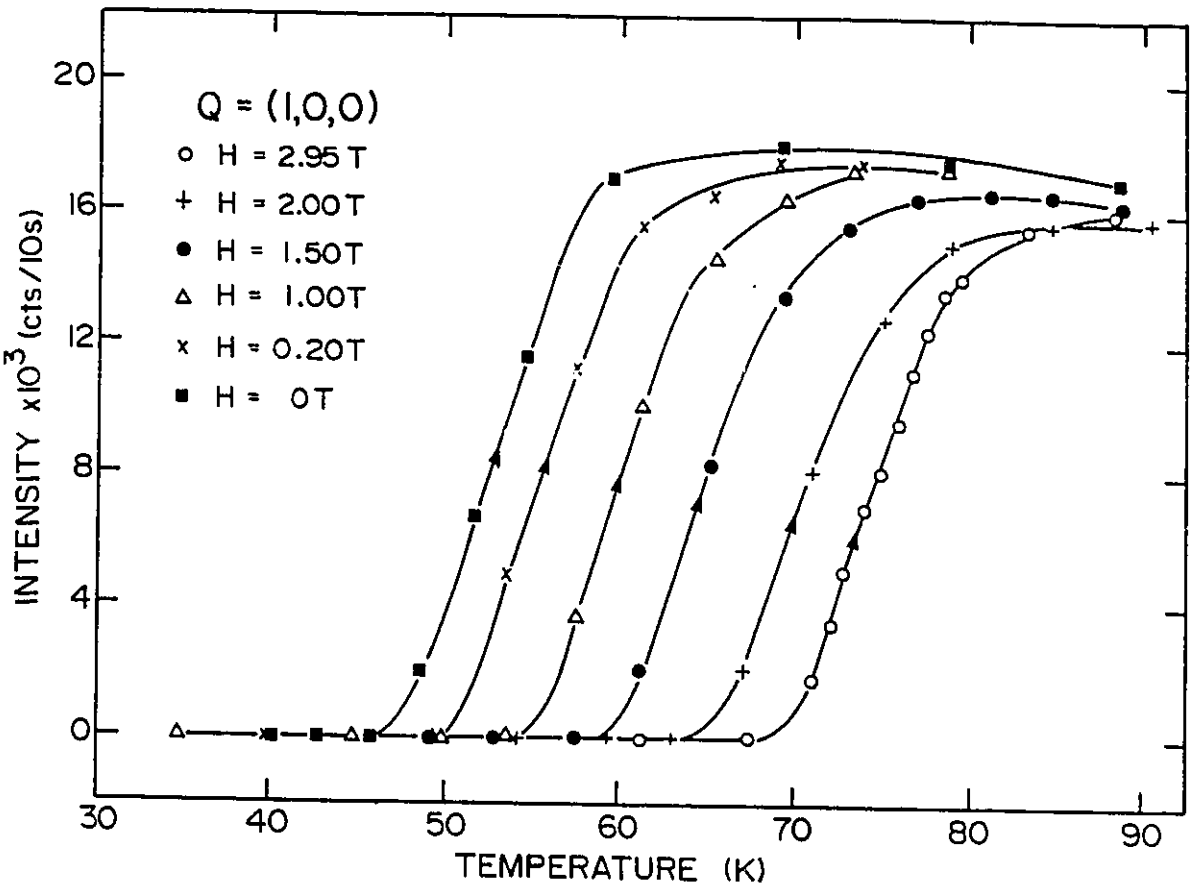

Figure 3.12 The intensity of the (1,0,0) magnetic Bragg peak as a function of increasing temperature in different fields.

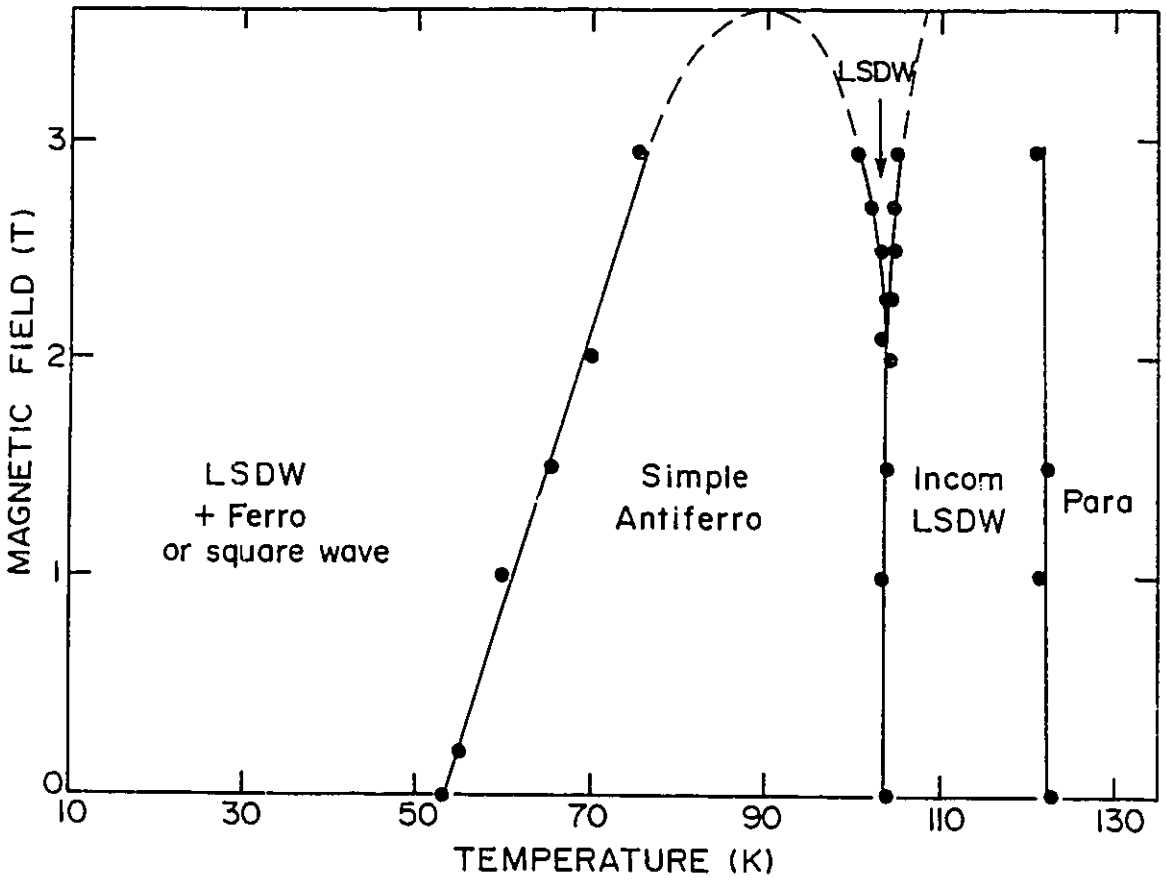

Figure 3.13 The magnetic phase diagram of UNi_2Si_2, with increasing temperature and applied field along the c axis. The solid lines are guides to the eyes. The dashed line is taken from the magnetization data.

above a field of 3.5T[3].

3.5 Discussion and conclusions

Our neutron-diffraction data of UNi_2Si_2 on single crystals in zero field agrees with the powder measurement by Chemicki et al[26] except that, in addition, we observe a third long-range magnetic ordered phase in the temperature region 103-124K. Some vestiges of the scattering from the incommensurate phase is apparent in Chemicki's published data. Our possession of single crystals has enabled us to make more detailed and more precise measurements.

The observation of oscillating moments with a net ferromagnetic component in the low-temperature phase was made in two different single crystals. This indicates that ferromagnetism is an intrinsic magnetic property of UNi_2Si_2 at lower temperatures, although the possibility of sample dependence of the value of ordered ferromagnetic moment exists since the moment in samples #1 and #2 was observed to be $(0.9\pm0.3)\mu_B$ and $(1.1\pm0.3)\mu_B$, respectively, and another sample from the same source as our samples showed a low temperature magnetization of $0.62\mu_B$[56]. We do not find ferromagnetism below 98K, as suggested in ref 23, but only below 53K.

The study on phase transitions shows that a conventional isotropic critical scattering centred on the wave vector **q** exists above 124K. The critical phase transition from

the incommensurate to the paramagnetic state has the critical exponent β=0.35±0.03. The other two phase transitions are both first order, but the low-temperature phase transition shows hysteresis and sample dependence.

When a magnetic field is applied along the c axis, there are no new phases induced. However, the simple antiferromagnetic phase is destabilised by the field and disappears above a field of 3.5T. There exists a reentrant point at 102.8K and 2.1T which connects the commensurate LSDW, simple antiferromagnetic, and incommensurate LSDW phases. The wave vector q decreases with increasing field in the incommensurate LSDW phase. There may exist a point in a higher field where the wave vector for the incommensurate and the commensurate LSDW phases become the same. This will happen if q_z is shifted by the field up to a value of 2/3.

An attempt has been made to explain the different kinds of magnetic ordering of UT_2Si_2 by using the isotropic RKKY model with a spherical Fermi surface[25-27]. However, the assumption of a spherical Fermi surface seems unrealistic, and it is not possible in this model to explain the existence of all three ordered structures at different temperatures. It is also possible to set up a model which gives a less localized character to the f electrons along the lines of the theory of spin-density waves[59]. This model explains the spin-density wave as arising from parallel areas of Fermi surface separated by

a wave vector **q**. There might be two such wave vectors corresponding to the commensurate structure, possibly arising from the large, and highly temperature dependent, anisotropy energy in uranium compounds.

We note that all the magnetic structures of UNi_2Si_2 exhibit ferromagnetic sheets with moments perpendicular to the sheets. Any model of the magnetic structure would need to incorporate this feature of planar ferromagnetic coupling. Except for the ferromagnetic ordering, the three phases order antiferromagnetically, with moments either modulating from sheets to sheets or coupling up and down simply. A possible theoretical framework to explain the UNi_2Si_2 data may be the ANNNI model since this model has Ising characteristics and can give rise to exotic structures of the type that we have observed. The spatially modulated phases, commensurate-commensurate phase transitions, and multiphase points in some rare-earth magnets like CeSb and USe-UAs have been described in terms of this model[39,51,60]. This model leads naturally to squared-up low-temperature structure and would accommodate the squared-up structure that we have described as a possibility for the low-temperature phase.

CHAPTER 4: THE EXPERIMENTAL RESULTS AND DATA ANALYSIS FOR ERBIUM

4.1 Introduction

The magnetic ordering of erbium has been studied using neutron and x-ray magnetic scattering over the decades. The detailed experimental study can be found in the references by Cable et al[61], Habenschus et al[62], Rhyne and Pickart[63], Atoji[64], and Gibbs et al[18].

In the absence of an applied field, there are three distinct magnetic ordered phases below the Neel temperature: the c-axis modulated (CAM) phase, the intermediate temperature phase, and the cone phase.

In the CAM phase, (52-84K), the moments are modulated sinusoidally along the c axis with wave vector $\mathbf{q}\approx 0.29\mathbf{c}^*$.

As the temperature decreases, the harmonics of $\mathbf{q}$ observed in the scattering indicates that the modulation of the z component of the moments becomes increasingly squared-up. The appearance of the harmonics is not connected in any way with the magnetic ordering of the basal plane moments. The wave vector $\mathbf{q}$ decreases monotonically from about $0.29\mathbf{c}^*$ to $0.25\mathbf{c}^*$.

There is a sequence of commensurate and incommensurate phase transitions in the intermediate

temperature phase (18-52K). The wave vectors of the commensurate structures lock in to certain rational-fractional values which can be described by $\mathbf{q}=n(4n-1)^{-1}\mathbf{c}^*$ with $n=2,3,4,5,6,\infty$. The temperature ranges of the lock-ins are up to 5K wide. Between 18 and 25K, a squared-up commensurate structure with $\mathbf{q}=1/4\mathbf{c}^*$ is stable.

The xy components of the moments order below 52K with the same periodicity as the z component of the moments. However, how the xy components couple with the z component can not be experimentally determined since the neutron scattering cannot tell the phase. The hodograph of the moment is basically an ellipse in this phase, but Cable[61] argues that the major axis of ellipse tilts from the c axis and the xy components of the moments form a helix (tilted helix), and Jensen[65] argues that the axis of ellipse lies down on the easy axis so that the moments are confined in the ac plane (cycloidal structure).

In the cone phase (below 18K), the z component of the moments aligns ferromagnetically along the c axis and the xy components rotate uniformly with $\mathbf{q}=5/21\mathbf{c}^*$. The cone angle is about 30°.

Anomalies at three phase transitions are also observed in the resistivity[66], specific heat[67], thermal expansion[68] and other types of measurements. There are small variations in the phase transition temperatures and lock-ins reported in the

literature, indicating some sample dependence of these properties. Hysteresis effects are observed below about 52K.

The magnetization of single crystals of erbium has been measured by Green et al[66], Flippen[69], Rhyne et al[70], Feron et al[71], Gama and Foglio[72], Ali et al[73] and Anstrom et al[74]. In addition to three distinct phase transitions, anomalies in the intermediate temperature phase are observed to correspond to the commensurate lock-in structures[73,74]. The c axis is found to be the direction of easy magnetization. At low temperatures there is a ferromagnetic moment of 7.9 μ_B along the c axis. In zero field or with a field applied along c there is a first order phase transition for the z component of the moments directly from ferromagnetism to the periodic modulation. The critical field Hc increases with temperature and goes through a maximum of about 2.2T at around 65K. In the temperature range from about 20 to 55K, the relation of the critical field and temperature is linear, given by Hc=0.06(Tc-18) Tesla.

In this thesis neutron scattering studies of the structure of erbium in an applied magnetic field along the c axis will be presented.

The single crystal used was 2 mm thick, 6 mm wide and 30 mm long. The lattice parameters of the hexagonal close-packed structure were a=3.550Å and c=5.600Å at 4.2K. The sample was aligned with the (hhℓ) plane horizontal. Scans were taken by varying ℓ along the [11ℓ] and [00ℓ] directions

in reciprocal space. The $(1,1,\ell)$ peaks have a slightly larger width than the $(0,0,\ell)$ peaks.

The measurements were normally performed with increasing temperature. There were high torques on the sample from the magnetic field in some configurations and the horizontal alignment of the crystal was adjusted as necessary. The magnetic field in this work refer to the applied field. There is no demagnetization correction on the data.

The position and the integrated intensity of the Bragg reflections was determined by fitting data to a Gaussian line shape. The value of q for a magnetic peak was taken relative to the position of the nearest nuclear Bragg peak. For determinations of the magnetic structure factor the magnetic intensity was normalized to the intensity of the nearest nuclear peak. The calculations were made following the formalism in Chapter 2. The value of the magnetic form factor was taken from Stassis et al[75], and the nuclear scattering length of erbium was taken as 0.803×10^{-12} cm[76]. A correction of the integrated intensity for a triple-axis spectrometer in the elastic mode was made following Cowley and Bates (see Appendix), and a correction for the absorption effect was phenomenologically taken by fitting the data for the nuclear peaks to the calculated nuclear structure factor.

4.2 Lock-in Phase Transitions

Figure 4.1 summarizes the data for the temperature dependence of the wave vector **q** at different fields. For T>54K, the value of q was determined from the (1,1,q) peak since the moments in the basal plane were no longer ordered and the (0,0,ℓ) peaks were not present. For T<54K, an average of the peak positions of (0,0,2-q), (1,1,q) and (1,1,3q) was used, though in a field only the position of the (0,0,2-q) peak was measured systematically. The error is within ±0.002 r.l.u..

In zero field, q locks in to the rational fractions 5/21, 1/4 and 5/19 in the temperature range of 4.2-20K, 21-27K and 30-34K respectively. Although no other of the lock-ins suggested by the c-axis spin-slip model is seen, it is possible that lock-ins at q=4/15, 3/11 and 2/7 exist but with a narrower temperature range since the temperature step in our experiment was 1.5-2K at higher temperatures. The sample studied by the x-ray magnetic scattering[18] and magnetization[72] shows the lock-ins at 5/21, 1/4, 6/23, 5/19, 4/15, 3/11 and 2/7 at the temperature of below 18K, 18-23K, 23-26.5K, 29K, 31.5-34.5K, 41K and 48.5-51.6K respectively. Another sample used in early neutron scattering experiments [62] showed the lock-ins at 5/21, 1/4 and 4/15. The comparison shows a sample dependence of the lock-ins.

Figure 4.2(a) shows the measured lock-ins from the

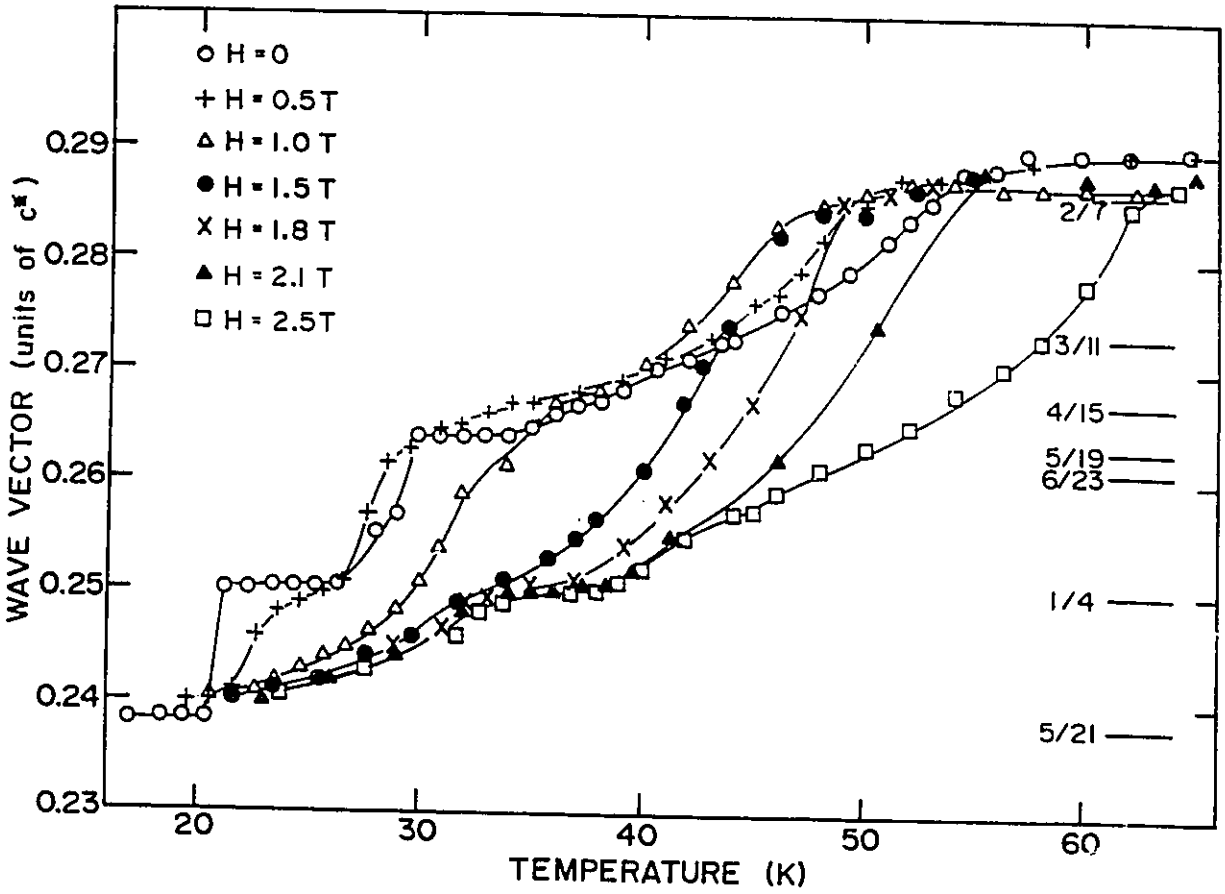

Figure 4.1 The magnitude of the wave vector q as a function of increasing temperature at different fields applied along the c axis. Lock-ins at 5/21, 1/4 and 5/19 in zero field, at 1/4 in a field of above 1.8T and at 2/7 in a field can be seen. The rational fractions on the right are the zero field lock-ins predicted by the c-axis spin-slip model.

(0,0,2-q), (1,1,q) and (1,1,3q) reflections in zero field in the temperature range from 10 to 40K. The data show that the lock-ins are independent of the reciprocal lattice vector **Q**, and therefore three dimensional. This has been suggested from recent magnetization and AC susceptibility experiments by two different groups[73,74]. Since the (0,0,2-q) reflection corresponds to xy components of the moments and the z component of the moments can be obtained by subtraction of the xy components from the (1,1,q) reflection, the evidence of the three dimensional lock-ins indicates that the spins in the basal plane and along the c axis are coupled. There seems to be a systematic difference of 0.5% between the values of q obtained from two reflections. The most accurate determination of q by Gibbs et al[18] suggests that the lock-in at around 25K, for instance, is exactly at one quarter, so it is likely that there is a small systematic error in our (0,0,2-q) data.

When a field is applied along the c axis, the lock-ins at 1/4 and 5/19 are destroyed. Figure 4.2(b) shows the evolution of **q** with field for temperatures corresponding to the centre and the boundaries of the $\mathbf{q}=1/4\mathbf{c}^*$ phase. The variation of **q** with field is reversible at 22K below a field of 0.7 T. Although the figure only shows the (0,0,2-q) reflection, the measured (1,1,q) and (1,1,3q) reflections in fields of 0.5T and 1.0T also indicate that lock-ins no longer exist for the z component of the moments.

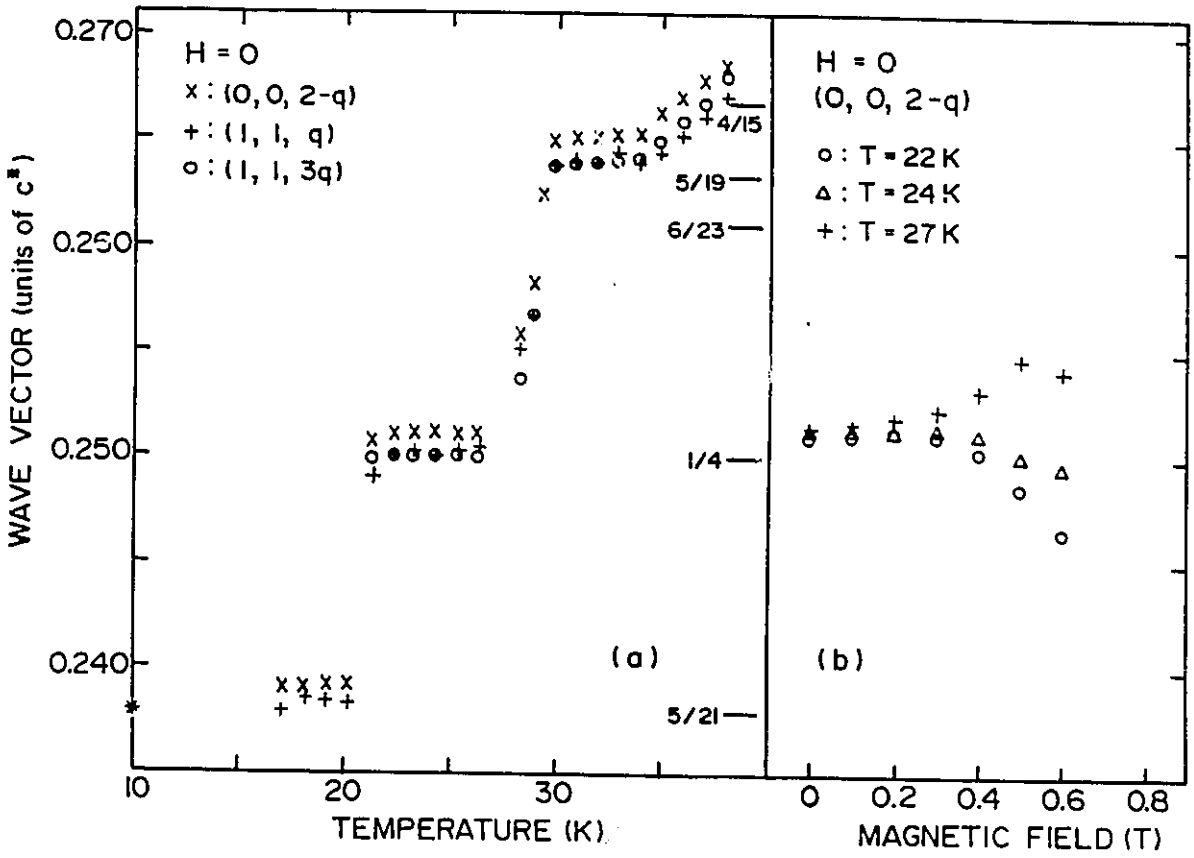

Figure 4.2 (a) Lock-ins in zero field along the [00ℓ] and [11ℓ] directions. (b) The wave vector q as a function of field near the $q=1/4c^*$ in the intermediate phase.

It is interesting to note that q=4/15 at about 38K is an inflection point which is not moved by the fields until 1 T. The inflection behaviour in zero field near q=4/15 was also observed by Habenschuss et al[62].

Another feature is that the field stabilises the lock-in at $\mathbf{q}=2/7\mathbf{c}^*$ at higher temperatures. Figure 4.3(a) shows two examples where the wave vector is obtained from the (0,0,2-q) reflection. The onset temperature and field of the lock-in in the intermediate phase can be described by $T_L=54.0-5.3H_L$ ($0<H_L<1.5T$) and $T_L=21.0+16.7H_L$ ($1.5T<H_L<2.2T$). The measured (1,1,q) reflections also suggest that the lock-in at q=2/7 persists in the CAM phase at fields of 1.0T and above. However, not enough data were taken in this phase to determine the full extent of the lock-in at 2/7.

The cone phase is stabilised by the field. The temperature range of the lock-in with $\mathbf{q}=5/21\mathbf{c}^*$ is almost field independent. Above 21K the magnitude of **q** is usually reduced as the field is increased at fixed temperature. For fields above 1.8T and temperatures between 34 and 39K, we observed a new lock-in cone structure with $\mathbf{q}=1/4\mathbf{c}^*$.

Figure 4.4 shows plots for the lattice constant c obtained from the position of the (0,0,2) nuclear peak. The change in value of c from about 5.60Å to 5.58Å corresponds to the transition from the cone phase to the intermediate phase. It is clear that the major determinator of the value of c is

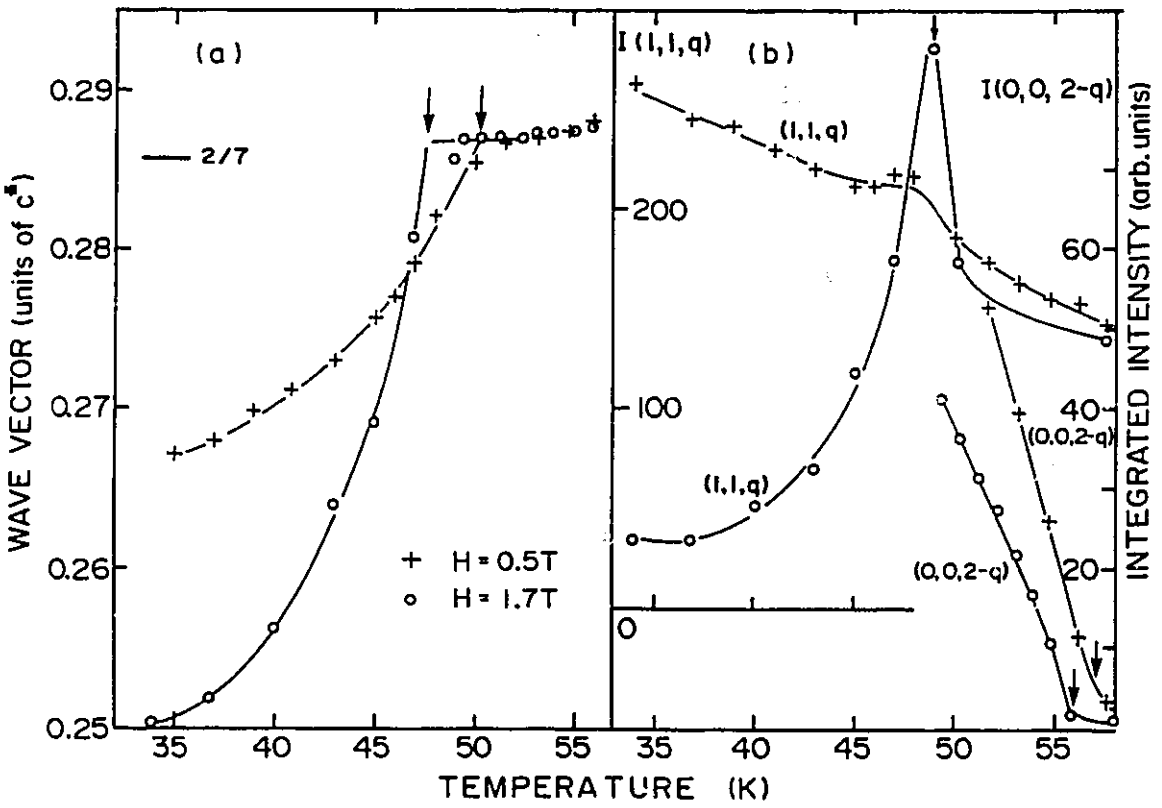

Figure 4.3 (a) The lock-in at 2/7 from the (0,0,2-q) magnetic Bragg peak in fields of 0.5T and 1.7T. (b) Phase transition between the intermediate and the CAM phase reflected by the (0,0,2-q) peak and between the cone and the intermediate phase reflected by the (1,1,q) peak in fields of 0.5T and 1.7T. The arrow marks the phase transition temperature.

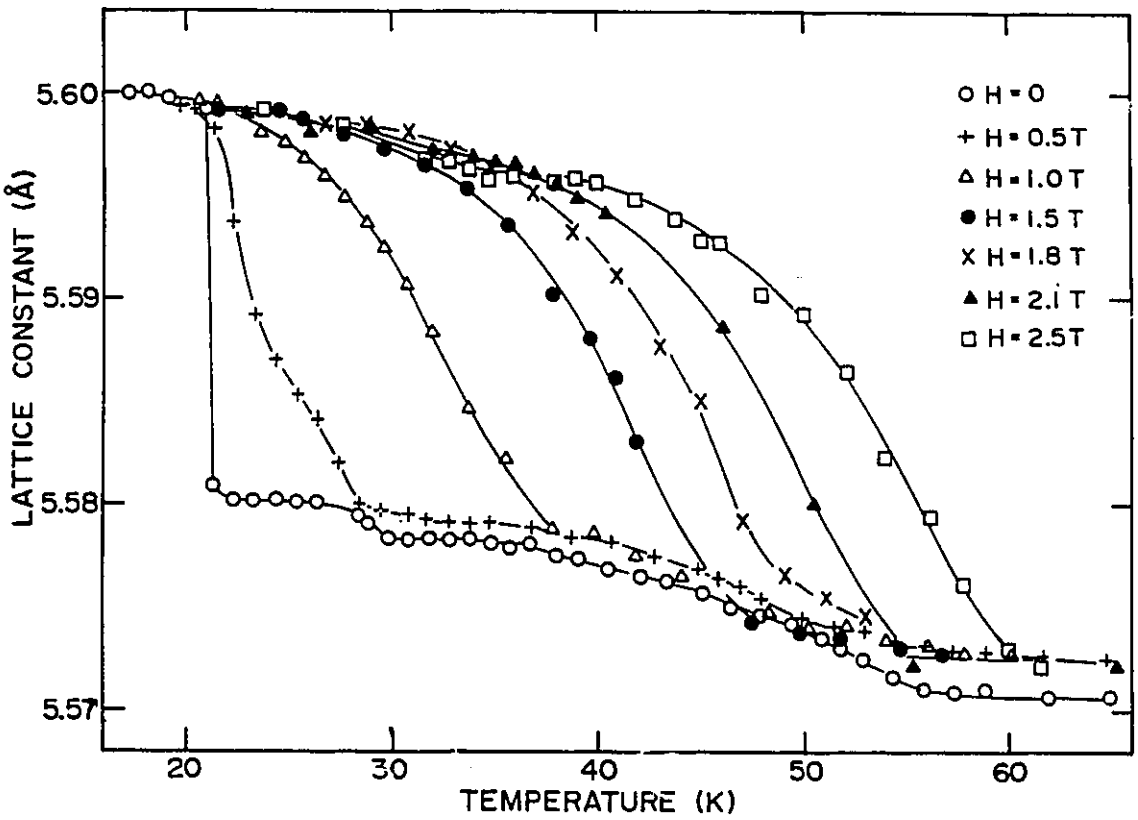

Figure 4.4 The lattice parameter c as a function of increasing temperature at different fields along the c axis. The large change in c from about 5.60Å to 5.58Å corresponds to the phase transition from the cone phase to the intermediate phase. Small steps correspond to the lock-ins in the magnetic structure.

the nature of the magnetic phase. Within a phase the field and lock-ins give smaller effects. Small steps seen at 5.600, 5.580, 5.578, 5.596 and 5.573Å correspond to the lock-ins of $\mathbf{q}=5/21\mathbf{c}^*$, $1/4\mathbf{c}^*$ and $5/19\mathbf{c}^*$ in zero field and $1/4\mathbf{c}^*$ and $2/7\mathbf{c}^*$ in a non-zero field.

4.3 Magnetic Phase Diagram

The magnetic field-temperature phase diagram was established by measuring certain magnetic reflections over a wide range of temperature and field. Figure 4.5 summarises the results. The filled circles and the crosses are from the experimental data. The solid and dashed lines are guides to the eyes. The phase diagram is set for increasing temperature.

The filled circles in the figure are the phase boundaries as determined from changes in the location or the intensity of the Bragg peaks. These boundaries are marked by the solid lines. The disappearance of the (1,1,q) and the (0,0,2-q) reflections were used to determine the upper and lower boundaries of the CAM phase respectively. Examples of this determination are shown in figure 4.3(b). The phase boundary between the cone and the intermediate phase may be determined in several ways. There is a sudden increase of the intensity of the (1,1,q) reflection (one example at a field of 1.7T is shown in figure 4.3(b)) and of the (1,1,2-5q) reflection which is the fundamental and fifth harmonics of

wave vector in the intermediate phase respectively; there is also a sudden decrease of the intensity of (1,1,0) which describes the ferromagnetic components in the cone phase. The changes are accompanied by a decrease of about 0.4% in the lattice parameter c as was noted also by Habenschuss et al[62]. The phase transition takes place from 21K in zero field to 59K in a field of 2.5 T. Its location can be described by Hc=0.06(Tc-21) Tesla at temperatures above 25K. Comparison with the results of magnetization data shows a difference of 0.18 Tesla for Hc. This can be reasonably considered as due to the demagnetization effect, and our result is consistent with the magnetization measurements. The line marking the high-field limit of the CAM phase is taken from the magnetization data[69,71,72], which shows the location the first order ferromagnetic phase transition.

The crosses in figure 4.5 are experimental points which correspond to lock-ins at rational-fractional values of q. We have found six islands, each corresponding to a lock-in, in the sea of incommensurate structures. The dashed lines are the boundaries between the commensurate and incommensurate phases. The transition temperature for these lock-ins was determined from data such as that shown in figure 4.3(a). Some of the lock-in regions extend to the boundary between the cone and intermediate phases. The transitions along thisboundary can be three types: incommensurate to commensurate (H<0.5T,

H>1.5 T), commensurate to commensurate (H=0T) and incommensurate to incommensurate (0.5T<H<1.5T except close to 1.3T).

When the xy components of the moments become disordered, the commensurate structure with wave vector q=2/7 persists through the phase boundary above a field of 0.5T. The experimental data at 2.5T indicates that q moves away from 2/7 between 70 and 75K. This suggests that there may exist a boundary for the q=2/7 island in the CAM phase which is shown by the dashed-dot line.

Although no data in fields were taken at low temperatures, extrapolating the data from just above 21K in figure 4.1 leads to the conclusion that there is a boundary for the $q=5/21c^*$ commensurate structure in the cone phase which is temperature independent. Measurements by Atoji[64] lead to the same conclusion of a lock-in at $q=5/21c^*$ at low temperature in a field of 2.0 T.

Our measurements show that the line on the phase diagram marking the transition from order to disorder of moments in the ab plane persists above 2.5 T. This suggests that the region labelled F in figure 4.5 corresponds to a ferromagnetic phase where all moments align in the field direction. We have not determined if there is a boundary between this phase and the paramagnetic phase.

Figure 4.6(a) shows the integrated intensity of the (0,0,2-q) magnetic Bragg peak in zero field as a function of

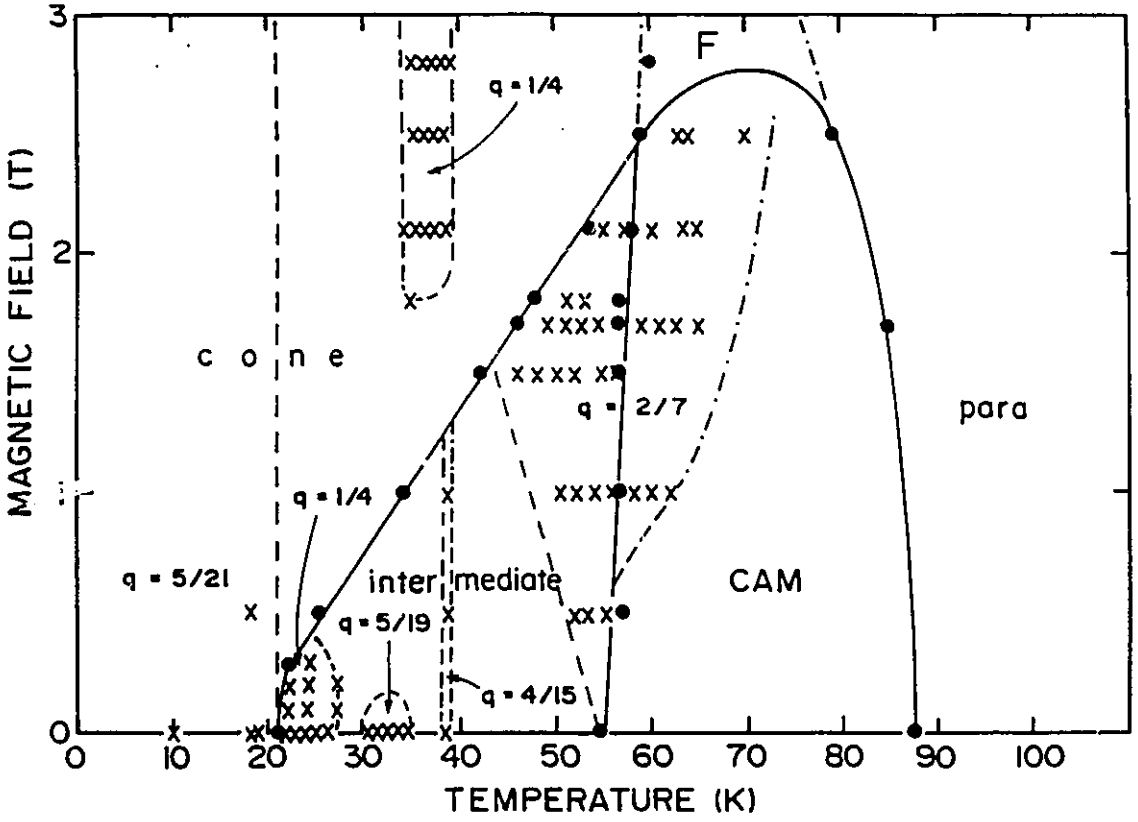

Figure 4.5 Magnetic phase diagram of erbium, with the increasing temperature and applied field along the c axis. The dots are measurements of the phase transition temperature. The crosses are experimental points corresponding to lock-ins. The lines are guides to the eyes. The solid line is the boundary between two distinct phases. The dashed line is the boundary between commensurate and incommensurate phases. The dashed-dot line corresponds to boundaries whose location has not been accurately determined.

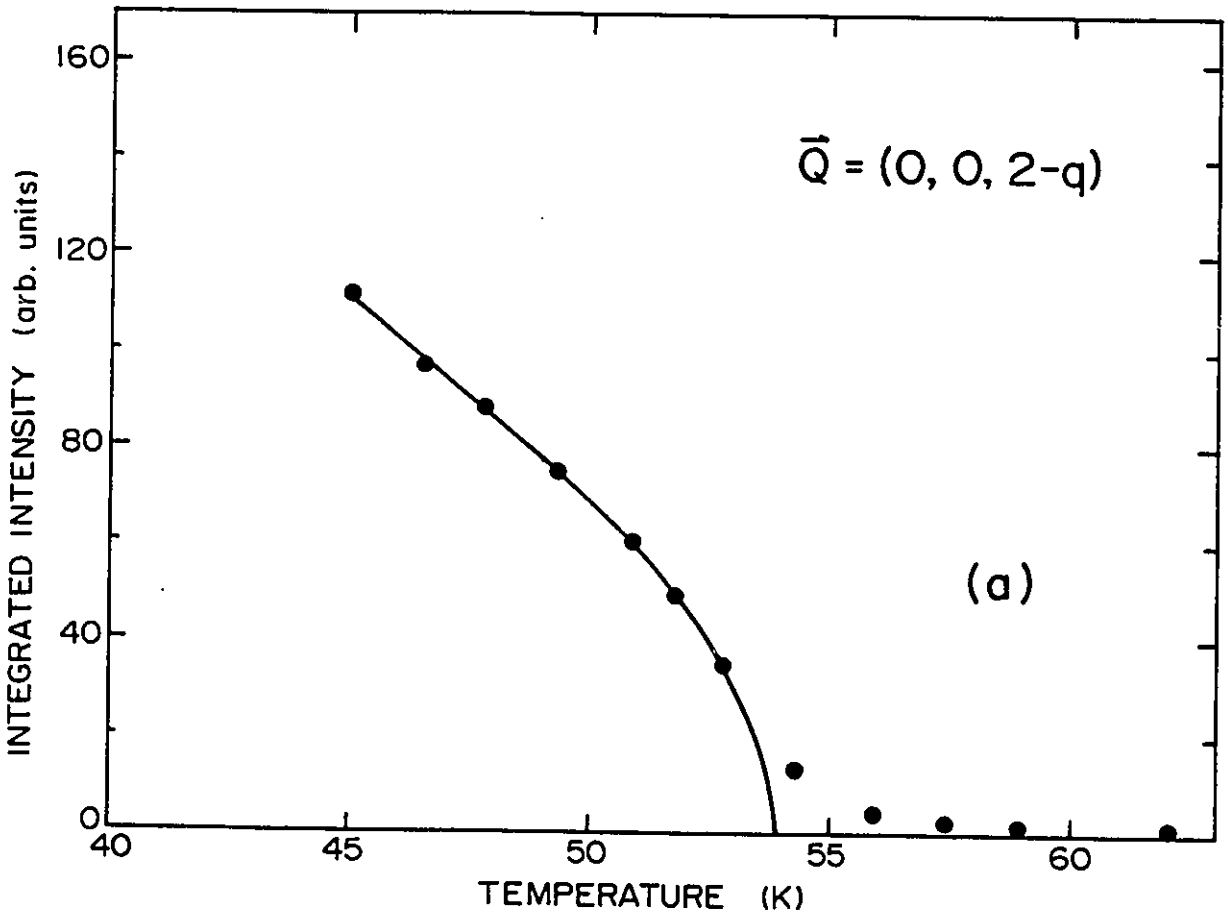

Figure 4.6(a) Temperature dependence of the integrated intensity of the (0,0,2-q) magnetic Bragg peak near the phase transition between the intermediate and CAM phases.

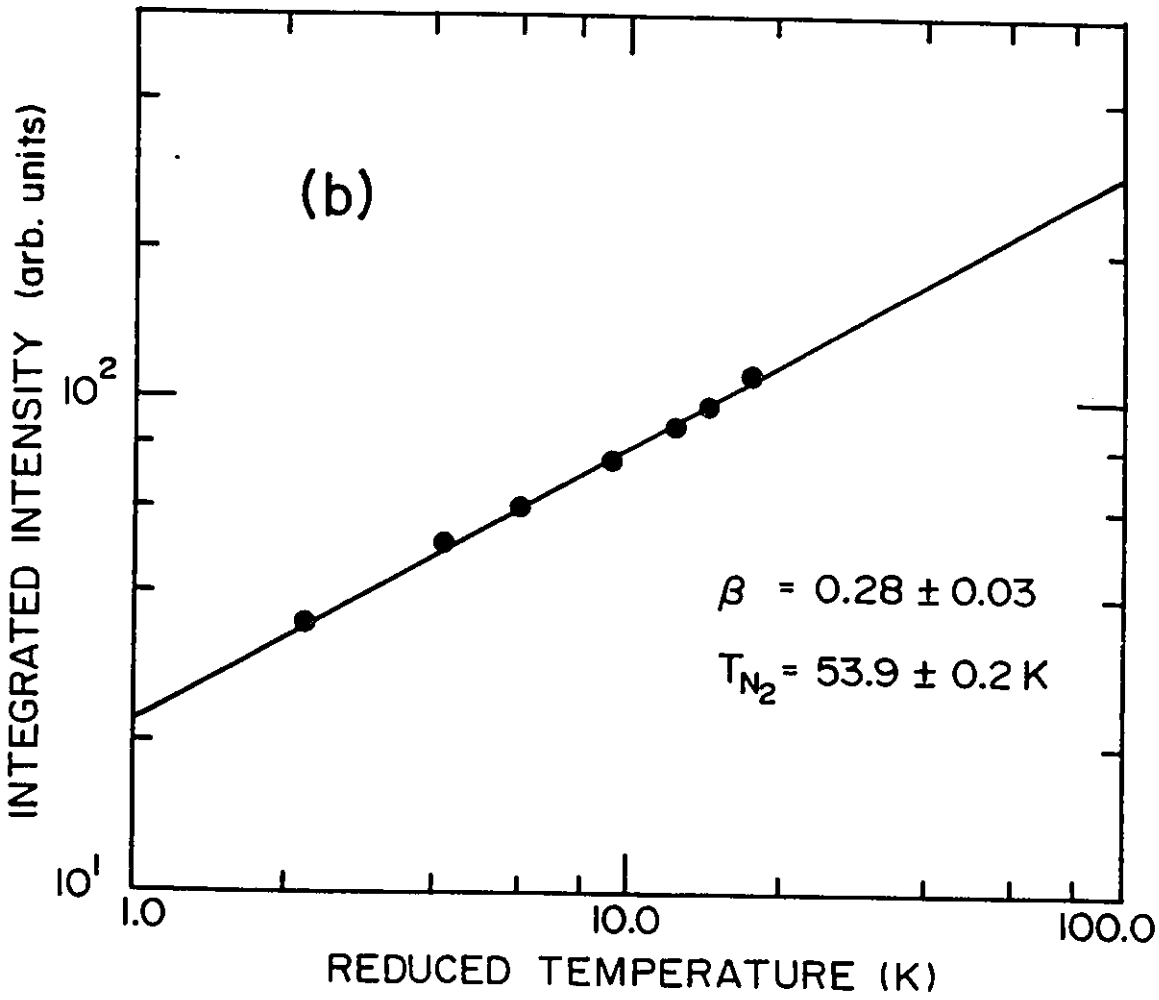

Figure 4.6(b) Log-log plot of integrated intensity vs reduced temperature. Least square fitting gives a critical exponent β of 0.28±0.03 and phase transition temperature T_{N2} of 53.9±0.2K.

temperature in the phase transition region when the xy components of the moments start to order. Figure 4.6(b) shows a linear behaviour of the integrated intensity against the reduced temperature in a log-log plot. The data indicate that the phase transition from the intermediate phase to the CAM phase is a critical phase transition. A least square fitting to the power law between the temperatures of 46 and 53K gives the critical exponent for the fundamental wave vector β=0.275±0.03 with T_N=53.9±0.2K.

4.4 Magnetic Structures

4.4.1 Cone phase

The application of a magnetic field along the c axis serves to close up the cone angle. The average half angle of the cone in our sample, as determined from the intensity of the (0,0,2-q) reflection and from the magnetization data[71], decreases gradually from 29° at zero field and 10K to 19° at 2.5T and 52K.

In addition to the first order magnetic satellites, we observed harmonics in this phase which are not described in the earlier literature. Figure 4.7 shows the diffraction pattern along the [00ℓ] direction on a logarithmic scale at zero field and 10K, where q is locked in at 5/21. The harmonic peaks can be indexed as (0,0,2n±1/21) and (0,0,2n± 11/21) which correspond to the 17th and 19th harmonics respectively

of the fundamental (0,0,2n±5/21). If we notice that the peak intensity of those harmonics are about 0.4% of the fundamental, and the position of q=1/21 is only 0.048 r.l.u. away from that of nuclear peak, it is not surperizing that they are easy to miss. As suggested by Gibbs, Bohr et al[20], the q=5/21c* structure can be described by a basal-plane spin-slip model where the spin-slip pattern has a complicated period. There are three slips every seven atomic layers, and the pattern repeats six times in one magnetic unit cell. If "." is a single spin that lies along the easy axis and "1" is a pair of spins that deviate from the easy axis by an angle ±α, they have proposed that $(..1.1)^6$ is the spin ccnfiguration in the basal plane. The insert to figure 4.7 shows the first eight layers of this basal-plane spin-slip model. Another alternative arrangement of the spin configuration is $(.11..)^6$ where two pairs are neighbours. However, the latter contributes too much intensity to the harmonics and is ruled out by our results. Table 4.1 shows the calculated structure factor for the $(..1.1)^6$ configuration with $\alpha=2\pi/17=21.2^\circ$ and with the z component of the moments ferromagnetically aligned. The model generates harmonic peaks at (h,k,2n±m/21) with m=1,7,11,13,19. α has been chosen so that the harmonics with m=1 and 11 have the strongest intensity. There is reasonable agreement with experiment.

Unexpectedly the forbidden nuclear peak (1,1,1) was

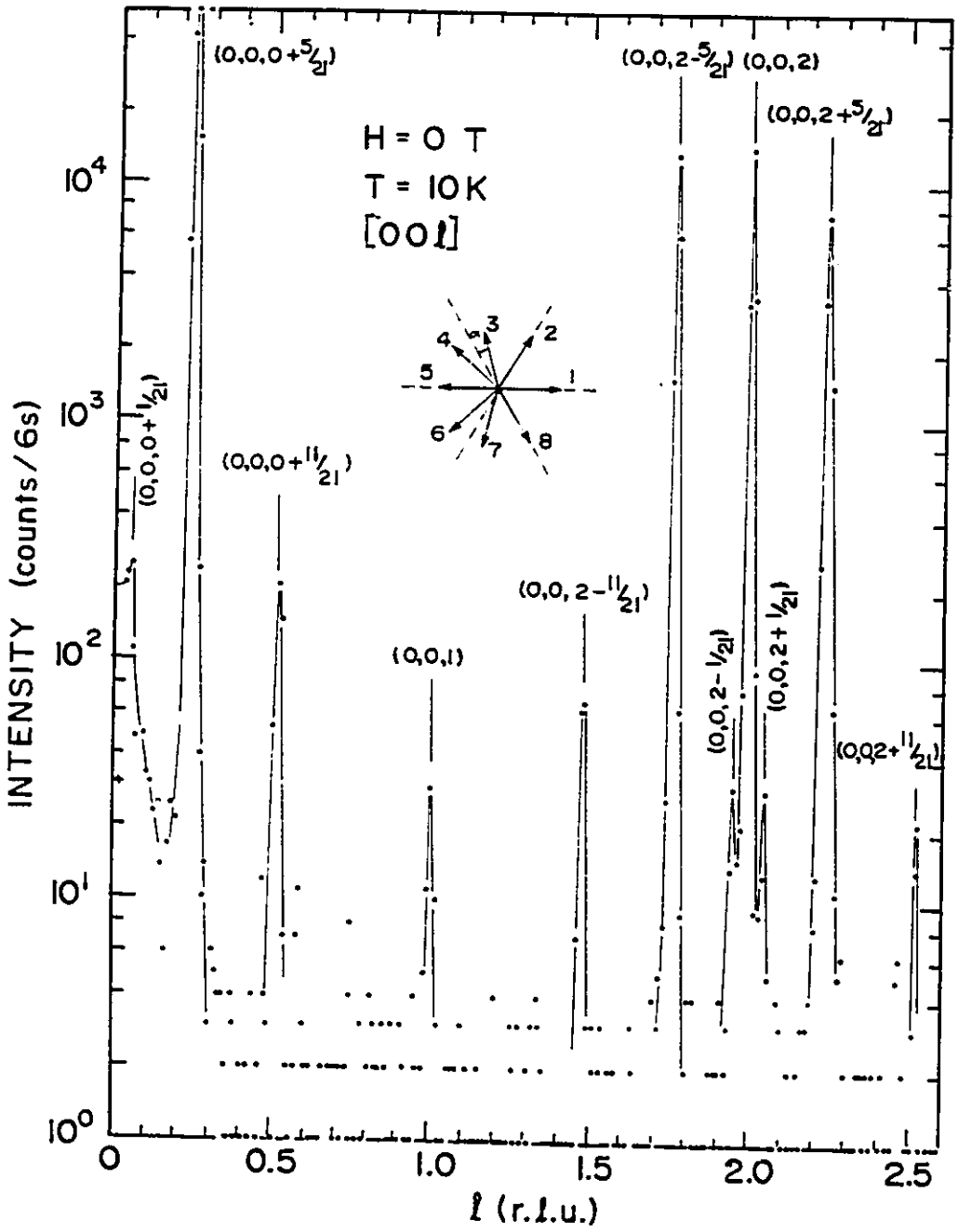

Figure 4.7 Diffraction pattern from the q=5/21c* cone phase at 0T and 10K along the [00ℓ] direction. The insert shows the first eight layers of the basal plane spin-slip model for this structure.

TABLE 4.1. Square of the magnetic structure factor relative to the nuclear structure factor in erbium at 10K and zero field. This corresponds to the cone phase with q=5/21c. The calculated values are for a ferromagnetic moment of 7.0 μ_B along c and a moment of 4.5 μ_B in the basal plane rotating according to the spin-slip model.*

	$\lvert F_{xy}^m(Q) / F^n(Q) \rvert^2$					$\lvert F_z^m(Q)/F^n(Q) \rvert^2$	
ℓ	1/21	5/21	11/21	13/21	19/21	0	16/21
obs.							
0,0,2+ℓ	0.05	16	0.05	0.00	0.00	-	-
0,0,2-ℓ	0.04	19	0.07	0.00	0.00	-	-
0,0,0+ℓ	0.09	12	0.09	0.00	0.00	-	-
1,1,2-ℓ	-	12	0.08	0.00	0.00	70	0.8
1,1,0+ℓ	-	11	0.09	0.00	0.00	81	0.2
1,1,1							3.4
average	0.06 ±0.02	14 ±3	0.08 ±0.02	0.00 ±0.01	0.00 ±0.01	76 ±6	
calc.	0.06	15.6	0.05	0.02	0.01	76	0

observed in all structures of the cone phase, an example can be seen in table 4.1. This was also noted by Rhyne and Pickart[63]. The peak is likely to be non-magnetic in origin. Its existence implies a lowering of the hcp symmetry, presumably induced by magnetostrictive effects. The reason why it is non-magnetic in origin is that the observed intensity of the peak corresponds to a moment of about 1.6 μ_B along the c axis, which implies a difference of moment between the two successive ferromagnetic sheets in the c direction. This is in contradiction with the experimental data.

The Bragg peak at the (1,1,1±5/21) position, is also

not explained by the spin-slip model.It could he a satellite to a nuclear (1,1,1) peak. Alternatively it is possible that the z component of the moments is modulated, though our data are rather insensitive to this effect.

In the new lock-in phase induced by the field at $\mathbf{q}=1/4\mathbf{c}^*$ harmonics of type (0,0,2n±1/2) type were observed. The ratio of their intensity to the fundamental magnetic satellites is 0.5 to 1.5%. The data can be qualitatively explained in terms of the basal-plane spin-slip model, shown as an insert in figure 4.7. An analysis for $\mathbf{q}=0.250\pm0.002\mathbf{c}^*$ at 2.5T and 36K gives $\alpha=18^\circ$. The cone angle in this phase is about 21°.

Weak harmonics of type (0,0,2n±0.532) were observed in the incommensurate cone phase with $\mathbf{q}=0.242\pm0.001\mathbf{c}^*$ at 1.5T and 23K. These harmonics correspond to (11/5)**q**.

4.4.2 Intermediate phase

Surveys were taken along [00ℓ] and [11ℓ] for $\mathbf{q}=2/7\mathbf{c}^*$ at 2.1T and 55K; for $\mathbf{q}=1/4\mathbf{c}^*$, $\mathbf{q}=5/19\mathbf{c}^*$ and $\mathbf{q}=0.277\pm0.002\mathbf{c}^*$ at 0T and 23K, 33K and 46K respectively.

Figure 4.8(a) and (b) shows the diffraction pattern of the phase with $\mathbf{q}=1/4\mathbf{c}^*$ in zero field. As was the case with the cone phase at low temperatures, we also observed harmonics that not in literature. Except for (0,0,2-1/2), there always exist magnetic peaks corresponding to the second harmonics of the fundamental. Thess second harmonics are not seen in any

other structures in the intermediate phase. Their appearance suggests that the basal-plane spin-slip model may also be applied to the xy components of the moments in this phase. The scattering from the z component of the moments is consistent with a completely squared-up structure that has four layers of "up" spins followed by four layers of "down" spins. Table 4.2 gives a comparison of the experiment and the theory. The fitted value of the moment is $\mu_{xy}=4.3\mu_B$ in the basal plane and $\mu_z=7.3\ \mu_B$ along the c axis. The scattering from the second order harmonic is just from the contribution due to the xy components of the moments. The pattern of the spin-slips in the basal plane is shown as an insert in figure 4.8(a) with $\alpha=3^\circ$. In this case, the single spin can be at an angle α from the easy axis. This model is in agreement with the experimental data.

As the temperature increases, the intensity of the harmonics along the [11ℓ] direction falls faster than that of the fundamental. The temperature dependence of these harmonics has been studied in detail by Habenschuss et al[62]. Our data both in the $\mathbf{q}=5/19\mathbf{c}^*$ and $\mathbf{q}=0.277\pm0.002\mathbf{c}^*$ phases show that the intensities of the harmonics are weaker than those predicted by the c-axis spin-slip model. This indicates an increased rounding of the squared-up structure of the z component of the moments as the temperature increases. Along the [00ℓ] direction, no harmonics were observed for the $\mathbf{q}=2/7\mathbf{c}^*$ phase.

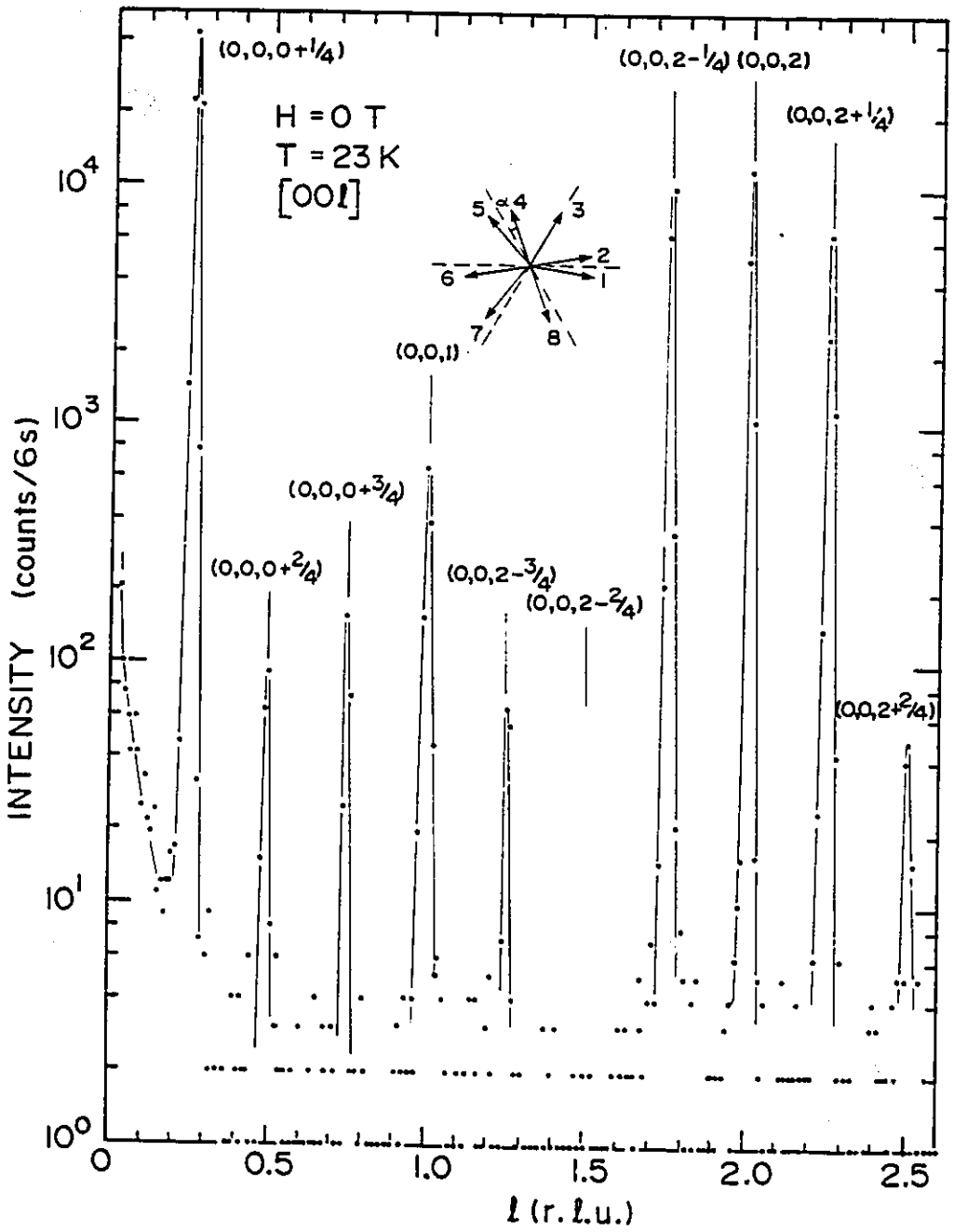

Figure 4.8(a) Diffraction pattern of the intermediate phase locked in at $q=1/4c^*$ at 0T and 23K, along the [00ℓ] direction. The insert shows the basal plane spin-slips.

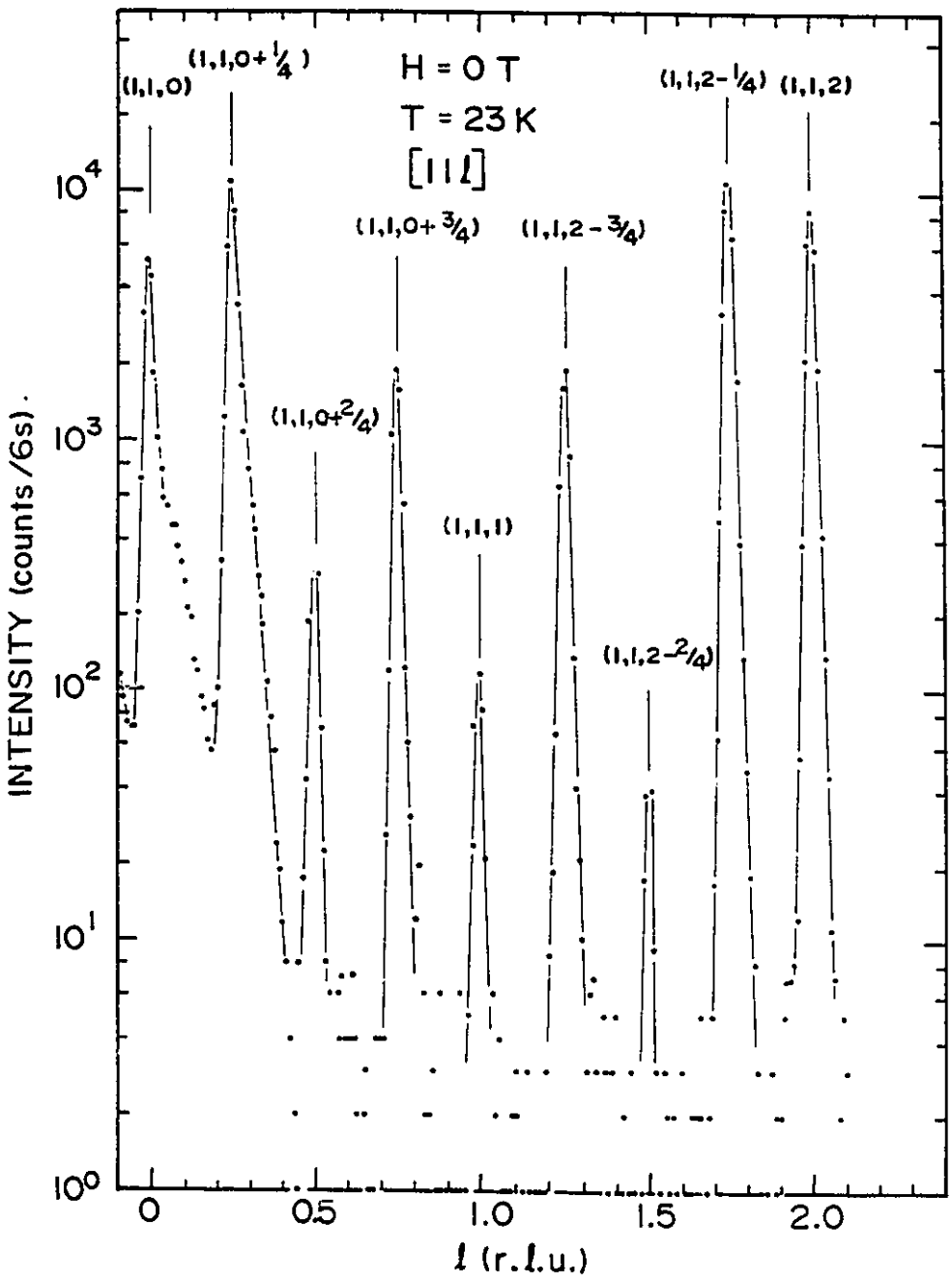

Figure 4.8(b) Diffraction pattern of the intermediate phase locked in at $q=1/4c^*$ at 0T and 23K, along the [11ℓ] direction.

TABLE 4.2. Square of the magnetic structure factor relative to the nuclear structure factor in erbium at 23K and zero field, and $G^2 \equiv (1+Q_z^2)\,|F_{xy}^m(Q)/F^n(Q)|^2 + (1-Q_z^2)\,|F_z^m(Q)/Fn(Q)|^2$. *The data are for the spin-slip phase with* $q=1/4c^*$. *The calculated values correspond to a squared-up (4,4) structure along the c axis and the basal-plane spin-slip model.*

$\lvert F_{xy}^m(Q) / F^n(Q) \rvert^2$					
ℓ	0	1/4	2/4	3/4	4/4
obs.					
0,0,4-ℓ	-	13	0.00	0.15	0.16
0,0,2+ℓ	0	14	0.12	0.08	-
0,0,2-ℓ	-	16	0.00	0.06	(0.52)
0,0,0+ℓ	-	11	0.02	0.08	-
average	0±1	13±2	0.03±0.04	0.09±0.03	0.16±0.03
calc.	0.14	14	0.10	0.06	0.14
G^2					
ℓ	0	1/4	2/4	3/4	4/4
obs 1,1,ℓ	0±1	42±4	0.12±0.02	6.9±0.4	0.12±0.03
calc.	0.14	49	0.11	5.8	0.15
Obs 1,1,2-ℓ	0±1	42±4	0.15±0.02	6.7±0.4	0.12±0.03
cal.	0.18	44	0.12	5.3	0.15

Third and fifth harmonics were seen for the $\mathbf{q}=5/19\mathbf{c}^*$ and $\mathbf{q}=0.277\pm0.002\mathbf{c}^*$ phases. However, it is difficult to find any spin-slip pattern in the basal plane to explain all of the observed harmonics in the latter two phases. This implies a break-down of the basal-plane spin-slip model as the temperature rises.

We note that the (0,0,1) peak has significant

intensity in all structures of the intermediate phase and the intensity decreases as the temperature increases. Its intensity is 1.5 to 5 % of that of the (0,0,2) nuclear peak, a value that is much larger than the observed 0.2 % in the cone phase which is considered to be the $\lambda/4$ contamination of the beam. If we postulate that the intensity of the (1,1,1) peak arises solely from the scattering due to the moment in the basal plane, the intensity of the (0,0,1) peak is still considerably larger than would be produced by this basal plane moment. An example is given in Table 4.2. Therefore the major component of the scattering from (0,0,1) is likely to be nuclear rather than magnetic scattering. There must be a lowering of the hcp symmetry, caused presumably by the magnetostriction.

4.4.3 CAM phase

A survey with Q in the range of (0,0,0.1)-(0,0,4) and (1,1,-0.44)-(1,1,2.44) was conducted for fields of 0, 1.7T and 2.1T at a temperature of 65K and for a field of 2.5T at 70K and 78K. The average value of q is 0.292±0.003, 0.287±0.003, 0.288±0.002, 0.285±0.003 and 0.279±0.003 respectively. Only the first and last of these five values are significantly different from 2/7 (0.286). The ratio of the intensities of the first order magnetic satellites to the nuclear peaks along [00ℓ] for all of the data is not greater than 0.5%, which is consistent with no magnetic ordering in the ab plane in this

phase.

Higher order harmonics were observed along [11ℓ]. The sole exception is at 2.5T and 78K, near the Neel temperature, where the structure is sinusoidal.

The c-axis spin-slip model was applied to the $\mathbf{q}=2/7\mathbf{c}^*$ phase. We note that spin-slips form a 4,3 and not a 4,3,3,4 repeat unit since the latter requires that the harmonics at $\ell=m/7$ with m odd are of the same order of intensity as the harmonic $\ell=6/7$, which was not observed. However, the measured intensities of the fundamental wave vector are much stronger than predicted for a squared-up structure, so that the squaring up is incomplete. The structure of the phase with $\mathbf{q}=2/7\mathbf{c}^*$ can be regarded as a superposition of the squared-up structure and the sinusoidal structure. The fact that this analysis is correct for different fields implies that the field does not change the spin-slip configuration in the $\mathbf{q}=2/7\mathbf{c}^*$ phase. Table 4.3 lists the observed and calculated magnetic structure factor for the $\mathbf{q}=2/7\mathbf{c}^*$ phase at 1.7T and 65K. The moment associated with the sinusoidal wave is $\mu_0=4.6\mu_B$ and the amplitude of the squared-up structure is $\mu_s=1.5\mu_B$. A small net ferromagnetic moment predicted by the model is not detectable in our experiments because its scattering is masked by the nuclear Bragg peaks but would be seen in megnetization measurements. The observed peak at $\ell=5/7\mathbf{c}^*$ cannot be described within this model. However, if a symmetry breaking occurs that

TABLE 4.3. Square of the magnetic structure factor relative to the nuclear structure factor in erbium at 65 K and 1.7 T in the CAM phase, locked in at q=2/7. The calculated values correspond to a superposition of the squared-up (4,3) structure and a sinusoidal structure with the same period.

	$\lvert F_z^m(Q) / F^n(Q) \rvert^2$							
ℓ	0/7	1/7	2/7	3/7	4/7	5/7	6/7	7/7
obs.								
1,1,2+ℓ	0	0.00	15					
1,1,2-ℓ	0	0.00	16	0.00	0.15	0.24	0.14	0.00
1,1,0+ℓ	0	0.00	15	0.00	0.17	0.01	0.15	0.00
average	0±2	0.00 ±0.01	15±2	0.00 ±0.01	0.16 ±0.02	0.13 ±0.10	0.15 ±0.02	0.00 ±0.02
calc.	0.08	0	15.3	0	0.09	0	0.19	0

distinguishes between the two sublattices, {R=(0,0,0) and R=(1/3,2/3,1/2)}, this harmonics can be understood by the two sublattices having phase angles differing by about 2.3°.

4.5 Discussion and Conclusions

This thesis gives results regarding the magnetic structure of erbium in zero field and regarding the effect of a magnetic field along the c axis.

In the cone phase, the existence of weak harmonics along the [00ℓ] direction indicates that the xy components of the moments, ferromagnetically aligned within the basal planes, do not rotate uniformly from layer to layer along the c axis. The agreement between the experiment and the basal-plane spin-slip model for the q=5/21c* structure in zero field

suggests that the moments are influenced by a hexagonal anisotropy in the ab plane. Although this anisotropy energy is much less than the energy of the axial anisotropy, it is nonetheless important in determining the lock-ins. An alternative treatment of the hexagonal anisotropy without spin-slip predicts that the fifth and seventh harmonics will be observed and does not fit our data.

A model with completely squared-up c-axis moments and basal-plane spin-slips gives a reasonable explanation of the data for the $\mathbf{q}=1/4\mathbf{c}^*$ structure in the intermediate phase. This implies that the hodograph of the moment is a tilted helix just above Tc. The result agrees with that of Cable and is not contradictory with the theory of Jensen and Mackintosh who predict the tilted helix can be stable in some of the commensurate structures just above Tc, when the cycloidal phase is disrupted by the first order transition to the cone phase. As the temperature is increased, the hexagonal anisotropy becomes less important. The driving forces for the lock-in to commensurate phases are the axial anisotropy of the crystal field and the magnetostriction. The lock-ins are primarily determined by the z component of the moments. The structures with $\mathbf{q}=2/7\mathbf{c}^*$ and $\mathbf{q}=5/19\mathbf{c}^*$ show an incomplete squaring-up of the z component of the moments. The model takes care of a difficulty that early workers had, in that the structures which it predicts have no atom with a moment

greater than that allowed by theory. Our study also confirms the three dimensional character of the lock-ins in the intermediate phase and the sample dependence of the lock-ins.

The effect of a field along the c axis on the lock-ins is interesting and supports the contention above that the lock-ins are primarily determined by the z component of the moments. The extent of the $\mathbf{q}=5/21\mathbf{c}^*$ cone phase at low temperatures is unaffected by the field. A new lock-in appears in the cone phase at $\mathbf{q}=1/4\mathbf{c}^*$ for fields above 1.8 T. In the intermediate phase, the $\mathbf{q}=5/19\mathbf{c}^*$ lock-in is destroyed rapidly and the $\mathbf{q}=4/15\mathbf{c}^*$ lock-in is sustained. The $\mathbf{q}=2/7\mathbf{c}^*$ lock-in is extended considerably both in the intermediate and CAM phase. The latter two structures possess small net magnetic moments parallel to the c axis according to the c-axis spin-slip model, so it seems that lock-ins with ferrimagnetism along the c axis are stabilised by the field and those without ferrimagnetism are destabilised. There is no evidence that the field modifies the configuration of the spin-slip structure.

The lattice parameter c also shows the lock-ins over the same region of the temperature as the magnetic structure. This can only arise from the effect of the magnetostriction.

The field and temperature dependence of the magnetic structure is described in the magnetic phase diagram. At least three distinct types of ordered phase, the cone phase, the intermediate phase and the CAM phase exist for fields below

2.5T. The boundary between the intermediate and the CAM phase is almost field independent. This indicates that the field along the c axis has little influence on the xy components of the moments. The magnitude of the wave vector q, in general, increases with increasing temperature and decreases with increasing field.

There are contradictory results in the literature about the character of the phase transition between the intermediate and CAM phases. The neutron experiments by Habenschuss et al[62] a show significant broadening of the magnetic peaks just above the transition temperature and no appreciable hysteresis. This indicates a second order phase transition. The most convincing evidence for a first order phase transition is that given by Aström and Benediktsson with a thermal hysteresis of 3K in microcalorimeter measurements[77]. Our measurements show a continuous change to zero of the integrated intensity of the magnetic peak. The variation of this intensity with temperature can be fitted to a power law of the type found for a critical phase transition with the critical exponent $\beta=0.28\pm0.03$. Since the intermediate temperature phase has the spin either confined in the ac plane or tilted away from the c axis, a theoretical model is needed to calculate the critical exponents with the space dimensionality d=3, and the spin dimensionality D=4 or 6 incommensurate modulated phase, as would be indicated by arguments of the

type used by Mukamel[46]. The value observed for β is significantly smaller than would be predicted for such a model. Bohr et al[19] have suggested that the critical exponent β is reduced by magnetostrictive effects for a similar phase transition in terbium. The reduction brings the value of β down so as to be in the range 0.25 to 0.30, which would be in agreement with our experimental value of 0.28.

Most theoretical works are based on mean field theory[11,15,34,36,37,38]. The essential idea is to take the thermal average of the values of operators in Hamiltonian on the surroundings of any particular ion, so that the interactions of two ions is replaced by effective one ion terms. The most complete calculation of the magnetic ordering in erbium has been done by Jensen[15,65]. He considers the crystal field anisotropy, dipolar interaction, isotropic exchange, and anisotropic two ion exchange as deduced from the spin wave dispersion[78]. The theory predicts that a longitudinal sinusoidal wave along the c axis is stable just below the Neel temperature T_{N1} since the anisotropy parameter of crystal field B_2^0 is negative for erbium. (2p+1) harmonics develop with the magnetization $\sigma^{2p+1} \propto (T-T_{N1})^{2p+1/2}$as the temperature decreases, and the moments approach a square wave at low temperatures. The divergence of the basal plane components of the susceptibility leads to the ordering of the basal plane moments at T_{N2}, and a minimum of the free energy requires the modulation of both

the x and y component of the moments to be locked at 90° out of phase with that of the z component of the moments. This results in moments confined to a single direction in the basal plane. Since the anisotropy parameter B_6^6 is negative, meaning that the a axis is the easy axis in the basal plane whose value is comparable with that in Ho, the linearly-polarized moment lies on the a axis. Hence the structure is an elliptic cycloidal with its principal axes along the a and c directions in the intermediate temperature phase. The odd harmonics will appear in the basal plane as a reflection of the z component of the moments because of the phase-locking of the components. When the anisotropy parameters B_4^0 and B_6^0 are considered, the structure favours the orientation which makes an angle with the c axis. It may go through a second order transition to a tilted helix if the system is already a cycloidal structure. The transition to the cone phase is due to the dipole-dipole interaction and magnetostriction.

So far, no quantitative prediction regarding the commensurate to incommensurate phase transition has been made. The lock-ins can be understood as a result of anisotropy or magnetostriction and of the temperature dependence of the exchange interaction $J(\mathbf{q})$. For the former, the axial anisotropy or magnetoelastic energy favours the maximum ordered moment at each site which gives rise to commensurate structures. For the latter, the exchange energy is lower when

there is a coalesence of superzones at the Fermi surface in the commensurate phase. A soliton theory based on the axial next-nearest-neighbour Ising (ANNNI) model was suggested by Bak and Boehm[39] to explain the lock-in for the z component of the moments by a "devil's staircase" mechanism. It predicts the low temperature structure of the z component of the moments to be the 1/4 structure, not the cone structure. Its attraction is that it can predict a "staircase" of lock-ins, as is observed. However this model is clearly incomplete for erbium because it does not take into account the xy components of the moments.

In conclusion, the experimental data shows ample evidence that the ideas of Jensen, regarding the basic interactions, of Bak and Boehm regarding the devil's staircase for the z component of the moments, and Bohr et al regarding spin-slips in the basal plane, are appropriate for erbium. A complete description of the magnetic properties may need to incorporate all these features.

APPENDIX

For Bragg scattering, the intensity of the peak depends on the resolution function which is determined by the collimations and mosaic spreads. These instrumental parameters of a triple axis spectrometer are the horizontal mosaic spreads of the monochromator η_M and of the analyzer η_A, the horizontal collimation angle α_j of the collimators C_j (figure 2.1), where j=0,1,2,3 implies for in-pile, monochromator to sample, sample to analyzer, and analyzer to detector respectively.

In this Appendix we give results derived by Cooper and Nathan[53], and Cowley and Bates[17] for the correction to Bragg intensities due to instrumental resolution of a triple-axis spectrometer.

The Lorentz term $\mathcal{L}(\theta)$ in eqn (2.15) for the peak intensity of a Bragg reflection is given by

$$\mathcal{L}(\theta) = (\sin 2\theta)^{-1} (A')^{-\frac{1}{2}} \qquad (A.1)$$

where θ is Bragg angle and A′ is given by

$$A' = (b_1+b_2)\tan^2\theta + 2(b_4-b_0)\tan\theta + b_3 + b_5 \qquad (A.2)$$

where b_0, ..., b_5 are determined by the instrumental parameters, as summarized in table A.1. The peak intensity is independent of the path in reciprocal space along which a scan is conducted.

The integrated intensity of a Bragg peak has a complicated Lorentz factor because it depends on how the measurement tracks through the peak. If a scan is conducted in constant wave vector steps along a line at an angle α to the wave vector transfer Q (figure 2.2), $\mathcal{L}(\theta)$ is given by

$$\mathcal{L}(\theta) = (\sin 2\theta)^{-1}\left(\frac{\cos^2\alpha}{\cos^2\theta}B_{11} + 2\frac{\sin 2\alpha}{\sin 2\theta}B_{12} + \frac{\sin^2\alpha}{\sin^2\theta}B_{22}\right)^{-\frac{1}{2}} \qquad (A.3)$$

where

$$B_{11} = (b_1+b_2)(b_3+b_5) - (b_4-b_0)^2 \qquad (A.4)$$

$$B_{12} = 2(b_1b_4+b_0b_2)\tan\theta + b_4^2 - b_0^2 + (b_1-b_2)(b_3+b_5) \qquad (A.5)$$

$$B_{22} = 4b_1b_2\tan^2\theta + 4(b_1b_4 - b_2b_0)\tan\theta + (b_1+b_2)(b_3+b_5) - (b_4+b_0)^2 \quad (A.6)$$

There are several particular case where eqn (A.3) can be simplified. If $\alpha=0$, so the scan is parallel to Q, the integrated intensity is proportional to $(2\sin\theta)^{-1}B_{11}^{-1/2}$, which is equivalent to the result for a two-axis diffracto-meter.

If there is an open detector which is also equiva-lent to a two-axis diffractometer, then $b_2=b_3=b_4=0$ and the integrated intensity is proportional to $(2\sin(\theta\pm\alpha))^{-1}B_{11}^{-1/2}$ There are also simplifications of eqn (A.3) if the monochro-mator and analyzer are identical and the collimations around them are symmetric.

Table A.1 The parameters used to determine the Lorentz factor for a triple-axis spectrometer. k is the neutron wave vector, θ_M (θ_A) is the Bragg angle of monochromator (analyzer), and η_M, η_A, and α_j are the instrumental parameters.

b	a	a
$b_0=a_1a_2+a_7a_8$	$a_1=\tan\theta_M/(\eta_M k)$	$a_6=-1/(\eta_A k)$
$b_1=a_2^2+a_3^2+a_8^2$	$a_2=1/(\eta_M k)$	$a_7=2\tan\theta_M/(\alpha_0 k)$
$b_2=a_4^2+a_6^2+a_{10}^2$	$a_3=1/(\alpha_1 k)$	$a_8=1/(\alpha_0 k)$
$b_3=a_5^2+a_9^2$	$a_4=1/(\alpha_2 k)$	$a_9=2\tan\theta_A/(\alpha_3 k)$
$b_4=a_5a_6+a_9a_{10}$	$a_5=\tan(\theta_A)/(\eta_A k)$	$a_{10}=-1/(\alpha_3 k)$
$b_5=a_1^2+a_7^2$		

REFERENCES

1. H. Lin, L. Rebelsky, M.F. Collins, J.D. Garrett, and W.J.L. Buyers, Phys. Rev. B **43**, 13232 (1991).
2. L. Rebelsky, H. Lin, M.F. Collins, J.D. Garrett, W.J.L. Buyers, M.W. McElfresh, M.S. Torikachvili, S. Horn, and H. Borges, J. Appl. Phys. **69**, 4807 (1991).
3. L. Rebelsky, H. Lin, M.F. Collins, J.D. Garrett, W.J.L. Buyers, and M.W. McElfresh, Physics B, (1992).to appear.
4. H. Lin, M.F. Collins, T. Holden, and W. Wei, J. Magn. Magn. Mat., (1992). to appear.
5. T.E. Mason, H. Lin, M.F. Collins, W.J.L. Buyers, A.A. Menovsky, and J.A. Mydosh, Physica B **163**, 45 (1990).
6. C. Broholm, H. Lin, P.T. Mattews, T.E. Mason, W.J.L. Buyers, M.F. Collins, A.A. Menovsky, J.A. Medosh, and J.K. Kjems, Phys. Rev. B **43**, 12809 (1991).
7. R.A. Steeman, T.E. Mason, H. Lin, W.J.L. Buyers, A.A. Menovsky, M.F. Collins, E. Frikkee, G.J. Nieuwenhuys, and J.A. Mydosh, J. Appl. Phys. **67**, 5203 (1990).
8. B. Coqblin, in *Rare Earths and Actinides* (The Insititute of Physics, London and Bristol, 1971).
9. M.B. Maple, L.E. Delong and B.C. Sales, in *Handbook on the Physics and Chemistry of Rare Earths*, edited by

K.A. Gschneidner, Jr. and L.R. Eyring (North-Holland, Amsterdam, 1978), vol. 1.

10. R.A. Steeman, *Ph.D thesis*, the Univiersity of Leiden, Netherlands, 1989.

11. B. Coqblin, *The Electronic Structure of Rare-Earth Metals and Alloys: The Magnetic Heavy Rare-Earths*, (Academic Press, London, 1977).

12. W.C. Koehler, in *Magnetic Properties of Rare Earth Metal* edited by R.J. Elliott (Plenum, New York, 1972).

13. S.K. Sinha, in *Handbook on the Physics and Chemistry of Rare Earth*, edited by K.A. Gschneidner, Jr., and L.R. Eyring (North-Holland, Amsterdam, 1978), vol.1.

14. K.A. McEwen, in *Handbook on the Physics and Chemistry of Rare Earth*, edited by K.A. Gschneidner, Jr., and L.R. Eyring (North-Holland, Amsterdam, 1978), vol.1.

15. J. Jensen and A.R. Mackintosh, *Rare Earth Magnetism, The Structures and Excitations*, (Clarendon Press, Oxford, 1991).

16. D. Gibbs, E.E. Moncton, K.L. D'Amico, J. Bohr, and B.H. Grier, Phys. Rev. Lett. **55**, 234 (1985).

17. R.A. Cowley and S.B. Bates, J. Phys. C **21**, 4113 (1988).

18. D. Gibbs, J. Bohr, J.D. Axe, D.E. Moncton and K.L. D'Amico, Phys. Rev. B **34**, 8182 (1986).

19. J. Bohr, D. Gibbs and K. Huang, Phys. Rev. B **42**, 4322 (1990).

20. J. Bohr, D. Gibbs, D.E. Moncton and K.L. D'Amico, Physica **140A**, 349 (1986).

21. J. Bohr, D. Gibbs, J.D. Axe, D.E. Moncton, K.L. D'Amico, C.F. Majkrzak, J. Kwo, M. Hong, C.L. Chien, and J. Jensen, Physica B **159**, 93 (1989).

22. H.H. Hill, in *Plutonium and Other Actinides*, edited by W.N. Miner (AIME, New York, 1970).

23. K.H.J. Buschow and D.B. Demooij, Philips J. Res. **41**, 55 (1986).

24. T.T.M. Palstra, A.A. Menovsky, G.J. Nieuwenhuys, and J.A. Mydosh, J. Magn. Magn. Mat. **54**, 435 (1986).

25. H. Ptasiewicz-Bak, J. Leciejewicz, and A. Zygmunt, J. Phys. F **11**, 1225 (1981).

26. L. Chelmicki, J. Leciejewicz, and A. Zygmunt, J. Phys. Chem. Solids **46**, 529 (1985).

27. A. Szylula, S. Siek, J. Leciejewicz, A. Zygmunt, and Z. Ban, J. Phys. Chem. Solids **49**, 1113 (1988).

28. L. Rebelsky, M.W. McElfresh, M.S. Torikachvili, B.M. Powell, and M.B. Maple, J. Appl. Phys. **69**, 4810 (1991).

29. B.R. Cooper, in *Magnetic Properties of Rare Earth Metal*, edited by R. J. Elliott (Plenum, New York 1972).

30. R.J. Elliott and F.A. Wedgwood, Proc. Phys. Soc. **84**, 63 (1964).

31. B.R. Cooper, R. Siemann, D. Yang, P. Thayamballi, and .A Banerjea, in *Handbook on the Physcis and Chemistry of the*

Actinides, edited by A.J. Freeman and G.H.Lander (North-Holland, Amsterdam, 1985), vol.2.

32. K.W.H. Stevens, Proc. Phys. Soc. A **65**, 209 (1952).

33. E. Callen and H.B. Callen, Phys. Rev. **139**, A455 (1965).

34. B.R. Cooper, *Solid State Physics* (Academic Press),vol.21.

35. R.J. Elliott, *Magnetism II A* (Academic Press).

36. T. Nagamiya, *Solid State Physcis* (Academic Press),vol.20.

37. K. Yosida and H. Miwa, J. Appl. Phys. **32**, 85 (1961).

38. R.J. Elliott, Phys. Rev. **124**, 346 (1961).

39. P. Bak and J. von Boehm, Phys. Rev. B **21**, 5297 (1980).

40. *Multicritical Phenomena*, edited by R. Pynn and A. Skjeltorp (Plenum Press, New York, 1983).

41. H.E. Stanley, *Introduction to Phase Transitions and Critical Phenomena* (Oxford University Press, New York, 1971)

42. M.F. Collins, *Magnetic Critical Scattering* (Oxford University Press, New York, 1989).

43. P. de B. du Plessis, G.H.F. Brits, and G.A.Eloff, J. Phys. Collq. **49**, 353 (1988).

43a. B.D. Gaulin, M. Hagen, and H.R.Child, J. de Phys, C **8**, 327 (1988).

44. P.A. Lindgard, in *Neutron Diffraction*, edited by H. Dachs (Springer-Verlag, Berlin, 1978).

45. P. Bak and D. Mukamel, Phys. Rev. B **13**, 5086 (1976).

46. D. Mukamel, Phys. Rev. Lett. **34**, 481 (1975).

47. T.E. Mason, B.D. Gaulin, J.D. Garrett, Z. Tun, W.J.L. Buyers, and E.D. Isaacs, Phys. Rev. Lett. **65**, 3189 (1990).

48. G.E. Bacon, *Neutron Diffraction* (Oxford University Press, London, 1962).

49. W. Marshall and S.W. Loversey, *Theory of Thermal Neutron Scattering: The Use of Neutrons for the Investigation of Condensed Matter* (Oxford University Press, London 1971).

50. G.L. Squires, *Introduction to the Theory of Thermal Neutron Scattering* (Cambridge University Press, London, 1978).

51. *Methods of Experimental Physics 23 (A), Neutron Scattering*, edited by K. Sköld and D.L. Price (Academic Press, Inc. Orlando, Florida, 1986).

52. *Methods of Experimental Physics 23 (C), Neutron Scattering*, edited by K. Sköld and D.L. Price (Academic Press, Inc. Orlando, Florida, 1987).

53. M.J. Cooper and R. Nathans, Acta Cryst. **23**, 357 (1967).

54. D.C. Tennant, N. Kerley, and N. Killoran, Rev. Sci. Instrum. **60**, 136 (1989).

55. Y.B. Ning, J.D. Garrett, and W.R. Datars, Phys. Rev. B **42**, 8780 (1990).

56. Y.B. Ning, V.V. Gridin, C.V. Stager, W.R. Datars, A. LeDawson, and D. H. Ryan, J. Phys: Cond. Matter **3**,

4399 (1991)..

57. M.S. Torikachvili, R.F. Jardim, C.C. Becerra, C.H. Westphal, A. Paduan-Filho, W.M. Lopez, and L. Rebelsky. J. Magn. Magn. Mat. (1992). to appear.

58. A.J. Freeman, J.P. Desclaux, G.H. Lander, and J. Faber Jr., Phys. Rev. B **13**, 1168 (1976).

59. E. Fawcett, Rev. Mod. Phys. **80**, 209 (1988).

60. M.E. Fisher, J. Appl. Phys. **52**, 2014 (1981).

61. J.W. Cable, E.O. Wollan, W.C. Koehler, and M.K. Wilkinson, Phys. Rev. **140**, A1896 (1965).

62. M. Habenschuss, C. Stassis, S.K. Sinha, H.W. Deckman, and F.H. Spedding, Phys. Rev. B **10**, 1020 (1974).

63. J.J. Rhyne and S.J. Pickart, A.I.P. Conf. Proc. No. 5, edited by D.C. Graham and J.J. Rhyne, 1436 (AIP, New York, 1972).

64. M. Atoji, Solid State Communications **14**, 1047 (1974).

65. J. Jensen, J. Phys. F. **6**, 1145 (1976).

66. R.W. Green, S. Legvold, and F.H. Spedding, Phys. Rev. **122**, 827 (1961).

67. R.E. Skochdopole, M. Griffel, and F.H. Spedding, J. Chem. Phys. **23**, 2258 (1955).

68. J.R. Banister, S. Legvold, and F.H. Spedding, Phys. Rev. **94**, 1140 (1954).

69. R.B. Flippen, J. Appl. Phys. **35**, 1047 (1964).

70. J.J. Rhyne, S. Foner, E.J. McNiff, Jr., and R. Doclo,

J. Appl. Phys. **39**, 892 (1968).

71. J.L. Feron, G. Hug, and R. Pauthenet, Z. Angew. Phys. **30**, 61 (1971).

72. S. Gama and M.E. Foglio, Phys. Rev. B **37**,2123 (1988).

73. N. Ali and F. Willis, Phys. Rev. B **42**, 6820 (1990).

74. H.V. Anström, D.X. Chen, G. Benediktsson, and K.V. Rao, J. Phys. Condens. Matter **2**, 3349 (1990).

75. C. Stassis, G.R. Kline, A.J. Freeman, and J.P.Desclaux, Phys. Rev. B **13**, 3916 (1976).

76. V.F. Sears, *Methods of Experimental Physics 23 (A), Neutron Scattering*, edited by K. Sköld and D. L. Price (Academic Press, Inc., Orlando, Florida, 1986), p 521.

77. H.U. Aström and G. Benediktsson, J. Phys.: Condens. Matter **1**, 4381 (1989).

78. R.M. Nicklow, N. Wakadbyashi, M.K. Wilkinson, and R.E. Reed, Phys. Rev. Lett. **27**, 334 (1971).